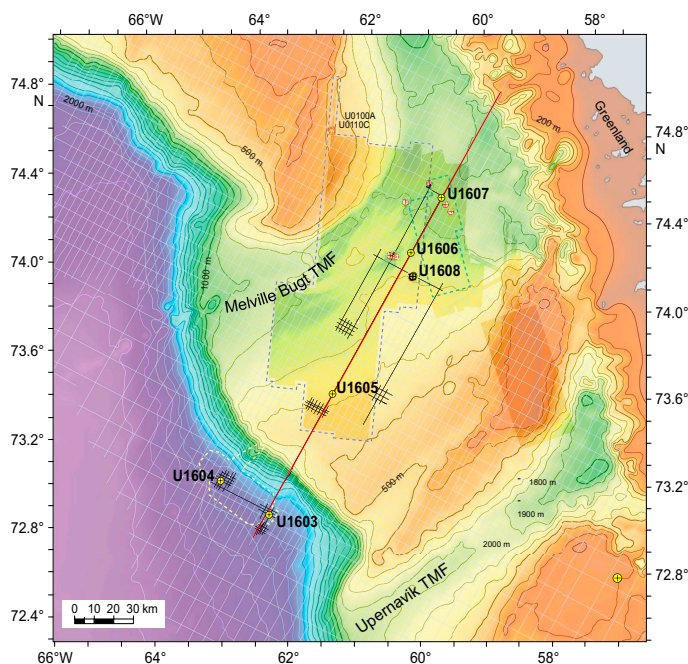# Site U1603[1]

P.C. Knutz, A.E. Jennings, L.B. Childress, R. Bryant, S.K. Cargill, H.K. Coxall, T.D. Frank, G.R. Grant, R.E. Gray, L. Ives, V. Kumar, S. Le Houedec, J. Martens, F. Naim, M. Nelissen, V. Özen, S. Passchier, L.F. Pérez, J. Ren, B.W. Romans, O. Seki, P. Staudigel, L. Tauxe, E.J. Tibbett, Y. Yokoyama, Y. Zhang, and H. Zimmermann[2]

Contents

Keywords

International Ocean Discovery Program, IODP, *JOIDES Resolution*, Expedition 400, NW Greenland Glaciated Margin, Site U1603, Baffin Bay, trough mouth fan, ice sheet instability, interglacial, glacial–interglacial cycles, laminated facies, detrital carbonate, ice-rafted debris, IRD, continental slope channel-levee deposit, contourites

Core descriptions

Supplementary material

References (RIS)

1. Background and objectives

Site U1603 (proposed Site MB-23A) is located at 72°59.04′N, 62°58.83′W in Baffin Bay at 1801 meters below sea level (mbsl), below a protrusion of the northwest Greenland margin shaped by the Melville Bugt Trough Mouth Fan (TMF) (Figure **F1**). The site targets an expanded drift-channel succession situated on the lower slope between two paleo–ice sheet outlets that represent major drainage routes for the northern Greenland ice sheet (NGrIS) into Baffin Bay (Knutz et al., 2019; Newton et al., 2017, 2021). The drilling strategy was to core a continuous high-resolution record of ice-ocean processes spanning the early late Pleistocene.

Figure F1. Bathymetry map showing position of Site U1603 in relation to other Expedition 400 sites, as well as Expedition 344S Sites U0100–U0110. Gray line grid = regional 2D seismic data (TGS). Black line grids = high-resolution multichannel seismic data (LAKO19). Yellow dotted line = seafloor area mapped by multibeam echosounder around deepwater sites. Dotted outlines = areas covered by 3D seismic on the shelf, dark blue and light blue for ANU (2013) and PITU (2011) surveys, respectively (Newton et al., 2017; Cox et al., 2021). Bathymetry shown outside areas mapped by spatial geophysical data is based on International Bathymetric Chart of the Arctic Ocean (IBCAO) v. 3.0 (Jakobsson et al., 2012).

Selection of Site U1603 was guided by regional 2D and high-resolution seismic data from where 10 horizons were mapped (including the seabed), defining 11 seismic units of the prograded TMF system (Knutz et al., 2019) (Figure **F2**). The strategy was to obtain a continuous high-resolution record spanning the early late Pleistocene by coring through Seismic Horizons 8–11 into a stratified interval within Seismic Unit 8, which appears to predate the channel formation. Site U1603 is paired seismic-stratigraphically with Site U1604, located 16 nmi (~30 km) to the northwest.

The drift-channel succession cored at Site U1603 is influenced by the circulation of deepwater masses in Baffin Bay, which is poorly constrained by oceanographic data but may be influenced by a southward flow along the Greenland margin that counters the surface currents (Tang et al., 2004). Gyre pulses of the West Greenland Current may overflow the site at intermediate water depths (e.g., to 800 mbsl) (Münchow et al., 2015). The sediment sequence thickens nearer to the channel margins, most prominently on the northern flanks of the channels (Knutz et al., submitted). The succession is hypothesized to represent interactions between bottom contour currents and sediments supplied by the NGrIS through glacial–interglacial cycles. Increased glacigenic sediment fluxes may be expected during periods when ice was grounded on the outer shelf and during phases of ice sheet retreat. The first two scientific objectives for Sites U1603 and U1604 are (1) to test the hypothesis that the NGrIS underwent significant deglaciation at intervals within the frequency range of orbital eccentricity (~100–400 ky) (Schaefer et al., 2016; Knutz et al., 2019) potentially related to exceptionally warm or prolonged super-interglacials (Christ et al., 2023) and (2) to achieve a long-term understanding (e.g., the last 0.5 My or older) of marine-based ice sheet dynamics and phasing relations between ice streams draining different sectors of the North American and Greenland ice sheets. In particular, we hope that the records can provide insights to ocean conditions through glacial terminations and ice-ocean dynamics associated with the different stages of ice sheet configurations (Hiscott et al., 1989; Simon et al., 2014), which may have far-field effects such as those associated with the opening/closing of the Canadian Arctic straits (Jennings et al., 2022; Kelleher et al., 2022; Lofverstrom et al., 2022) (Figure **F3**). Finally, the multiproxy data collected at deepwater Sites U1603 and U1604 will contribute to the third scientific objective of testing the regolith hypothesis for the change in orbital insolation frequency across the mid-Pleistocene transition (Clark and Pollard, 1998).

Triple-hole coring was planned for Site U1603 using the advanced piston corer/half-length advanced piston corer (APC/HLAPC) systems, with a target depth of 250 m core depth below seafloor, Method A (CSF-A), in the first two holes and 422 m CSF-A in the third hole. Downhole logging with the triple combo, Versatile Seismic Imager (VSI), and Formation MicroScanner (FMS)-sonic tool strings was planned for the deepest hole.
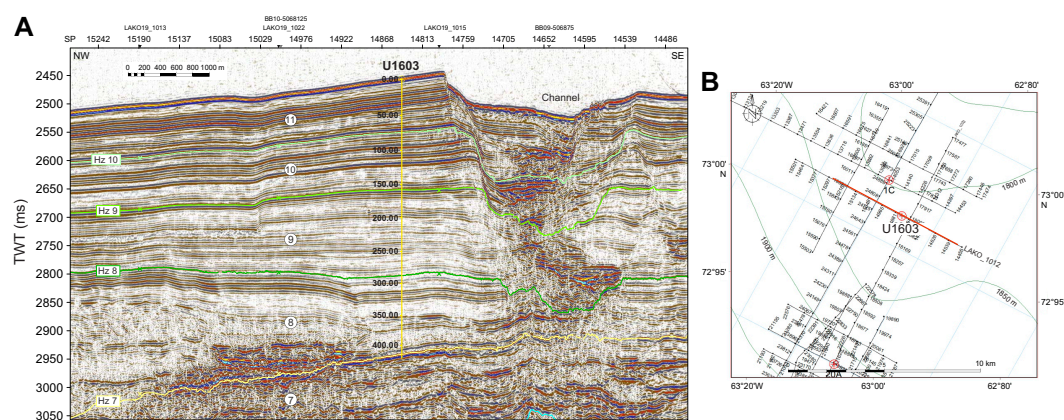
Figure F2. A. Seismic profile (LAKO_1012) showing location of Site U1603 on the lower slope of the Melville Bugt TMF adjacent to a channel. Interpreted Horizons 7–10 and the associated units (Seismic Unit 11 being topmost) are indicated. TWT = two-way traveltime. Site U1603 depths are in meters based on the preferred time-depth model (see Downhole logging). B. Close-up bathymetry map with seismic survey lines in the vicinity of Site U1603. Gray line grid = regional 2D seismic data (TGS). Black line grid = high-resolution multichannel seismic data (LAKO19).

2. Operations

2.1. Port call

Expedition 400 began in Reykjavík, Iceland, at Skarfabakki Harbour at 0815 h on 12 August 2023. The Expedition 395 science party departed the R/V *JOIDES Resolution* on 12 August, and on 13 August the crew, staff, and science party of Expedition 400 boarded the vessel, with the oncoming *JOIDES Resolution* Science Operator technical staff arriving at 0900 h and the science party at 1445 h. Immigration checks for those sailing were conducted dockside during the afternoon and completed by 1600 h. The science party began expedition preparation and received orientations including life at sea and safety training along with introductions to the laboratories during the rest of the port call. The two ice navigators were set up with internet access, and the ice analysis and reporting routine was initiated.

Freight was completed throughout the port call and included off-going shipments of core and refrigerated and frozen samples as well as the loading of sepiolite (drilling mud), drilling equipment, and fresh and frozen foods. On 16 August, fuel was bunkered and a boat drill was conducted.

The vessel was readied for departure, and the pilot came on board at 0745 h on 17 August. The tugboats were secured shortly after, and the last line was released at 0806 h, marking the official start of the initial transit. By 0822 h, the tugboats were released; the pilot departed, and our sea passage to Site U1603 began at 0824 h.

2.2. Site U1603

Hole location, water depth, and the number of cores recovered are listed in Table **T1**. All times are local ship time (UTC – 3 h) unless otherwise noted.

Site U1603 was the first site occupied during Expedition 400. *JOIDES Resolution* completed the 1721 nmi transit from Iceland to Site U1603 in 153.2 h (6.4 days) at an average speed of 11.3 kt (including pilotage). A favorable current and wind contributed greatly to this average speed as we transited up the west side of Greenland. The vessel arrived on site at 1355 h on 23 August 2023,

Parameter	Proxy	Full ice	Termination	Interglacial	Super-interglacial	Pre-GrIS
Sites		U1603, U1604, U1605, U1608	U1603, U1604, U1605, U1608	U1603, U1604, U1605, U1608	U1603, U1604, U1605, U1608	U1606, U1607, U1608
Ice sheet configuration indicators						
Iceberg production	IRD	0 to ++	++++	0 to +	0	0
Land exposure	^{10}Be	0	0	+	++	+++
Ice cover	^{10}Be/^{26}Al	<7 (burial)	<7 (burial)	7	7	7
Terrigenous flux	Volumetric sed. rate, sedimentary magnetism, NGR	+ to ++	+++++	+	+	+ to ++
Terrestrial productivity	Pollen, leaf waxes, DNA, fossils	0	+	++	+++	++++
Sediment sourcing	Elemental, magnetic, mineral, and isotopic provenance	Glacial flowline, warm - polythermal bed	Glacial flowline, warm bed	Multiple ice-rafted sources, reworked glacial	Fluvial, reworked glacial, more local	Fluvial, basin only
Weathering intensity	Mineralogy, grain size and texture	0	0	+	++	++++
Glacial meltwater	Salinity reconstructions using δ^{18}O and trace elements in foraminifera, palmitic acid δD	0 to +	++++	++	0	0 to +
Environmental indicators						
Depositional processes (Shelf environment)	Lithofacies description	Tills	Glacial-marine, diamicton	Hemipelagic	Hemipelagic	Hemipelagic, contourite, deltaic
Depositional processes (Basin environment)	Lithofacies description	Glacial-marine, plumites/turbidites	Glacial-marine, plumites/turbidites	Hemipelagic, glacial-marine, contourite	Hemipelagic, contourite	Hemipelagic, contourite
Terrestrial climate	Pollen, brGDGT, leaf wax	Cold, dry	Transitional	Warm, wet	Warmer, wetter	Warmest, wettest
Ocean water conditions (surface/subsurface)	Dinoflagellate, diatom and foraminifera; isoGDGTs (e.g. TEX$_{86}$) shell trace elements δD	Cold	Cool, strongly stratified	Warm, highly seasonal	Very warm	Very warm
Sea Ice	IRD, Dinoflagellates and diatoms; biomarkers (HBIs, e.g. IP$_{25}$)	+++	++ to +++	+	0-?	0-?

Figure F3. Diagnostic template for interpreting different stages of ice sheet evolution on the northwest Greenland margin, Expedition 400. GrIS = Greenland ice sheet, brGDGT = branched glycerol dialkyl glycerol tetraether, isoGDGT = isoprenoid GDGT, HBI = highly branched isoprenoid.

Table T1. Core summary, Site U1603. DRF = drilling depth below rig floor, DSF = drilling depth below seafloor. APC_Calc = drill string length from rig floor to the bit, plus the length of the extended APC core barrel, minus the length of core recovered. Offset = seafloor depth is adopted from the previous hole. Tagged = driller detected weight or torque on bit. H = APC, F = HLAPC, R = RCB, numeric core type = drilled interval. NA = not applicable. (Continued on next two pages.) **Download table in CSV format.**

Hole U1603A
Latitude: 72°59.0386′N
Longitude: 62°58.8333′W
Water depth (m): 1800.76
Date started (UTC): 1715 h; 23 August 2023
Date finished (UTC): 2045 h; 24 August 2023
Time on hole (days): 1.15
Seafloor depth DRF (m): 1811.9
Seafloor depth est. method: APC_Calc
Rig floor to sea level (m): 11.14
Penetration DSF (m): 118.6
Cored interval (m): 118.6
Recovered length (m): 119
Recovery (%): 100.34
Drilled interval (m): NA
Drilled interval (no.): 0
Total cores (no.): 13
APC cores (no.): 13
HLAPC cores (no.): 0
XCB cores (no.): 0
RCB cores (no.): 0
Other cores (no.): 0

Hole U1603B
Latitude: 72°59.0441′N
Longitude: 62°58.8431′W
Water depth (m): 1800.76
Date started (UTC): 2045 h; 24 August 2023
Date finished (UTC): 1500 h; 26 August 2023
Time on hole (days): 1.76
Seafloor depth DRF (m): 1811.9
Seafloor depth est. method: Tagged
Rig floor to sea level (m): 11.14
Penetration DSF (m): 243.98
Cored interval (m): 134.88
Recovered length (m): 122.68
Recovery (%): 90.95
Drilled interval (m): 109.1
Drilled interval (no.): 1
Total cores (no.): 26
APC cores (no.): 4
HLAPC cores (no.): 22
XCB cores (no.): 0
RCB cores (no.): 0
Other cores (no.): 0

Hole U1603C
Latitude: 72°59.0480′N
Longitude: 62°58.8542′W
Water depth (m): 1800.76
Date started (UTC): 1500 h; 26 August 2023
Date finished (UTC): 0315 h; 28 August 2023
Time on hole (days): 1.51
Seafloor depth DRF (m): 1811.9
Seafloor depth est. method: Offset
Rig floor to sea level (m): 11.14
Penetration DSF (m): 285
Cored interval (m): 73.5
Recovered length (m): 22.78
Recovery (%): 30.99
Drilled interval (m): 211.5
Drilled interval (no.): 1
Total cores (no.): 8
APC cores (no.): 0
HLAPC cores (no.): 0
XCB cores (no.): 0
RCB cores (no.): 8
Other cores (no.): 0

Hole U1603D
Latitude: 72°59.0506′N
Longitude: 62°58.8735′W
Water depth (m): 1800.37
Date started (UTC): 0315 h; 28 August 2023
Date finished (UTC): 1200 h; 01 September 2023
Time on hole (days): 4.36
Seafloor depth DRF (m): 1811.9
Seafloor depth est. method: Offset
Rig floor to sea level (m): 11.14
Penetration DSF (m): 422
Cored interval (m): 152.6
Recovered length (m): 43.31
Recovery (%): 28.38
Drilled interval (m): 269.4
Drilled interval (no.): 1
Total cores (no.): 17
APC cores (no.): 0
HLAPC cores (no.): 0
XCB cores (no.): 0
RCB cores (no.): 17
Other cores (no.): 0

Hole U1603E
Latitude: 72°59.0551′N
Longitude: 62°58.8829′W
Water depth (m): 1800.37
Date started (UTC): 1200 h; 01 September 2023
Date finished (UTC): 0445 h; 02 September 2023
Time on hole (days): 0.7
Seafloor depth DRF (m): 1811.6
Seafloor depth est. method: APC_Calc
Rig floor to sea level (m): 11.23
Penetration DSF (m): 59.1
Cored interval (m): 59.1
Recovered length (m): 17.48
Recovery (%): 29.58
Drilled interval (m): NA
Drilled interval (no.): 0
Total cores (no.): 7
APC cores (no.): 6
HLAPC cores (no.): 1
XCB cores (no.): 0
RCB cores (no.): 0
Other cores (no.): 0

Hole U1603F
Latitude: 72°59.0361′N
Longitude: 62°58.8180′W
Water depth (m): 1801.25
Date started (UTC): 0445 h; 02 September 2023
Date finished (UTC): 0445 h; 03 September 2023
Time on hole (days): 1
Seafloor depth DRF (m): 1812.5
Seafloor depth est. method: APC_Calc
Rig floor to sea level (m): 11.25
Penetration DSF (m): 134.3
Cored interval (m): 134.3
Recovered length (m): 116.93
Recovery (%): 87.07
Drilled interval (m): NA
Drilled interval (no.): 0
Total cores (no.): 15
APC cores (no.): 14
HLAPC cores (no.): 1
XCB cores (no.): 0
RCB cores (no.): 0
Other cores (no.): 0

Core	Top depth DSF (m)	Bottom depth DSF (m)	Interval advanced (m)	Recovered length (m)	Curated length (m)	Core recovery (%)	Core on deck date (2023)	Core on deck time UTC (h)	Sections (*N*)
400-U1603A-									
1H	0.0	4.6	4.6	4.65	4.65	101	24 Aug	0735	5
2H	4.6	14.1	9.5	9.05	9.05	95	24 Aug	0835	7
3H	14.1	23.6	9.5	9.83	9.83	103	24 Aug	0920	8
4H	23.6	33.1	9.5	9.82	9.82	103	24 Aug	1020	8
5H	33.1	42.6	9.5	9.89	9.89	104	24 Aug	1055	8
6H	42.6	52.1	9.5	9.82	9.82	103	24 Aug	1135	8
7H	52.1	61.6	9.5	8.87	8.87	93	24 Aug	1235	7
8H	61.6	71.1	9.5	10.07	10.07	106	24 Aug	1310	8
9H	71.1	80.6	9.5	9.87	9.87	104	24 Aug	1350	8
10H	80.6	90.1	9.5	10.27	10.27	108	24 Aug	1450	8
11H	90.1	99.6	9.5	9.99	9.99	105	24 Aug	1550	8
12H	99.6	109.1	9.5	7.39	7.39	78	24 Aug	1640	6
13H	109.1	118.6	9.5	9.48	9.48	100	24 Aug	1740	8
Hole U1603A totals:		118.6	119.00	119.00					97
400-U1603B-									
11	0.0	109.1	109.1	*****Drilled interval*****			25 Aug	0345	0
2H	109.1	118.6	9.5	9.86	9.86	104	25 Aug	0520	8
3H	118.6	128.1	9.5	2.04	2.04	21	25 Aug	0615	3
4H	128.1	137.6	9.5	9.72	9.72	102	25 Aug	0720	8
5H	137.6	147.1	9.5	9.68	9.68	102	25 Aug	0920	8

Table T1 (continued). (Continued on next page.)

Core	Top depth DSF (m)	Bottom depth DSF (m)	Interval advanced (m)	Recovered length (m)	Curated length (m)	Core recovery (%)	Core on deck date (2023)	Core on deck time UTC (h)	Sections (*N*)
6F	147.1	151.9	4.8	4.93	4.93	103	25 Aug	1020	5
7F	151.9	156.6	4.7	5.02	5.02	107	25 Aug	1105	5
8F	156.6	158.4	1.8	1.75	1.75	97	25 Aug	1145	3
9F	158.4	163.2	4.8	0.62	0.62	13	25 Aug	1255	2
10F	163.2	167.9	4.7	3.66	3.66	78	25 Aug	1400	4
11F	167.9	172.6	4.7	4.77	4.77	101	25 Aug	1450	5
12F	172.6	177.4	4.8	3.76	3.76	78	25 Aug	1535	4
13F	177.4	182.1	4.7	3.83	3.83	81	25 Aug	1620	4
14F	182.1	186.9	4.8	3.42	3.42	71	25 Aug	1650	3
15F	186.9	191.6	4.7	4.79	4.79	102	25 Aug	1800	5
16F	191.6	196.4	4.8	4.01	4.01	84	25 Aug	1840	4
17F	196.4	201.1	4.7	5.04	5.04	107	25 Aug	1925	5
18F	201.1	205.9	4.8	5.11	5.11	106	25 Aug	2000	5
19F	205.9	210.6	4.7	4.83	4.83	103	25 Aug	2100	5
20F	210.6	215.4	4.8	5.02	5.02	105	25 Aug	2145	5
21F	215.4	220.1	4.7	5.10	5.10	109	25 Aug	2230	5
22F	220.1	224.9	4.8	4.97	4.97	104	25 Aug	2310	5
23F	224.9	229.6	4.7	5.01	5.01	107	26 Aug	0105	5
24F	229.6	234.4	4.8	5.06	5.06	105	26 Aug	0200	5
25F	234.4	239.1	4.7	5.27	5.27	112	26 Aug	0305	5
26F	239.1	243.9	4.8	5.33	5.33	111	26 Aug	0455	5
27F	243.9	244.0	0.1	0.08	0.08	100	26 Aug	1640	1
Hole U1603B totals:			244.0	122.70	122.70				122
400-U1603C-									
11	0.0	211.5	211.5	*****Drilled interval*****			27 Aug	1230	0
2R	211.5	217.1	5.6	3.37	3.37	60	27 Aug	1325	4
3R	217.1	226.8	9.7	4.21	4.21	43	27 Aug	1420	4
4R	226.8	236.5	9.7	0.07	0.07	1	27 Aug	1545	1
5R	236.5	246.2	9.7	3.66	3.66	38	27 Aug	1700	4
6R	246.2	255.9	9.7	0.10	0.10	1	27 Aug	1840	1
7R	255.9	265.6	9.7	4.19	4.19	43	27 Aug	1950	4
8R	265.6	275.3	9.7	3.77	3.77	39	27 Aug	2105	4
9R	275.3	285.0	9.7	3.41	3.41	35	27 Aug	2250	4
Hole U1603C totals:			285.0	22.80	22.80				26
400-U1603D-									
11	0.0	269.4	269.4	*****Drilled interval*****			29 Aug	0855	0
2R	269.4	275.0	5.6	2.49	2.49	44	29 Aug	1010	3
3R	275.0	284.7	9.7	0.72	0.72	7	29 Aug	1120	2
4R	284.7	294.4	9.7	0.06	0.06	1	29 Aug	1250	1
5R	294.4	304.1	9.7	1.17	1.17	12	29 Aug	1345	2
6R	304.1	313.8	9.7	0.97	0.97	10	29 Aug	1440	2
7R	313.8	323.5	9.7	3.84	3.84	40	29 Aug	1605	4
8R	323.5	333.2	9.7	5.37	5.37	55	29 Aug	1700	6
9R	333.2	342.9	9.7	0.10	0.10	1	30 Aug	1240	1
10R	342.9	352.6	9.7	2.11	2.11	22	30 Aug	1330	3
11R	352.6	362.3	9.7	3.95	3.95	41	30 Aug	1420	4
12R	362.3	372.0	9.7	3.38	3.38	35	30 Aug	1545	4
13R	372.0	381.7	9.7	5.86	5.86	60	30 Aug	1705	5
14R	381.7	391.4	9.7	2.13	2.13	22	30 Aug	1800	3
15R	391.4	401.1	9.7	2.66	2.66	27	30 Aug	2000	3
16R	401.1	410.8	9.7	3.84	3.84	40	30 Aug	2150	4
17R	410.8	420.5	9.7	4.16	4.16	43	30 Aug	2340	4
18R	420.5	422.0	1.5	0.50	0.50	33	31 Aug	0130	2
Hole U1603D totals:			422.0	43.30	43.30				53
400-U1603E-									
1H	0.0	6.9	6.9	6.94	6.94	101	1 Sep	2100	6
2H	6.9	16.4	9.5	9.75	9.75	103	1 Sep	2200	8
3H	16.4	25.9	9.5	0.17	0.17	2	1 Sep	2245	1
4H	25.9	35.4	9.5	0.14	0.14	1	1 Sep	2350	1
5H	35.4	44.9	9.5	0.17	0.17	2	2 Sep	0030	1
6H	44.9	54.4	9.5	0.00	NA	0	2 Sep	0130	0
7F	54.4	59.1	4.7	0.31	0.31	7	2 Sep	0335	2
Hole U1603E totals:			59.1	17.50	17.50				19
400-U1603F-									
1H	0.0	6.0	6.0	6.08	6.08	101	2 Sep	0555	5
2H	6.0	15.5	9.5	9.77	9.77	103	2 Sep	0650	8
3H	15.5	25.0	9.5	9.75	9.75	103	2 Sep	0735	8
4H	25.0	34.5	9.5	10.17	10.17	107	2 Sep	0840	8

Table T1 (continued).

Core	Top depth DSF (m)	Bottom depth DSF (m)	Interval advanced (m)	Recovered length (m)	Curated length (m)	Core recovery (%)	Core on deck date (2023)	Core on deck time UTC (h)	Sections (*N*)
5H	34.5	44.0	9.5	9.72	9.72	102	2 Sep	0935	8
6F	44.0	48.8	4.8	4.73	4.73	99	2 Sep	1100	5
7H	48.8	58.3	9.5	9.91	9.91	104	2 Sep	1215	8
8H	58.3	67.8	9.5	10.16	10.16	107	2 Sep	1315	8
9H	67.8	77.3	9.5	7.44	7.44	78	2 Sep	1405	6
10H	77.3	86.8	9.5	8.42	8.42	89	2 Sep	1600	7
11H	86.8	96.3	9.5	0.27	0.27	3	2 Sep	1650	1
12H	96.3	105.8	9.5	1.16	1.16	12	2 Sep	1735	2
13H	105.8	115.3	9.5	9.87	9.87	104	2 Sep	1840	8
14H	115.3	124.8	9.5	9.66	9.66	102	2 Sep	1940	8
15H	124.8	134.3	9.5	9.82	9.82	103	2 Sep	2035	8
Hole U1603F totals:			134.3	116.90	116.90				98
Site U1603 totals:			1263.0	442.20	442.20				415

and the thrusters were lowered and the dynamic positioning (DP) system was engaged. At 1420 h, operations began for Site U1603.

2.2.1. Hole U1603A

The first attempt to spud Hole U1603A was an APC shot from 1802.0 meters below rig floor (mbrf), which resulted in a water core. The pipe was lowered 5 m and shot from 1807 mbrf. Hole U1603A was spudded at 0425 h on 24 August 2023 with 4.65 m recovered. The seafloor was calculated at 1800.8 mbsl (1811.9 mbrf; meters below rig floor is 11.1 m greater than meters below sea level).

APC coring continued through Core 400-U1603A-13H at 118.6 m CSF-A. The advanced piston corer temperature (APCT-3) tool was run on Cores 4H, 7H, 10H, and 13H. The core liner shattered on Core 13H and had to be pumped out of the liner.

At 1515 h on 24 August, the bridge notified the drill floor that an iceberg had entered the Red Zone (i.e., would be within 3 nmi of the vessel in less than twice the time it will take to trip up to 50 m CSF-A). The drill string was tripped up with the top drive from 109.1 to 43.21 m CSF-A at 1600 h. From 1600 to 1715 h, the vessel tracked two icebergs. At 1715 h, with one of the icebergs entering the Termination Zone (within 1 nmi of the vessel), the order was given to pull the pipe clear of the seafloor. The drill string was again pulled up with the top drive, this time to 1778.3 mbrf, clearing the seafloor at 1742 h and ending Hole U1603A. The vessel was moved 500 m south in DP mode. The closest iceberg passed within ~0.6 nmi of the vessel. Once it was safe to do so, the vessel was moved back over location and offset 10 m northwest of Hole U1603A, coming into position at 2000 h on 24 August.

A total of 13 cores were taken in Hole U1603A over a 118.6 m interval with 100.3% recovery. Temperature measurements using the APCT-3 tool were taken on Cores 4H, 7H, 10H, and 13H. Total time on Hole U1603A was 27.6 h (1.15 days). In total, 1.25 h were spent waiting on ice, and an additional 1.25 h of operational time was spent pulling out of Hole U1603A to prepare to wait on ice.

2.2.2. Hole U1603B

Hole U1603B was spudded at 2035 h on 24 August 2023. It was washed down to 109.1 m CSF-A by 0100 h on 25 August. Coring began with Core 2H from 109.1 m CSF-A and continued through Core 5H at 147.1 m CSF-A. After an overpull and drillover of Core 5H, we switched to the half-length APC (HLAPC) system. HLAPC coring started with Core 6F and continued through Core 27F, shot from 243.9 m CSF-A at 0230 h on 26 August. The barrel pulled free from the formation with no overpull; however, the coring line could not pull the barrel up. The drill string was tripped back up to the vessel with the bit clearing the rig floor at 1157 h, ending Hole U1603B. Once the bottom hole assembly (BHA) was on board, the core barrel was recovered with 0.08 m of material,

likely from the push down trying to free the barrel. The final depth for Hole U1603B was 244.0 m CSF-A. The vessel was offset 10 m northwest of Hole U1603B.

A total of 26 cores were taken in Hole U1603B over a 134.9 m interval with 91.0% recovery. Total depth for Hole U1603B was 243.98 m CSF-A, and total time was 42.24 h (1.76 days). In total, 2.25 h were spent waiting on ice and an additional 5.75 h of operational time were spent starting a new hole and drilling down in Hole U1603B to the depth of penetration in Hole U1603A.

2.2.3. Hole U1603C

Hole U1603C was spudded at 0105 h on 27 August 2023, and the hole was drilled down over the next 7.75 h. Cores 2R–9R advanced from 211.5 to 285.0 m CSF-A and recovered 22.78 m (31%). At 1945 h, ice moved within 3 nmi of the vessel, and we raised the drill string to 22.3 m CSF-A and began waiting on ice.

At 0000 h on 28 August, ice entered the 1 nmi exclusion zone. We raised the drill string, clearing the seafloor at 0009 h and ending Hole U1603C, and continued waiting on ice. The vessel was moved 1200 m east-northeast and then 700 m east-southeast in DP mode to maintain a safe distance from the ice. By 0330 h, the ice had cleared the site and the vessel was positioned 10 m northwest of Hole U1603C.

A total of eight cores were taken in Hole U1603C over a 73.5 m interval with 31% recovery. Total depth for Hole U1603C was 285.0 m CSF-A, and total time was 36.24 h (1.51 days). In total, 2.25 h were spent waiting on ice and an additional 2.0 h of operational time were spent pulling out of Hole U1603C to wait on ice.

2.2.4. Hole U1603D

Hole U1603D was spudded at 0455 h on 28 August 2023 and, with a wash barrel, was drilled ahead to 102.0 m CSF-A. As ice once again neared the site, we decided to install a free fall funnel (FFF) to allow us to reenter Hole U1603D. The FFF was deployed at 0950 h, and by 1030 h we resumed drilling ahead in Hole U1603D to 189.0 m CSF-A. At 1400 h, ice moved within 3 nmi of the vessel, and we raised the drill string to 22.3 m CSF-A by 1515 h and began waiting on ice for the remainder of the day.

By 0015 h on 29 August, the ice had cleared the site. The drill string was lowered to 169.6 m CSF-A, and we washed back to 189.0 m CSF-A before drilling ahead to 269.4 m CSF-A. Cores 400-U1603D-2R through 8R advanced from 269.4 to 333.2 m CSF-A and recovered 14.62 m (24%). At 1400 h, ice moved within 3 nmi of the vessel, and we raised the drill string to 22.3 m CSF-A by 1545 h and began waiting on ice. Ice then entered the 1 nmi exclusion zone, and we raised the drill string, clearing the seafloor at 1930 h. The vessel was moved 1000 m north in DP mode to maintain a safe distance from the ice. By 2157 h, we began to move back toward the site, and the vessel was in position over Hole U1603D by 2348 h on 29 August.

At 0100 h on 30 August, we began preparing the subsea camera system to assist with reentering Hole U1603D. At 0320 h, we successfully reentered the hole and recovered the subsea camera system. The drill string was lowered to 294.4 m CSF-A, and we washed back to 318.5 m CSF-A before encountering material that had fallen into the bottom of the hole. A center bit was dropped, and we washed to 333.2 m CSF-A by 0800 h. Cores 9R–18R advanced from 333.2 to 422.0 m CSF-A and recovered 28.69 m (32%). Sepiolite (drilling mud) was swept in the hole, and the bit was released at 2315 h to prepare for logging Hole U1603D. We then tripped the drill string up to 50.8 m CSF-A in preparation for logging.

The modified triple combo (quad combo) tool string was rigged up and, following a repair to the logging winch, was deployed to the base of Hole U1603D (419.5 m CSF-A). The quad combo measures natural gamma ray, density, acoustic velocity, resistivity, magnetic susceptibility (MS), and density. Following a complete pass of the hole, the quad combo was pulled to the rig floor and broken down. The VSI was rigged up, and the protected species watch began at 1600 h on 31 August. The VSI was deployed but almost immediately experienced a communication issue. The tool was brought back on board and repaired. At 1800 h, the VSI was deployed to 413.1 m CSF-A, and stations were measured uphole until 2120 h, when fog impacted visibility and the ability to

monitor for protected species. After the VSI was brought back on board and broken down, the FMS-sonic tool string was assembled and deployed. The FMS-sonic tool string was run, and the tools were back on deck by 0345 h on 1 September. With logging completed, we tripped the pipe out of the hole, clearing the rig floor at 0900 h and ending Hole U1603D.

A total of 17 cores were taken in Hole U1603D over a 152.6 m interval with 28.4% recovery. Total depth for Hole U1603D was 422 m CSF-A, and total time was 104.64 h (4.36 days). In total, 21.5 h were spent waiting on ice, and an additional 24.75 h of operational time were spent drilling down in Hole U1603D to the depth of penetration in Hole U1603C and later pulling out of and reentering Hole U1603D.

2.2.5. Hole U1603E

An APC/extended core barrel (XCB) BHA was made up, and we began tripping the drill pipe back to the seafloor at 1200 h on 1 September 2023. The vessel was offset 10 m northwest in DP mode, and the pipe was pumped with a cleanout tool while the tracer pumps were running. Hole U1603E was spudded at 1745 h, and Core 1H recovered 6.94 m. Core 2H advanced to 16.4 m and recovered 9.75 m (103%). Cores 3H–6H each advanced 9.5 m but recovered almost no material (less than 20 cm each). The deplugger was run in the pipe. Core 7F advanced from 54.4 to 59.1 m CSF-A and recovered 0.31 m (7%). Following Core 7F, we decided to abandon Hole U1603E due to lack of recovery, and the drill string was tripped out, clearing the seafloor at 0140 h on 2 September.

A total of seven cores were taken in Hole U1603E over a 59.1 m interval with 29.6% recovery. Total time for Hole U1603E was 16.8 h (0.7 days).

2.2.6. Hole U1603F

The vessel was offset 10 m southeast of Hole U1603A to hopefully improve recovery and allow for better correlation with other holes. Hole U1603F was spudded at 0235 h on 2 September 2023. Cores 1H–5H advanced from 0 to 44.0 m CSF-A and recovered 45.49 m (103%). Core 6F (44.0– 48.80 m CSF-A; 4.73 m recovered) was cored with the HLAPC system to help adjust core spacing to cover gaps in Hole U1603A. Cores 7H–15H advanced from 48.8 to 134.3 m CSF-A and recovered 66.71 m (78%). The APCT-3 tool was run on Cores 4H and 10H. We then began pulling the drill string out of the hole, clearing the seafloor at 1935 h. The drill string was tripped up with the bit at the surface at 0030 h on 3 September. The drill floor was secured for transit, and the thrusters were raised and secured for transit at 0145 h, ending Hole U1603F and Site U1603.

A total of 15 cores were taken in Hole U1603F over a 134.3 m interval with 87.1% recovery. Total time for Hole U1603F was 24 h (1.0 days).

3. Lithostratigraphy

Site U1603 consists of six overlapping holes (U1603A–U1603F) cored to a total depth of 422 m CSF-A, with Holes U1603A–U1603D each recovering ~120 m thickness at successive depths and Holes U1603E and U1603F targeting the uppermost 130 m to replicate stratigraphy recovered in Hole U1603A. Of the 422 m thick section, 243.6 m of sediments were recovered. Based on those recovered sediments, the stratigraphy at this site is divided into four lithostratigraphic units (Figure **F4**; Table **T2**). Named lithofacies are sedimentary; are present in all four units with variable predominance; and include mud, calcareous mud, interlaminated to interbedded mud and sand, diamicton, and sandy mud with common clasts (Figure **F4**).

Sediments recovered are consistent with the site location at the base of the continental slope proximal to a glaciated progradational margin deposited during the Early to Late Pleistocene. The deposits in the uppermost ~243 m of the succession (Lithostratigraphic Units I and II) are consistent with downslope and along-slope sedimentation on a channel levee system with high sedimentation rates (~28 cm/ky on average) (see **Age model**). The uppermost ~42 m (Unit I) consists of mud with irregular sand laminae and dispersed clasts. A thick sequence of interlaminated to interbedded mud and sand is predominant between ~42 and 243 m CSF-A (Unit II) and is divided into two subunits distinguished by laminae/bed thickness, proportion of mud versus sand, and clast

occurrence. Subunit IIA consists of finer laminae, thinner sand beds, and a lower proportion of sand, whereas Subunit IIB (~145–243 m CSF-A) has thicker laminae and beds, a higher proportion of sand, and a relatively higher clast abundance. The deposits below 243 m CSF-A show a higher average sedimentation rate (~75 cm/ky) (see **Age model**). From 243 to 374 m CSF-A (Unit III), weakly stratified mud lithologies are dominant, sand lithofacies are rare, and clast occurrence increases significantly. In the lowermost ~46 m of Hole U1603D (Unit IV), weakly stratified muds similar in character to Unit III are present, but this unit also contains an interval of calcareous mud and various types of soft-sediment deformation that are absent in Unit III.

3.1. Unit descriptions

Site U1603 is divided into four lithostratigraphic units (I–IV; youngest to oldest), with Unit II divided into two subunits (IIA and IIB) (Figure **F4**). Significant downhole changes in lithology were determined using a combination of visual core description, microscopic characterization (using smear slides, grain mounts, and thin sections), reflectance spectroscopy and colorimetry, and bulk and clay mineralogical analyses using X-ray diffraction (XRD) (see **Lithostratigraphy** in the Expedition 400 methods chapter [Knutz et al., 2025]).

3.1.1. Unit I

Intervals: 400-U1603A-1H-1, 0 cm, to 5H-6, 112 cm; 400-U1603E-1H-1, 0 cm, to 5H-CC, 17 cm*; and 400-U1603F-1H-1, 0 cm, to 5H-5, 122 cm (asterisk denotes recovered extent in that hole [due to drill down or lack of recovery below]; see Table **T2**)
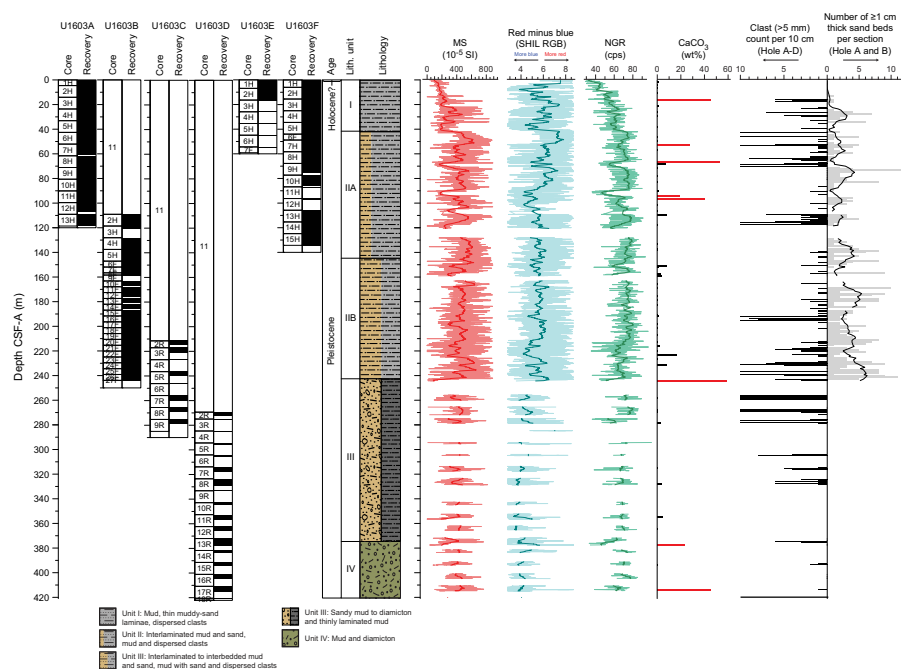Depth: 0–41.7 m CSF-A
Thickness: 41.7 m
Age: Pleistocene–Holocene?
Lithology: mud, thin muddy-sand laminae, dispersed clasts

Lithostratigraphic Unit I consists of grayish brown (uppermost two cores) and greenish to bluish gray mud (Core 400-U1603A-3H through Section 5H-6, 112 cm). Beds of thinly (millimeter scale)

Figure F4. Lithostratigraphic summary, Site U1603. MSP measurements are filtered to exclude those greater than two standard deviations from the mean. Thin red line = MSP measurements collected using the SHMSL, thick red line = depth-based rolling mean of the filtered data (10 m window). Red minus blue data and whole-round NGR measurements are plotted using the same method. cps = counts per second. Red bars = CaCO₃ in samples from intervals identified as calcareous mud (Lithofacies 2). Clast count data are plotted with bars centered on the 10 cm interval. Number of sand beds are plotted with bars centered on the core section. Black line = depth-based rolling mean (10 m window).

laminated mud alternate with massive mud layers on a ~1 m or thinner scale. Massive muds are sparsely and rarely moderately bioturbated. Clasts occur dispersed throughout the unit. Centimeter- to decimeter-scale interbeds of common to abundant clasts are also observed. Diagenetic color alteration (color banding) and iron-sulfide mineralization result in black mottling as both millimeter-scale patches and in discrete millimeter-scale laminae.

3.1.2. Unit II

3.1.2.1. Subunit IIA

Intervals: 400-U1603A-5H-6, 112 cm, to 13H-CC, 56 cm*; 400-U1603B-2H-1, 0 cm*, to 5H-5, 118 cm; 400-U1603E-5H-CC, 17 cm*, to 7H-CC, 12 cm*; and 400-U1603F-5H-5, 122 cm, to 15H-CC, 23 cm* (asterisk denotes recovered extent in that hole [due to drill down or lack of recovery below]; see Table T2)
Depth: 41.7–144.84 m CSF-A
Thickness: 103.14 m
Age: Pleistocene
Lithology: interlaminated mud and sand, mud with dispersed clasts

Lithostratigraphic Subunit IIA consists primarily of dark gray, millimeter-scale interlaminated mud and sand alternating with greenish gray to grayish brown mud, typically in continuous intervals on the order of 2–3 m. Sand beds 1–3 cm thick are overall rare but are common in specific intervals. Dispersed (<5%) to common (5%–10%) clasts occur in the mud lithofacies as coarse sand to fine gravel. Clasts containing pink feldspathic grains are common. Plutonic pebble-sized clasts are rare and not associated with a particular lithofacies. Clast abundance is generally higher in Subunit IIA than in Unit I. Bioturbation is rare in this subunit.

Table T2. Lithostratigraphic units, Site U1603. * = recovered extent of the unit in hole (due to drill down or lack of recovery below). — = hole does not overlap with the unit. Recovery percentages are based on core level recovery. Recovered meters are calculated from curated lengths. **Download table in CSV format.**

Lith. unit	Hole	Top hole, core, section, interval (cm)	Bottom hole, core, section, interval (cm)	Top depth CSF-A (m)	Bottom depth CSF-A (m)	Recovery (%)	Recovered (m)
		400-	400-				
I	U1603A	U1603A-1H-1, 0	U1603A-5H-6, 112	0.00	41.70	101	41.95
	U1603B	—	—	—	—	—	—
	U1603C	—	—	—	—	—	—
	U1603D	—	—	—	—	—	—
	U1603E	U1603E-1H-1, 0	U1603E-5H-CC, 17*	0.00	35.57*	42	17.17
	U1603F	U1603F-1H-1, 0	U1603F-5H-5, 122	0.00	41.70	103	42.97
IIA	U1603A	U1603A-5H-6, 112	U1603A-13H-CC, 56*	41.70	118.58*	100	77.05
	U1603B	U1603B-2H-1, 0*	U1603B-5H-5, 118	109.10*	144.84	82	28.86
	U1603C	—	—	—	—	—	—
	U1603D	—	—	—	—	—	—
	U1603E	U1603E-5H-CC, 17*	U1603E-7H-CC, 12*	35.57*	54.70*	3	0.31
	U1603F	U1603F-5H-5, 122	U1603F-15H-CC, 23*	41.70	134.62*	82	73.96
IIB	U1603A	—	—	—	—	—	—
	U1603B	U1603B-5H-5, 118	U1603B-26F-3, 55	144.84	242.59	95	91.9
	U1603C	U1603C-2R-1, 0*	U1603C-5R-CC, 28*	211.50*	240.16*	36	11.31
	U1603D	—	—	—	—	—	—
	U1603E	—	—	—	—	—	—
	U1603F	—	—	—	—	—	—
III	U1603A	—	—	—	—	—	—
	U1603B	U1603B-26F-3, 55	U1603B-27F-CC, 8*	242.59	243.98*	106	1.92
	U1603C	U1603C-6R-CC, 0*	U1603C-9R-CC, 14*	246.20*	278.71*	30	11.47
	U1603D	U1603D-2R-1, 0*	U1603D-13R-3, 0	269.40*	374.83	27	26.99
	U1603E	—	—	—	—	—	—
	U1603F	—	—	—	—	—	—
IV	U1603A	—	—	—	—	—	—
	U1603B	—	—	—	—	—	—
	U1603C	—	—	—	—	—	—
	U1603D	U1603D-13R-3, 0	U1603D-18R-CC, 8	374.83	421.00	38	16.32
	U1603E	—	—	—	—	—	—
	U1603F	—	—	—	—	—	—

3.1.2.2. Subunit IIB

Intervals: 400-U1603B-5H-5, 118 cm, to 26F-3, 55 cm, and 400-U1603C-2R-1, 0 cm*, to
  5R-CC, 28 cm* (asterisk denotes recovered extent in that hole [due to drill down or lack of
  recovery below]; see Table **T2**)
Depth: 144.84–242.59 m CSF-A
Thickness: 97.75 m
Age: Pleistocene
Lithology: interlaminated to interbedded mud and sand, mud with sand and dispersed clasts

Lithostratigraphic Subunit IIB consists of dark gray thinly to thickly interlaminated to thinly interbedded mud and sand. Mud and sand laminae are 1–10 mm thick, and normally graded sand beds as thick as 4 cm occur throughout this subunit. Grayish brown mud intervals are a minor component of this unit. These intervals frequently have dispersed clasts and typically contain very sparse and irregularly occurring sand laminae and thin beds. In Subunit IIB, sand beds (>1 cm) are both more numerous and generally thicker and dispersed clasts occur more frequently than in Subunit IIA. Sand composition in this unit becomes more quartz rich. Bioturbation is rare, with a thin interval of common–abundant bioturbation in Sections 400-U1603B-22F-1 and 22F-2.

3.1.3. Unit III

Intervals: 400-U1603B-26F-3, 55 cm, to 27F-CC, 8 cm*; 400-U1603C-6R-CC, 0 cm*, to 9R-CC,
  14 cm*; and 400-U1603D-2R-1, 0 cm*, to 13R-3, 0 cm* (asterisk denotes recovered extent
  in that hole [due to drill down or lack of recovery below]; see Table **T2**)
Depth: 242.59–374.83 m CSF-A
Thickness: 132.24 m
Age: Early Pleistocene
Lithology: sandy mud to diamicton and thinly laminated mud

Lithostratigraphic Unit III consists of dark grayish brown thinly laminated mud with rare to common sand laminae, weakly stratified sandy mud, mud with dispersed clasts, and clast-poor diamicton. The interlaminated mud and sand lithofacies is expressed with very thin parallel laminae (~1 mm). The sandy mud contains very faint parallel bedding structures, which are difficult to see in visible light but are more distinguishable in X-ray images. Dispersed clasts occur solely in mud lithologies and occur in intervals ~20 cm thick. Unit III is distinguished from Unit II by the higher proportion of diamicton and mud with common clasts. Bioturbation is absent or unobservable due to drilling disturbance.

3.1.4. Unit IV

Interval: 400-U1603D-13R-3, 0 cm, to 18R-CC, 8 cm
Depth: 374.83–421 m CSF-A
Thickness: 46.17 m
Age: Early Pleistocene
Lithology: mud and diamicton

Lithostratigraphic Unit IV consists of weakly stratified sandy mud and clast-poor muddy diamicton with intervals of thinly laminated mud. One bed of foraminifera-bearing calcareous clay was also observed. The mud intervals contain sedimentary structures including ripple cross lamination. Carbonate mud intraclasts (millimeter-scale diameter) occur as part of the clast fraction, which is otherwise dominated by plutonic and metamorphic lithologies. Bioturbation is rare, with the exception of one interval in Core 400-U1603D-13R. Synsedimentary microfaults, soft-sediment folds, and shear structures are common throughout most of this unit.

3.2. Lithofacies descriptions

At Site U1603, four main lithofacies are identified based on lithology, sedimentary structures, and textural and other common characteristics. This set of lithofacies is interpreted to represent a range of ice-distal to ice-proximal glaciomarine sedimentary processes in a continental slope to base-of-slope environment (water depth = 1800 m). Lithofacies are described below, emphasizing

visual description characteristics and supplemented with physical properties when relevant. Figure **F5** highlights multiple lithofacies and their associated characteristics.
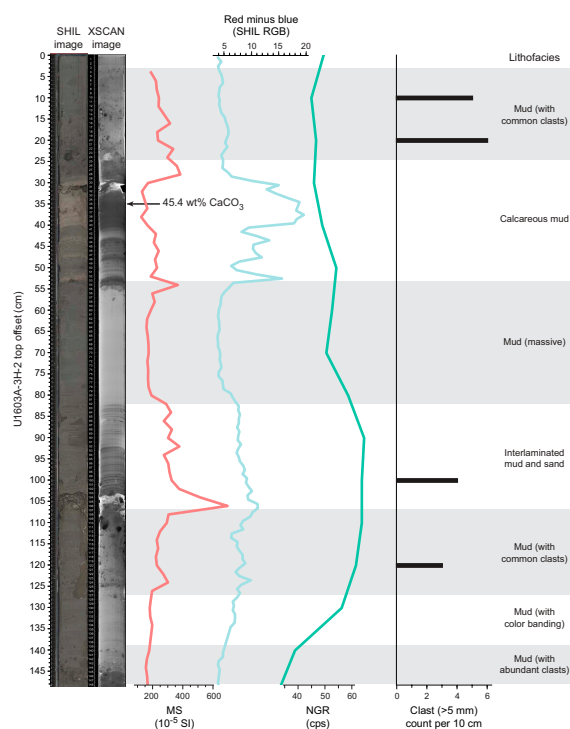
3.2.1. Lithofacies 1: mud

Lithofacies 1 consists of clay- and silt-sized terrigenous material and includes a large range in color spanning grayish yellow, grayish brown, and gray, including light to dark greenish gray and bluish gray. Sedimentary structures include massive/structureless, parallel laminations, and color banding (Figure **F6**). Individual mud laminae are <0.3–1 cm thick. Laminated mud intervals are typically <1 m thick and are often gradationally interstratified with mud that is massive and shows no clear evidence of lamination. Sand laminae (<1 cm) and very thin beds (1–3 cm) are present in some intervals, especially in gradational contact with Lithofacies 3 (interlaminated to interbedded mud and sand). Clasts are present in some intervals, ranging from sand-sized grains (0.063–2 mm) to sand blebs and pebble-sized clasts up to 6 cm in diameter. Where clasts occur, their abundance ranges from dispersed to common. Bioturbation is absent to sparse. There are very rare intervals with moderate bioturbation (e.g., interval 400-U1603A-13H-2, 0–80 cm). Mottling is present in rare intervals. Smear slides indicate that this mud lithofacies is composed of a mixture of clay and silt. The silt particles are commonly dominated by quartz and feldspar with common muscovite, amphibole, and rare accessory minerals.

Lithofacies 1 represents a continuum of slope depositional processes from suspension settling (hemipelagic) to bottom currents and low-concentration density flows. The sparse isolated clasts were likely delivered from ice rafting.

3.2.2. Lithofacies 2: calcareous mud

Lithofacies 2 consists of yellow-brown calcareous mud, which occurs in 1–30 cm thick beds. Smear slide analyses show that this lithofacies is dominated by mud-sized particles of abiotic carbonate, including rhombs, with minor siliciclastic components (Figure **F7A**). Bulk XRD analyses of selected intervals confirm that the carbonate mineralogy is dolomite and high-magnesium calcite. Carbonate contents, which range 19.4–58.4 wt% ($n = 8$), are significantly higher than those of enclosing sediments (average = 1.6 wt%; median = 0.4 wt%; $n = 54$) (see **Geochemistry**). Lithofacies 2 is also characterized by low MS values (approaching 0), an increase in L*, and an increase in


Figure F5. Multiple lithofacies, Section 400-U1603A-3H-2. cps = counts per second.
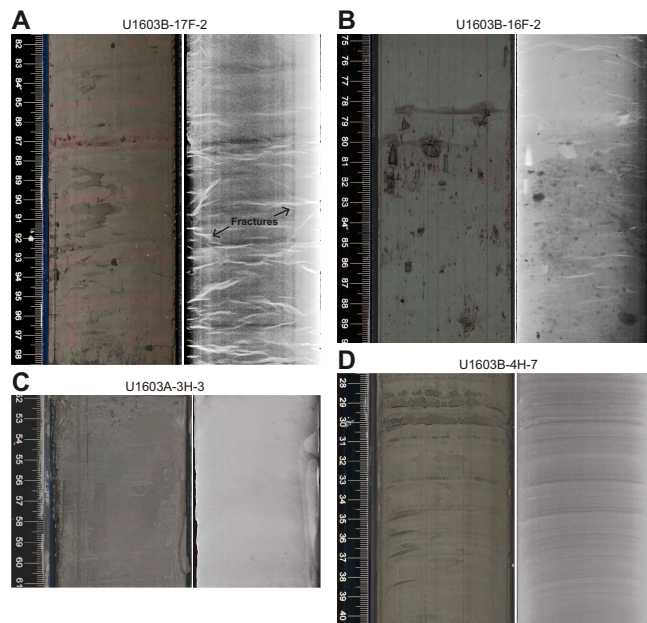
Figure F6. Lithofacies 1 (mud), Holes U1603A and U1603B. Paired SHIL and X-Ray Linescan Logger (XSCAN) images showing (A) mud with color banding (contrast was increased for red in the SHIL image; bright features in the X-ray image are fractures in the split core surface), (B) mud with clasts, (C) massive (structureless) mud, and (D) mud with parallel laminations.
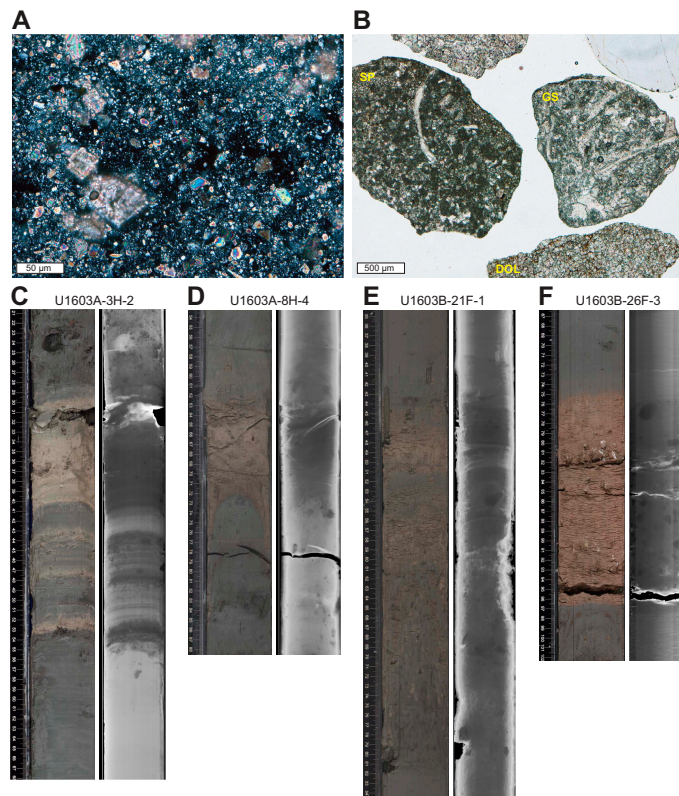

Figure F7. Lithofacies 2 (calcareous mud), Holes U1603A and U1603B. A. Calcareous mud facies (400-U1603B-21F-1, 49 cm). Clay- to silt-sized grains of carbonate, including distinct rhombs, dominate the composition. B. Carbonate clasts (26F-CC; plane-polarized light [PPL]). Silty packstone (SP) and grainstone (GS) clasts have been partially dolomitized, with altered remnants of fossil debris preserved. DOL = coarsely crystalline dolomite. C–F. Paired SHIL and XSCAN images showing (C) complex expression with gradational lower contact, (D) bed with gradational upper contact (lower contact distorted by drilling disturbance), (E) complex expression with gradational upper and lower contacts, and (F) bed with sharp lower and gradational upper contact.

the difference between red and blue color magnitudes relative to other lithofacies. The expression of Lithofacies 2 varies throughout the succession (Figure **F7C–F7F**). Some occurrences are isolated laminae or thin beds enclosed by gray siliciclastic-dominated deposits. Upper and lower contacts may be sharp or gradational. More complex occurrences are characterized by isolated blebs, laminae, or thin beds that grade upward into a thicker bed of calcareous mud before transitioning upward to isolated laminae within gray enclosing lithofacies. At Site U1603, there does not appear to be a systematic association between Lithofacies 2 and any other lithofacies.

Although Lithofacies 2 occurs throughout the succession, it is relatively rare in this otherwise siliciclastic-dominated succession and thus may indicate transient shifts in source regions for ice-related transport. The depositional processes involved in emplacing these layers (e.g., by ice rafting) does not appear to deviate strongly from adjacent, noncalcareous lithofacies (Lithofacies 1, 3, and 4). Localized occurrences of granule- to fine pebble–sized clasts of dolomitized fossiliferous limestone and dolostone (massive and nonfossiliferous) within the succession may provide some indication of provenance and glacial source regions for Lithofacies 2 (Figure **F7B**).

3.2.3. Lithofacies 3: interlaminated to interbedded mud and sand

Lithofacies 3 consists of interlaminated to interbedded mud and sand with variable proportions of mud versus sand throughout the succession. The mud component is dark gray to dark brown in color and commonly laminated (Figure **F8**). Bioturbation in the mud component varies but is typically sparse. The composition of the mud component based on smear slide analysis reveals varying mixtures of clay and silt, with the silt particles dominated by quartz and feldspar, with muscovite, amphibole, and other accessory minerals. The sand component of this lithofacies occurs within laminations (<1 cm) as well as very thinly bedded (1–3 cm) and rare thinly bedded (3–10 cm) layers. Sand grain size varies from very fine in the thinnest laminations to up to medium sand in the >2 cm thick beds. Normal grading is observed in >0.5 cm thick beds. Some of the sand beds displaying thicknesses ≥1 cm have internal structures including parallel lamination, ripple cross lamination, and centimeter-scale scour surfaces (Figure **F8**). Bioturbation in the sand component is variable but is typically absent to sparse. The sand composition based on smear slide analysis is dominated by angular quartz and feldspar grains, with lesser amounts of amphibole, mica (muscovite and biotite), and igneous rock fragments. Grains are typically angular and show little to no evidence of alteration. In general, this lithofacies does not contain abundant dispersed
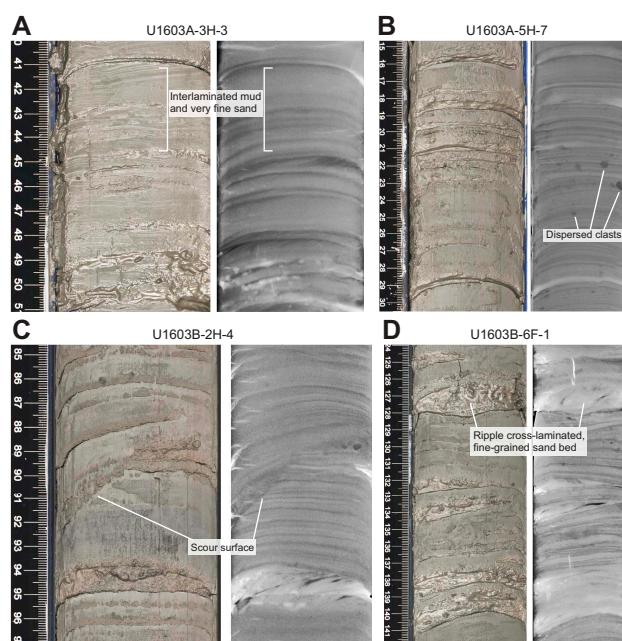
Figure F8. Lithofacies 3 (interlaminated to interbedded mud and sand), Holes U1603A and U1603B. SHIL and XSCAN pairs showing (A) interlaminated mud and sand (only visible in the XSCAN image), (B) rare dispersed clasts, (C) an erosional scour surface truncating underlying laminations, and (D) ~1 cm thick sand beds, which commonly exhibit ripple cross lamination.

clasts, but there are some intervals where isolated grains and granule to small-pebble clasts are observed (Figure F8).

Lithofacies 3 represents a complex mixture of depositional processes on the continental slope, including downslope (turbidity current) processes, contour-current deposition, and suspension settling from plumes. The thicker, coarser grained, and normally graded sand beds are likely derived from turbidity currents, whereas the specific depositional process of the mud component is similar to Lithofacies 1. The sparse isolated clasts were likely delivered by ice rafting.

3.2.4. Lithofacies 4: diamicton and sandy mud with common clasts

Lithofacies 4 consists of poorly sorted sediments with a matrix of sand and mud and a clast abundance of more than 1%, including diamicton and sandy mud with common clasts (Figure F9). These lithofacies rarely exceed more than 1 m in thickness, and both upper and lower bed boundaries are typically gradational. Collectively, the clasts comprise mainly polymict assemblages of igneous and metamorphic lithologies and occur both as isolated outsized clasts and as clast clusters. Clast sizes range from sand sized up to pebbles ~6 cm in diameter. Stratification of the diamict matrix on a decimeter scale is common and is evident from X-ray images. Locally, the matrix is organized into horizontal planar millimeter- to centimeter-scale poorly sorted laminae of sand and granules. The sandy mud is characterized by sand-rich (>25%) muds with thin (<3 mm) to thick (3–10 mm) parallel laminations that are generally less visually distinctive than the interlaminated lithofacies. A high degree of bioturbation may obscure the laminations or present a mixed-sediment component suggestive of postdepositional disturbance.

Lithofacies 4 represents sedimentation in a lower continental slope environment with a strong glacigenic influence. Sandy mud and muddy diamicton with clast clusters can be interpreted as hemipelagic sediment with ice-rafted debris (IRD), whereas some of the stratified clast-poor sandy diamicton and sandy mud could have originated as gravity flows.

3.3. Diagenesis

Diagenetic features at Site U1603 include iron sulfide minerals and carbonate concretions. The iron sulfide minerals are typically associated with sand laminae or blebs, forming prominent black laminae or patches in cores. They are often highlighted on X-ray images by dense material. Thin section analysis shows that the iron sulfides form fine coatings on grains, with biotite grains being most affected (Figure F10A). A few calcite-cemented concretions were observed in Sections 400-U1603A-10H-2, 400-U1603B-22F-3, and 400-U1603C-8R-2. In these concretions, intergranular cementation aided in the preservation of primary sedimentary structures such as graded fine sand and silt laminae (Figure F10B).
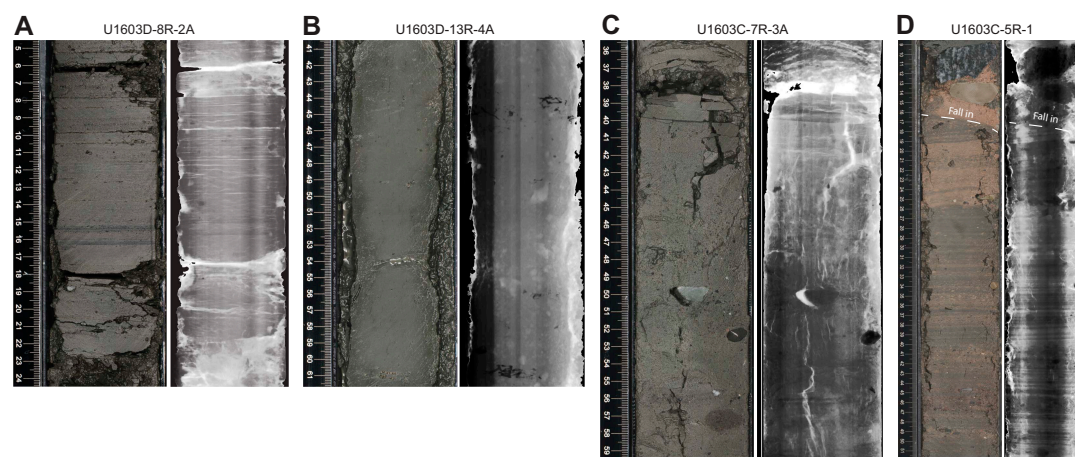
Figure F9. Lithofacies 4 (diamicton and sandy mud with common clasts), Holes U1603C and U1603D. SHIL and XSCAN pairs showing (A) laminated sandy mud with dispersed clasts, (B) bioturbated sandy mud, (C) crudely stratified diamicton, and (D) interstratified sandy mud and diamicton. Note the core disturbance (fall-in) near the top.

In Holes U1603A, U1603C, and U1603D, intervals of featureless or slightly laminated mud are often associated with color banding, alternating reddish and greenish layers, which may be associated with change in the iron oxidation state in sediments (see **Geochemistry**).

3.4. Smear slide and thin section analysis

A series of smear slides were taken during core description to ascertain the characteristics and composition of mud and very fine sand. Clay was too fine grained for mineralogical identification using petrographic methods. With the exception of samples discussed below, silt- and sand-sized grains are of terrigenous origin, dominated by quartz and feldspar minerals, with lesser amounts of mica, amphibole, and other accessory grains. Grains are typically angular to subangular, and minerals such as feldspar show no signs of alteration. Smear slides of calcareous mud intervals were also prepared and show that they are dominated by clay- to silt-sized fragments and rhombs of calcite and dolomite. Quartz, feldspar, and clay are present in minor amounts.

To determine the composition of prominent black laminae and blebs in mudstone and interlaminated mudstone–sandstone facies, a grain mount was made of black-coated, unconsolidated sand grains enclosed in a bleb (Sample 400-U1603A-8H-2W, 1–4 cm; TS01). Petrographic examination under transmitted and reflected light shows the black material to be opaque with an amorphous or cubic to stellate habit and pale yellow reflectance, consistent with iron sulfide minerals such as pyrite. Mica (possibly biotite) grains are most affected by pyritization, with quartz, feldspar, and accessory minerals being less affected. Of note, many of the feldspar grains in this sample were undergoing alteration (e.g., sericitization).

To preliminarily assess the composition of IRD, grain mounts were made from pebbles that were prominent in the biostratigraphy core catcher sample (400-U1603B-26F-CC, 23–28 cm; TS02 and TS04). This interval is composed of Lithofacies 2 (calcareous mud). The pebbles, typically subrounded, are dominated by fragments of variably dolomitized limestone and dolostone. Fragments of plutonic igneous rocks, chert, sandstone, and siltstone occur in relatively minor amounts. Some carbonate clasts contain altered fossils, including a coral (likely Paleozoic), brachiopod shell fragments, and a probable trilobite fragment, along with peloids and recrystallized shell debris. One clast contains silicified ooids. Dolomitization style is variable, ranging from finely crystalline to coarsely crystalline to saddle (hydrothermal) dolomite. In one sandstone clast, framework grains are rimmed by hematite.

3.5. Clay and bulk mineralogy results

XRD analyses were performed on 11 powdered bulk samples from Holes U1603A–U1603C, with sample selection based on major lithologic changes. In addition, 11 samples were taken from Holes U1603C–U1603E to determine the clay mineral compositions in Lithostratigraphic Units I, III, and IV and Subunit IIB. A qualitative and ratio-based summary of XRD results is given in Tables **T3** and **T4** for bulk and clay compositions, respectively.
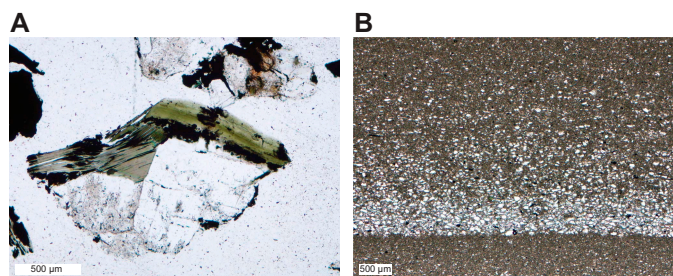
Figure F10. Diagenetic features, Holes U1603A and U1603B. A. Igneous rock fragment containing feldspar (clear) and biotite (green), which has been partially coated by iron sulfide (black/opaque) (400-U1603A-8H-2, 1–4 cm; PPL). B. Carbonate concretion that preserves fining-upward structures in the interlaminated mud and sand facies (400-U1603B-8R-2, 34–36 cm; PPL). The silt fraction is dominated by angular grains of quartz and feldspar, with minor biotite. Biotite grains are oriented parallel to laminae, giving a platy appearance in cross section.

The analyses of bulk samples in Hole U1603A were performed on three of the main identified lithofacies: mud, calcareous mud, and diamicton and sandy mud with common clasts. A supplementary bulk analysis was performed on a concretion found in Section 10H-2. The mud facies in Unit I sampled in Section 5H-4 is dominated by quartz with common feldspars and plagioclase. In addition, clay XRD analyses performed on material from Hole U1603E from Lithofacies 1 in Unit I show dominant illitic composition. Bulk analyses of the calcareous mud facies (Lithofacies 2) sampled in Sections 400-U1603A-5H-6 and 11H-5 indicate that quartz is still abundant, but calcite and dolomite are also identified as common phases. The concretion in Section 10H-2 contains traces of dolomite, likely occurring as intergranular cement.

Analyses of bulk samples in Hole U1603B specifically targeted calcareous mud (Lithofacies 2) and diamicton (Lithofacies 4). Based on samples of Lithofacies 2 from Sections 26F-3 and 26F-CC, dolomite and calcite are abundant phases in the calcareous mud, along with quartz. For Lithofacies 4, the sample from Section 2H-6 contains magnesium calcite in abundance, whereas the sample from Section 26F-4 is dominated by dolomite.

In Hole U1603C, samples for bulk XRD analysis were collected from Sections 3R-2 and 5R-2 (base of Subunit IIB) and Section 9R-2 (top of Unit III). All samples present a similar composition of abundant quartz and common feldspars (including plagioclase) in Lithofacies 1 and 3. XRD analyses for clay minerals were performed for Lithofacies 1 (mud) from Sections 2R-2 and 5R-2 in Sub-

Table T3. XRD results from bulk samples, Site U1603. Semiquantitative assessment of mineral abundance based on a comparison of peak intensities. XRD signatures are not linearly proportional to real mineral abundances. The approximate abundances are as follows: A = abundant (>30%), C = common (10%–30%), F = few (3%–10%), R = rare (<3%). **Download table in CSV format.**

Core, section, interval (cm)	Sample type	Quartz	K-feldspar	Plagioclase	Illite	Kaolinite	Smectite	Calcite	Mg-calcite	Dolomite	Augite	Amphibole	Halite	Pyrite
400-U1603A-														
5H-4, 36–37	Bulk	A	C	C	F	R								
5H-6, 102–103	Bulk	A	F	C	R	R		C		C				
10H-2, 121–122	Bulk	C	F	F	R					R	A			
11H-5, 104–105	Bulk	A	F	F	R	R		C		C				
400-U1603B-														
2H-6, 55–56	Bulk	C	F	F	R	R			A	F				
26F-3, 88–89	Bulk	C			R	F		A		A				
26F-4, 4–5	Bulk	R								A				
26F-CC, 17–18	Bulk	A		R	R	R		C		A				
400-U1603C-														
3R-2, 21–22	Bulk	A	C	C	F	R				R	R	F	R	R
5R-2, 10–11	Bulk	A	C	C	F	R	R			R	R	R	R	
9R-2, 116–117	Bulk	A	C	C	F	R				R	R	R	R	

Table T4. XRD results from the glycolated clay fraction (<4 µm), Site U1603. Counts refer to peak intensities following background subtraction. Clay-mineral ratios are based on peak intensities, which are not linearly proportional to mineral concentrations. **Download table in CSV format.**

Core, section, interval (cm)	Sample type	Kaolinite (7.1 Å counts)	Illite (10 Å counts)	Chlorite (14 Å counts)	Smectite (16.9 Å counts)	Chlorite 14 Å vs. Illite 10 Å	Kaolinite 7.1 Å vs. Illite 10 Å	Smectite 16.9 Å vs. Illite 10 Å
400-U1603C-								
2R-2, 19–20	Clay glycolated		10,420	2,639		0.25		
5R-2, 51–52	Clay glycolated		10,918	2,998	2,157	0.27		0.20
7R-2, 61–62	Clay glycolated		19,401	3,639	1,129	0.19		0.06
8R-2, 43–44	Clay glycolated		6,531	476		0.07		
9R-2, 19–20	Clay glycolated		15,523	2,372	1,410	0.15		0.09
400-U1603D-								
2R-2, 48–49	Clay glycolated	2,034	4,167				0.49	
5R-CC, 2–3	Clay glycolated		4,149	540	470	0.13		0.11
7R-1, 118–119	Clay glycolated		7,772	1,424	811	0.18		0.10
8R-5, 54–55	Clay glycolated	3,445	7,697		3,583		0.45	0.47
400-U1603E-								
2H-2, 47–48	Clay glycolated	805	1,815				0.44	
2H-3, 47–48	Clay glycolated		11,775	1,569		0.13		

unit IIB and from Section 7R-2 in Unit III. All samples show a dominantly illitic composition with chlorite as a secondary component. A similar composition characterizes Lithofacies 3 (interlaminated to interbedded mud and sand) and Lithofacies 4 (sandy mud with common clasts) in Unit III, based on analysis of samples from Sections 8R-2 and 9R-2. Smectite is a trace component in samples from Sections 5R-2, 7R-2, and 9R-2.

For Hole U1603D, clay XRD analyses were performed to investigate the clay mineralogy of Lithofacies 1 within Unit III. All samples are characterized by a primarily illitic composition. Smectite is present in greater abundance downhole (e.g., Section 8R-5). Kaolinite is a common mineral in two samples (Sections 2R-2 and 8R-5).

3.6. Preliminary depositional interpretation

Site U1603 recovered a sequence of Holocene to Early Pleistocene sediments from the continental slope and base of slope offshore the northwest Greenland margin. Unit I and Subunits IIA and IIB reveal a complex mixture of depositional processes on the continental slope that include suspension settling from plumes, turbidity current and contour current processes, and ice rafting. Interbedded diamicton and stratified sandy mud (Units III and IV) indicate the glacigenic origin of the sediments and may record ice sheet processes that occurred on the shelf. Several calcareous mud intervals in an otherwise siliciclastic-dominated succession may suggest episodes of variable sediment provenance in the depositional system. A short sequence containing foraminifera-bearing mud (Unit IV) suggests a prolonged interval of relatively enhanced productivity in open-marine conditions during the Early Pleistocene.

4. Biostratigraphy

4.1. Biostratigraphy and paleoenvironment

Core catcher samples from Holes U1603A–U1603D, together with additional samples from within cores, were examined for foraminifera, diatoms, dinoflagellate cysts (dinocysts), and other palynomorphs. The additional samples were taken from cores where variations in lithology were observed as an attempt to identify microfossil-rich horizons. Sampling targets included intervals of massive muds, increased bioturbation, and muds with dispersed clasts that coincided with low natural gamma radiation (NGR) values, as well as grayish brown and medium greenish gray carbonate-rich intervals. Mudline samples from Holes U1603A and U1603F were also examined. Cores from Holes U1603E and U1603F, which provide a second copy of the uppermost ~130 m of the cored section, were not examined. Observations of foraminifera from palynomorph and diatom slide preparations were integrated in the overall foraminifera evaluations.

The muds and interlaminated sands and muds typical of Site U1603 are generally barren of in situ microfossils besides a few intervals where some groups become abundant (Figure **F11**). Where foraminifera appear, they remain as rare occurrences, except in two distinct intervals in Cores 400-U1603B-22F and 400-U1603D-13R where they are common. Diatoms were found in about 6% of all samples examined, with trace to rare amounts of specimens and species. Palynomorph preparations revealed persistent contributions of phytoclasts and reworked terrestrial pollen and spores. The observed microfossil specimens and assemblages for all groups are typical of cold-water polar environments, and in situ dinoflagellate species are typical of coastal or neritic environments. Observed specimens and assemblages are broadly consistent with a Pleistocene age. The species have long stratigraphic ranges and provide limited age control.
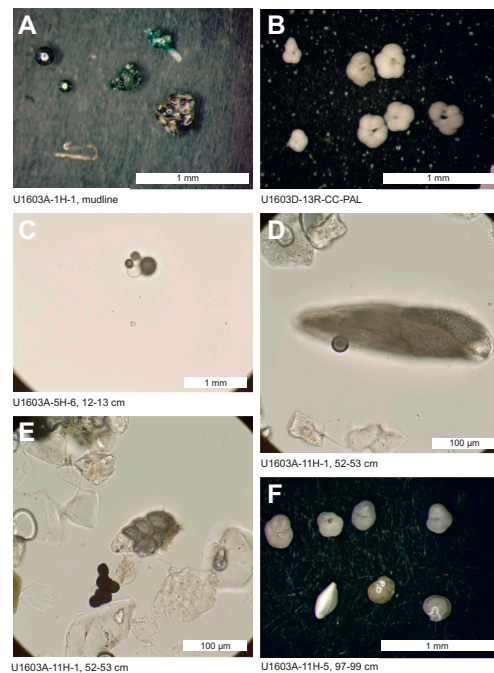
4.1.1. Foraminifera

Two mudline samples were examined for Holes U1603A and U1603F. Both contain abundant oxidized metallic grains and fine quartz sand (Figure **F12**). Sample 400-U1603A-1H-1, 0 cm, which yielded an extremely small sand sample, contains a few large diatoms but no foraminifera. Also of note are two tektites and several clasts of green and brown glass with indications of a bubble texture (Figure **F12A**). Mudline Sample 400-U1603F-1H-1, 0 cm, contains diverse biogenic grains, including radiolarians, abundant large (100–200 μm) centric diatoms, setae of the diatom *Chaeto-*

ceros spp., and rare agglutinated benthic foraminifera including *Hormosinelloides guttifera* and *Textularia earlandi* (Figure **F13A–F13C**).

All lithologies that characterize Site U1603 were challenging to disaggregate, especially in the uppermost 5–10 cores of Hole U1603A where muds dominate (Figure **F11**). Because of the high
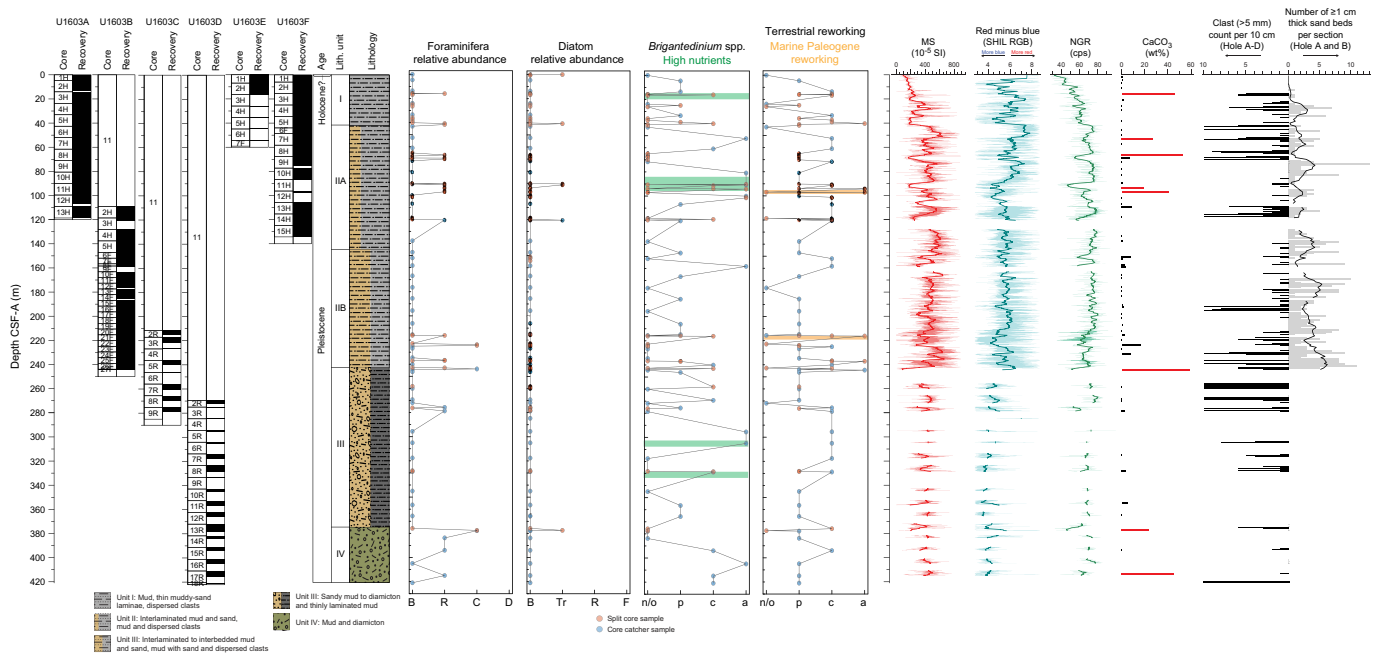
Figure F11. Trends across fossil groups as they relate to various physical and sedimentological measurements of the cores, Site U1603. Foraminifera: B = barren, R = rare (<5%), C = common (5%–50%), D = dominant (>50%). Diatoms: B = barren, Tr = trace (<2%), R = rare (2%–5%), F = few (5%–10%). Dinocysts: n/o = not observed, p = present (1%–5%), c = common (5%–20%), a = abundant (>20%). cps = counts per second.

Figure F12. Notable grains, foraminifera assemblages, and specimens, Holes U1603A and U1603D. A. Tektites and clasts of green and brown glass from the mudline. B. Forms of *N. pachyderma*. C. Embryonic (four chambers) specimen of *N. pachyderma*. D. Benthic foraminifera *Buliminella elegantissima*. E. Benthic foraminifera *Bolivina arctica*. F. Planktonic and benthic foraminifera in a >63 µm residue.

clay content in much of the recovered sediment, the sieved >63 µm residues are often small, becoming significantly larger in sand-rich and diamicton intervals. Figure **F13D–F13M** illustrates the range in variability of >63 µm residues, emphasizing the dominance of lithics, mineral grains, and other biological materials. Quartz typically dominates the sands, which is well sorted in some intervals (Figure **F13H, F13O**), together with transported lithic clasts of a variety of lithologies, including typically gray carbonates in variable quantities (Figure **F13E, F13I**). Other notable grains are extremely rounded quartz grains that are common in many samples, as well as grains of pyrite-cemented clusters of quartz sand (Figure **F13N**).

Of the processed foraminifera samples, 41 of the 49 core catcher samples from Site U1603 are devoid of foraminifera and 8 have rare to common foraminifera. Of the 54 additional samples taken from targeted intervals, 32 are also devoid of foraminifera. Rare to common calcareous foraminifera appear in 22 residues. The >125 and 63–125 µm sieved fractions were examined separately; however, because of the typically low numbers of foraminifera, observations are combined. Planktonic and benthic foraminifera are also presented together here.

The core catchers and additional samples in which rare foraminifera (planktonic and benthic) are observed are shown in Table **T5**. A single species of planktonic foraminifera was recorded: the
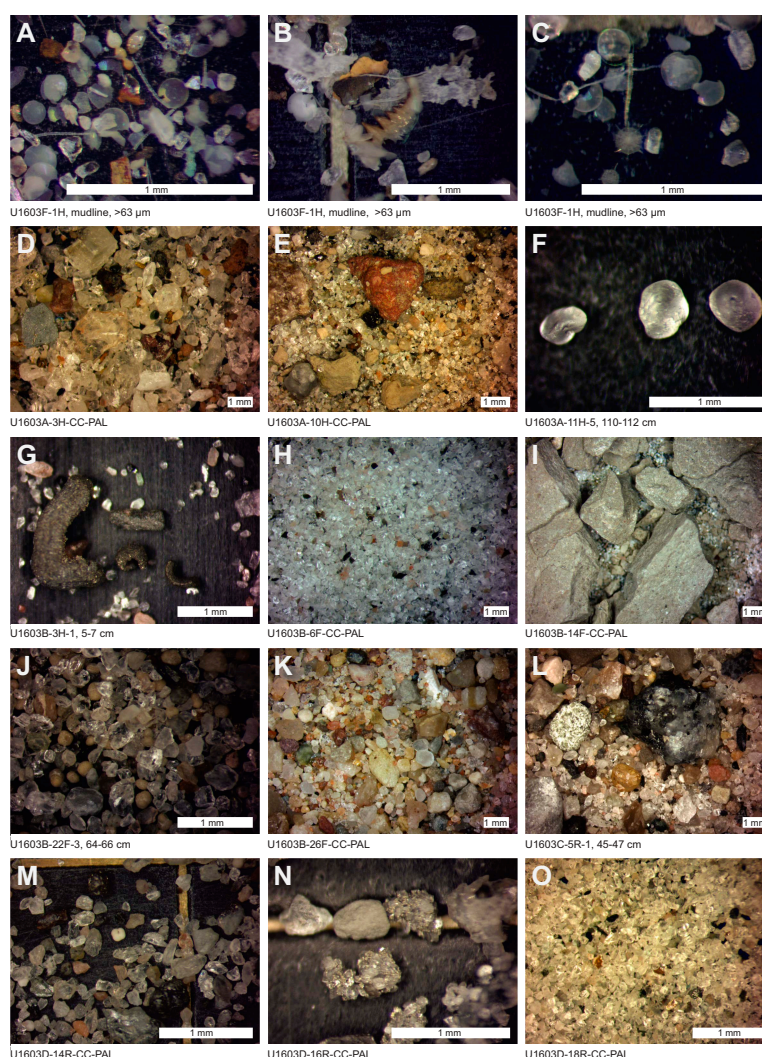
Figure F13. Sand fraction samples and selected grain components, Site U1603. A–C. Mudline (recent) samples containing oxidized metallic grains, fine quartz sand, large centric diatoms, and diatom setae (strands). Lithic clasts vary from being dominated by granitic/mineral-rich to combinations of minerals together with (D, E, K, L) dolomite and/or (I) fine-grained limestone gravel or granules and other sedimentary rocks. F. Rounded quartz grains. G. Pyritized burrows. H, O. Samples dominated by sorted quartz sand. J, M. Foraminifera-bearing samples. N. Pyrite-cemented clusters of quartz sand.

polar specialist *Neogloboquadrina pachyderma*. This is most often seen as only a couple of specimens per sample (Figure **F13M**) but with some notable exceptions (Figure **F13J**) in Samples 400-U1603A-8H-6, 25–27 cm; 400-U1603B-22F-3, 64–66 cm, and 22F-4, 45–47 cm; and 400-U1603D-13R-4, 119–121 cm, and 13R-CC where *N. pachyderma* is more abundant (Figure **F13J, F13M**). A variety of *N. pachyderma* morphotypes are observed that match the five-morphotype classification of Eynaud et al. (2009) and El Bani Altuna et al. (2018). Noteworthy in Section 400-U1603A-8H-6 and Core 400-U1603D-13R is the common occurrence of a large five-chambered morphotype with an open umbilicus. This could be Nps-4 of El Bani Altuna et al. (2018), but it is also comparable to *Neogloboquadrina dutertrei* (although lacking an umbilical tooth) and *Neogloboquadrina atlantica*. This sample also contains teratoid *N. pachyderma* specimens, which display irregular coiling and/or aperture placement. These are reminiscent of *Neogloboquadrina polusi* (Androsova, 1962), which was also reported by Aksu (1985) in the central Arctic Ocean. *N. polusi* is currently synonymized under *N. pachyderma* (Brummer and Kučera, 2022). Preliminary *N. pachyderma* coiling counts in Samples 400-U1603D-13R-CC and 13R-4, 119–121 cm (calculated as ~5% dextral) suggest that the planktonic assemblages are monospecific and do not contain the warmer water species *Neogloboquadrina incompta*. It is noted that the sand fraction of the bottom core catcher sample (13R-CC; 420.92 m CSF-A) is composed almost entirely of an extremely well sorted, foraminifera-barren fine sand falling in the 63–125 µm sieved fraction. This particle sorting is suggestive of current winnowing and a contourite facies (Figure **F12**).

Similarly, much of the cored sequence at Site U1603 lacks benthic foraminifera, especially the interlaminated sands and muds. Even in the most foraminifera-bearing samples, only single to a few benthic foraminifera specimens are observed, with the exception of Samples 400-U1603D-13R-4, 119–121 cm, and 13R-CC and 400-U1603B-27F-CC, where specimens are sufficiently abundant (>100 specimens) to be considered an assemblage (Table **T5**). In Sample 400-U1603D-13R-4, 119–121 cm, the ecologically flexible *Cassidulina reniforme* is most common, together with common *Stetsonia horvathi* and rare *Cassidulina neoteretis/teretis*, the latter being typical of chilled Atlantic waters (Jennings and Helgadottir, 1994; Cage et al., 2021). Sample 400-U1603B-27F-CC contains dominant *Elphidium clavatum*, a few examples of the agglutinated benthic species *Recurvoides* spp., and rare *Islandiella inflata*. *E. clavatum* is typical of Arctic glaciomarine environments in shelf and slope settings without perennial sea ice cover but with seasonal ice (Hald and Korsun, 1997; Jennings et al., 2020). Other species observed at Site U1603 include the Arctic species *Buliminella elegantissima*, *Stainforthia feylingi*, *Bolivina arctica*, *Triloculina trihedra*, and scarce *Oridorsalis umbonatus*. These foraminifera species are typical of Holocene to Pleistocene Arctic shelf and slope environments. They are regarded as opportunists associated with sea ice–influenced environments, whereas *O. umbonatus* is ubiquitous in deeper water settings globally (Seidenkrantz, 2013). Agglutinated benthic species are recorded in one sample (400-U1603B-27F-CC). These benthic assemblages are similar to those found by Kaminski et al. (1989) at Ocean Drilling Program Site 645 and Feyling-Hansen (1976) in the Clyde Foreland Formation (western Baffin Bay), and they are consistent with a Pleistocene age.

In the foraminifera-rich samples, foraminifera were also detected in the sedimentology smear slides and the diatom and dinoflagellate slides. These contained a number of well-preserved examples of *N. pachyderma* as juveniles, having only six to seven chambers in the test, and embryonic stages, involving combinations of two or three small globular chambers (Figure **F12C**). The Sample 400-U1603A-11H-1, 52–53 cm, diatom slide contained specimens of the benthic foraminifera *B. elegantissima* and *B. arctica* (Figure **F12D, F12E**). In five cases, foraminifera appeared in palynology slides although they did not appear in the >63 µm residues (Samples 3H-2, 56–58 cm, and 11H-1, 6–8 cm, and 400-U1603B-4H-CC, 21F-1, 42–44 cm, and 26F-3, 68–70 cm). These slides record common to abundant occurrences of foraminifera specimens smaller than the typical 63 µm preparations routinely examined by the foraminifera team. This finding of small foraminifera species and subadult forms in superfine-fraction preparations in this slope setting has potential ecological/environmental implications and raises questions about calcite preservability on the northwest Greenland margin. It also has relevance to questions about the life history and trans-

Table T5. Foraminifera-containing intervals observed from sand fraction samples (>63 µm), Site U1603. **Download table in CSV format.**

portation of *N. pachyderma* in extreme Arctic slope and shelf settings, including the possibility of planktonic foraminifera nurseries or refugia in such regions or advection of juvenile forms by Atlantic water entering Baffin Bay.

The general scarcity of foraminifera at Site U1603 suggests combinations of calcite dissolution and climatic conditions prohibitive to planktonic foraminifera production and/or preservation in seafloor sediments or the sediment pile. Extensive seafloor dissolution of foraminifera shells in Baffin Bay has been observed under recent interglacial conditions, despite the fact that planktonic foraminifera live in the water column (Stehman, 1972). Even where we do find foraminifera, it is possible that dissolution-susceptible species, including *Globigerina bulloides*, which occurs in the water column of Baffin Bay (Stehman, 1972), have been selectively dissolved.

Overall, the foraminifera from Site U1603 yielded species consistent with a Pleistocene age. Although the sporadic foraminifera occurrence is not appropriate for identifying specific bioevents useful for dating, the occurrence of a mature *N. pachyderma* assemblage in Section 400-U1603D-13R-CC (377.86 m CSF-A) implies the cored sequence down to that level is younger than 1.82 Ma. This constraint is based on the established timing of the first common occurrence of *N. pachyderma* biohorizons (B Common *N. pachyderma* sinistral), which has been calibrated to the paleomagnetics in the North Atlantic (Expedition 395).

4.1.2. Diatoms

We examined 118 Site U1603 samples, consisting primarily of core catcher samples, for diatoms. Diatoms were observed in trace amounts in seven samples at Site U1603. Except in Samples 400-U1603A-1H-1, 1 cm, 5H-6, 12–13 cm, 11H-1, 52–53 cm, and 11H-1, 126–127 cm; 400-U1603B-3H-CC; 400-U1603D-13R-4, 119–120 cm; and 400-U1603F-1H-1, 0 cm, the great majority of core catcher and section-half samples are virtually barren of diatoms (Figure **F11**). Only fragments of diatoms, which could not be confidently identified, were observed in a few samples. The morphology of most of the fragments indicates that they were probably derived from *Coscinodiscus* species.

Mudline Samples 400-U1603A-1H-1, 1 cm, and 400-U1603F-1H-1, 0 cm, contain trace to rare amounts of moderately to poorly preserved diatoms, including *Actinocyclus curvatulus*, *Rhizosolenia hebetata* f. *hebetata*, *Chaetoceros* spp. and resting spores, *Melosira arctica*, and *Navicula* spp. Observed species are characteristic of the modern assemblages living in the Arctic region. *Coscinodiscus marginatus* is present in trace amounts in Samples 400-U1603A-5H-6, 12–13 cm, and 11H-1, 52–53 cm. These samples also contain trace amounts of *Coscinodiscus* species fragments. We also observed a single specimen of *Coscinodiscus oculus-iridis* in Sample 11H-1, 52–53 cm. Two specimens of *Stephanopyxis turris* were observed in Section 400-U1603B-3H-CC. A few specimens of *Podosira* sp. (*montagnei*?) were seen in Samples 400-U1603A-11H-1, 52–53 cm, and 11H-1, 126–127 cm; 400-U1603B-3H-CC; and 400-U1603D-13R-4, 119–120 cm.

Trace occurrence and poor preservation of diatoms at Site U1603 preclude any stratigraphic analysis (Figure **F11**). The specimens seen are typical of Arctic environments, except *S. turris*, although too few specimens were observed to discern paleoenvironmental conditions at Site U1603. The virtual absence of diatoms in these sediments may have paleoceanographic significance or may signify extensive dissolution and/or diagenesis.

4.1.3. Palynology

In total, 52 core catcher samples and 51 additional samples from targeted intervals were processed following the procedure described in **Biostratigraphy** in the Expedition 400 methods chapter (Knutz et al., 2025).

Overall, palynomorphs, and notably the dinocysts among them, were found to be scarce except for a few intervals, and no quantitative analyses were conducted on board. Occurrences of palynofacies categories and palynomorphs for all samples from Site U1603 are listed in Table **T6**.

Table T6. Palynofacies categories and palynomorphs for all samples, Site U1603. **Download table in CSV format.**

All dinoflagellate cysts species observed in the analyzed material are consistent with a Pleistocene age. Preservation of in situ dinocysts is good in all samples, although abundances are low across the entire studied interval. Rarity of palynomorphs in the Quaternary in Arctic marine settings can be attributed to the small number of dinoflagellates around the Arctic that form fossilizable cysts (Okolodkov, 1998) and the general ecological preference of dinoflagellates for warmer waters (e.g., de Vernal et al., 2013).

Dinocyst species belonging to the genus *Brigantedinium* spp. are present in 47 of the 103 samples from throughout the entire interval (Figure **F11**). Highest abundances of *Brigantedinium* spp. are observed in Sample 400-U1603A-6H-CC and samples from Sections 11H-1 and 12H-1; Sample 400-U1603B-8F-CC; and Samples 400-U1603D-5F-CC, 6F-CC, and 16R-CC. Other species of dinocysts identified include *Echinidinium sleipnerensis*, *Echinidinium delicatum*, *Echinidinium granulatum*, *Islandinium brevispinosum*, and *Islandinium minutum* (Figure **F14A, F14B, F14D, F14E**). Intervals with higher abundances of these dinocysts include Samples 400-U1603A-3H-2, 56–68 cm, and 400-U1603D-8R-5, 37–39 cm, and samples from Sections 400-U1603A-11H-1, 400-U1603D-5R-CC, and 400-U1603A-10H-CC. In Sample 3H-2, 56–68 cm, a type of *Echinidinium* with slightly fewer and longer processes than *E. sleipnerensis* is present. This specimen resembles *Echinidinium* sp. A (Radi et al., 2013), which was previously observed in last interglacial (Upper Pleistocene) deposits from the Norwegian Sea (Radi et al., 2013).

Other in situ palynomorphs include *Leiosphaeridia* in 29 of the 103 samples. This acritarch is most abundant at the contact margin between seasonal sea ice and pack ice in the Arctic (Mudie, 1992). Highest abundances of *Leiosphaeridia* are found in Samples 400-U1603B-8F-CC; 400-U1603D-5R-CC; 400-U1603C-9R-CC; 400-U1603A-11H-3, 90–92 cm, and 10H-CC; and all sam-
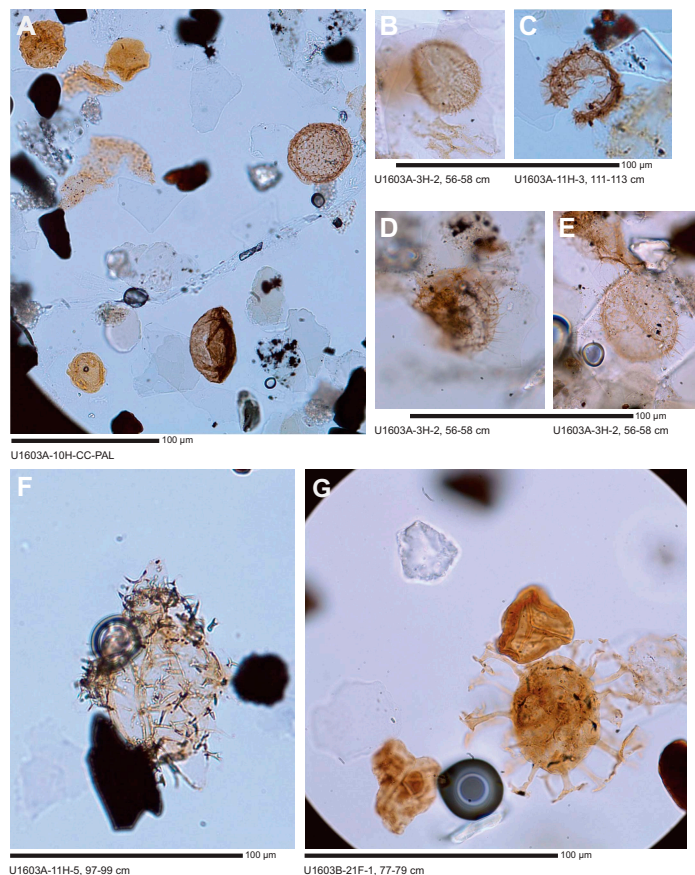
Figure F14. In situ and reworked dinocysts, Site U1603. A. Reworked pollen and spores and *Islandinium minutum*. B. *Echinidinium sleipnerensis*. C. Prasinophyte algae *Cymatiosphaera*. D, E. *Echinidinium* sp. A (Radi et al., 2013). F, G. Reworked dinocysts of Paleogene age: (F) *Wetzelliella* spp. and (G) *Hystrichosphaeridium tubiferum*.

ples from Section 400-U1603C-5R-1. Additionally, the prasinophyte algae *Cymatiosphaera* (Figure **F14C**) is found in Samples 400-U1603A-11H-3, 111–113 cm, and 10H-CC.

In addition to in situ palynomorphs, varying abundances of reworked (mostly terrestrial) palynomorphs are present in all samples, which is a common characteristic of sites at continental margins proximal to ice sheets, like Site U1603 (Smelror, 1999). The highest rates of terrestrial reworking are found in Samples 400-U1603B-26F-CC; 400-U1603C-5R-1, 56–58 cm; 400-U1603B-21F-1, 77–79 cm; and 400-U1603A-11H-1, 126–128 cm, 11H-3, 80–82 cm, 11H-3, 90–92 cm, and 11H-3, 111–113 cm. These include bisaccate pollen, other gymnosperm pollen, and wide varieties of trilete fern spores (Figure **F14A**). Future study by a pollen and spore specialist would be a valuable contribution to constrain the age of the reworked sediments.

In addition to terrestrial reworking, some samples yielded large amounts of marine reworking, represented by high numbers of dinocysts of a Paleogene age. The assemblage includes various species belonging to the genera *Cordosphaeridium*, *Wetzelliella* (Figure **F14F**), *Spiniferites*, and *Hystrichosphaeridium* (Figure **F14G**), among others. Two intervals that are marked by this pulse of reworking are from Section 400-U1603A-11H-3 and Sample 400-U1603B-21F-1, 77–79 cm. These reworked sediments have a great potential to further constrain the source of reworked material.

4.1.3.1. Provenance study

To constrain the origin of the reworked marine sediments of Paleogene age, clasts from one interval have been sampled and processed separately using the same method that was used for other palynology samples. Clasts sampled originated from Sample 400-U1603C-5R-1, 45–47 cm. One brown sedimentary clast and one black sedimentary clast were analyzed. The brown clast contains abundant organic matter aggregates, plant material, and some poorly preserved bisaccate pollen. This implies a terrestrial source for which the age could not be constrained. The black clast consists of a variety of different minerals, a few organic matter aggregates, and rare phytoclasts. Palynomorphs are very rare, although one poorly preserved small cyst was identified. The source of this clast could not be determined based on these palynomorphs.

4.1.4. Marine sedimentary ancient DNA

A mudline sample (~10 g) was collected as a modern reference from Hole U1603A. Samples for sedimentary ancient DNA (sedaDNA) analysis were collected from Hole U1603E (Table **T7**) down to ~14 m CSF-A (6 samples on the catwalk; 3 in split core sections) and Hole U1603F (Table **T8**) down to ~132 m CSF-A (38 samples on the catwalk; 13 in split core sections) following the catwalk and the split core sampling methodologies (see **Biostratigraphy** in the Expedition 400 methods chapter [Knutz et al., 2025]). On the catwalk, samples were usually taken at the bottom of Sections 1, 3, and 5 if the sections were available and the section bottom was undisturbed. Additional samples were collected from the working half of split sections targeting nonstratified mud layers with few or no clasts, characterized by low MS and low NGR, predominantly above and/or below calcareous layers. Considering the lithology, all samples from Hole U1603E were taken within mud layers, and for Hole U1603F, 15 sedaDNA samples were taken within interlaminated sand(stone) and mud(stone), 1 within interlaminated sand(stone) and mud(stone) with dispersed clasts, 3 within interbedded sand(stone) and mud(stone), 25 in mud, 2 in mud with sand, 1 in sandy mud, 3 in mud with dispersed clasts, and 1 in mud with common clasts. All samples were immediately stored at −86°C. A total of 12 tracer samples were taken for Hole U1603E (Table **T9**) and 69 for Hole U1603F (Table **T10**). Trace amounts of perfluorodecalin (PFD) tracer were detected in the external sample from the bottom of Section 400-U1603E-1H-1 and in samples taken from liquid at

Table T7. Samples taken for sedaDNA analysis, Hole U1603E. **Download table in CSV format.**

Table T8. Samples taken for sedaDNA analysis, Hole U1603F. **Download table in CSV format.**

Table T9. Samples taken for PFD tracer analysis and run on the GC2 Agilent 6890N gas chromatograph, Hole U1603E. **Download table in CSV format.**

Table T10. Samples taken for PFD tracer analysis and run on the GC2 Agilent 6890N gas chromatograph, Hole U1603F. **Download table in CSV format.**
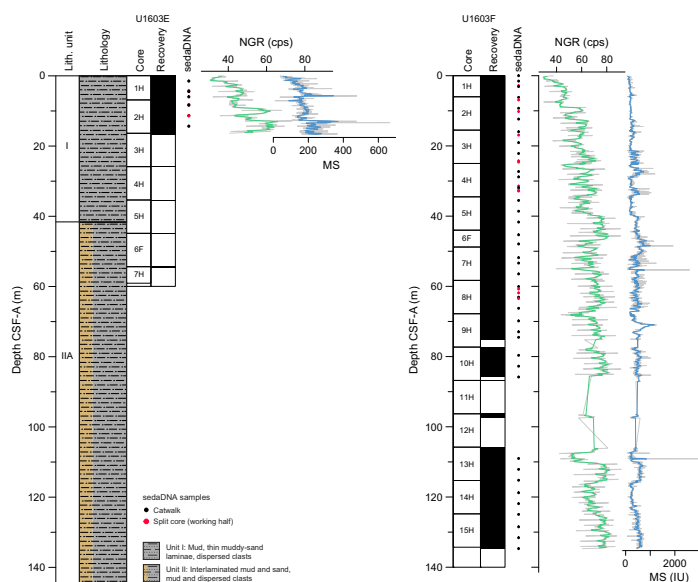
Figure F15. sedaDNA samples, Holes U1603E and U1603F. NGR: gray line = all whole-round measurements collected, green line = rolling average (50 cm window). cps = counts per second. MS: thin gray line = all MSP measurements collected using the SHMSL, blue line = rolling average (1 m window).

the top of cores from Hole U1603F, confirming the arrival of PFD at the drill bit (Figure **F15**). Overall, these results suggest a low risk of contamination by drill fluids with the APC system.

5. Paleomagnetism

Pass-through paleomagnetic measurements from Site U1603 were performed using the superconducting rock magnetometer (SRM) to investigate the natural remanent magnetization (NRM) on a total of 313 archive section halves. Measurements were not made on 16 archive section halves that had highly disturbed sediments, and no pass-through measurements were made on core catcher samples. All measurements on section halves were made at 2 cm intervals; we measured the initial magnetization and the magnetization following stepwise peak alternating field (AF) demagnetizations at 5, 10, 15, and 20 mT.

A total of 188 discrete cube samples were taken from the working section halves from Holes U1603A–U1603D. Generally, we collected one sample per section, avoiding visually disturbed intervals. Note that in paleomagnetic practice, samples are the objects that are taken (sampled) and specimens are the objects that are measured. In this case, the two objects are the same. We measured 54 specimens on the AGICO JR-6A spinner magnetometer and 146 specimens on the SRM. Some specimens were measured on both instruments to ensure cross-calibration.

5.1. Discrete sample measurements

A total of 188 discrete cube samples were collected from working section halves: 73 from Hole U1603A, 79 from Hole U1603B, 13 from Hole U1603C, and 23 from Hole U1603D. All were measured after stepwise demagnetization up to a peak field of 20 mT on either the JR-6A or the SRM. Of these, 71 specimens were measured after stepwise AF demagnetizations up to a peak field of 80 mT to assess the demagnetization behavior at higher peak fields. Examples of Zijderveld diagrams (Zijderveld, 1967) are shown in Figure **F16** for normally (Figure **F16A, F16B**) and reversely magnetized specimens (Figure **F16C, F16D**), along with plots of the remaining remanence versus AF demagnetization step (Figure **F16E–F16H**). In both normal and reversed polarity intervals, the

drill string overprint is typically removed by 15 mT; the preliminary magnetostratigraphy is based on the inclination from measurements of the 20 mT AF demagnetization step. Because the cores are not azimuthally oriented and the field at the site latitude is nearly vertical, declination was not used to constrain polarity.

We measured anisotropy of MS (AMS) and volume-normalized bulk MS using the AGICO MFK2 Kappabridge on 188 discrete specimens. The AMS data are reduced to a 3×3 tensor with eigenvalues (τ_1, τ_2, and τ_3) and eigenvectors (V_1, V_2, and V_3), where τ_1 is the maximum eigenvalue associated with eigenvector V_1 and $\tau_1 > \tau_2 > \tau_3$. These data provide useful information about possible disturbance of the specimens from geological processes, core recovery, or sampling. In an undisturbed sedimentary fabric, τ_F is approximately equal to τ_2, and the ratio can be used as a measure of disturbance. In Figure **F17A**, we plot the ratio of the two as a cumulative distribution function. For values close to unity, the sediments are undisturbed, but for ratios larger than about 1.02, we can infer that the sediments were disturbed either by sedimentary processes (e.g., slumping) (Schwehr and Tauxe, 2003) or by coring. We use this eigenvalue ratio to assign disturbance and plot the disturbed specimens as Xs.

We show the directions of the eigenvectors in Figure **F17B**. The direction of the minimum axis (blue circles) is expected to be vertical (center of the diagram) in most sediments, and this is the case for the vast majority of our specimens. However, some are quite deflected from the vertical;
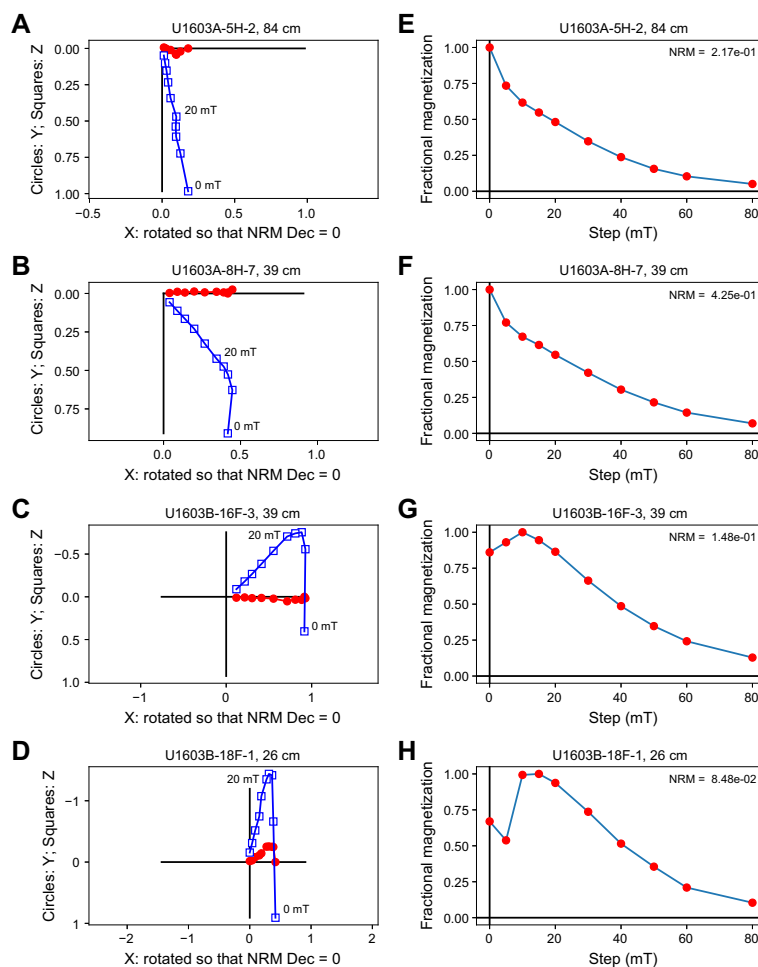
Figure F16. Representative progressive AF demagnetization behavior, Site U1603. A–D. Representative vector endpoint diagrams for (A, B) normal polarity and (C, D) reversed polarity specimens. Red dots = horizontal projections, blue squares = vertical projections. The drilling overprint is mostly removed by 20 mT. E–H. Magnetization remaining after progressive demagnetization to 80 mT for the same specimens as in A–D, normalized to the NRM (unit = A/m). The vertical downward direction of the drill string overprint is removed by 20 mT.

these likely suffered some disturbance of the sedimentary fabric related to uparching of the core, and their directions could therefore be suspect.

To examine the behavior of the eigenparameters versus depth, we plot the eigenvalues in Figure **F18A**, along with the ratio τ_1/τ_2 (L, lineation parameter of Balsley and Buddington [1960]; see also Chapter 13 of Tauxe [2010]) in Figure **F18C** and the inclination of V_3 in Figure **F18B**. Intervals with values of L significantly different from unity (e.g., Core 400-U1603A-12H) are likely disturbed either from sedimentary processes (slumping) or coring disturbance, and these are plotted as Xs in Figure **F18A**.

Anhysteretic remanent magnetization (ARM) was also measured on a subset of 45 discrete specimens from Holes U1603A and U1603B. We imparted an ARM with a peak 50 mT AF and 50 µT direct current (DC) field on specimens that had been demagnetized on all three axes at 80 mT. These measurements were compared with volume-normalized bulk MS (Figure **F19**). The relationship between ARM and MS is quasilinear, which suggests that the concentration of magnetic minerals is the primary control on both measurements and supports the use of normalized remanence for estimating relative paleointensity (RPI) (see **Age model**).

5.2. Archive-half measurements

Site U1603 archive section halves were stepwise demagnetized to 20 mT to remove the drilling overprint. Data were filtered as follows:

- All measurements within 10 cm of section ends were deleted to remove the edge effects associated with pass-through measurements.
- Intervals with drilling disturbances as defined by the disturbance intensity code of "moderately disturbed" or greater (see **Lithostratigraphy** in the Expedition 400 methods chapter [Knutz et al., 2025]) were removed.
- Core linescan images and X-radiographs in intervals of suspect directions were examined to assess where lithologic features such as dropstones or concretions necessitated removal of intervals.

Data from the 20 mT demagnetization step are shown in Figures **F20**, **F21**, **F22**, **F23**, **F24**, and **F25**. Unfiltered data are plotted with gray dots, and filtered data are plotted with black dots. Inclination and declination of discrete specimens, calculated from the remanent magnetization measured after the 20 mT AF demagnetization step, are shown as red stars if they were deemed undisturbed using the AMS eigenvalue discrimination approach; those that were disturbed are plotted as Xs.
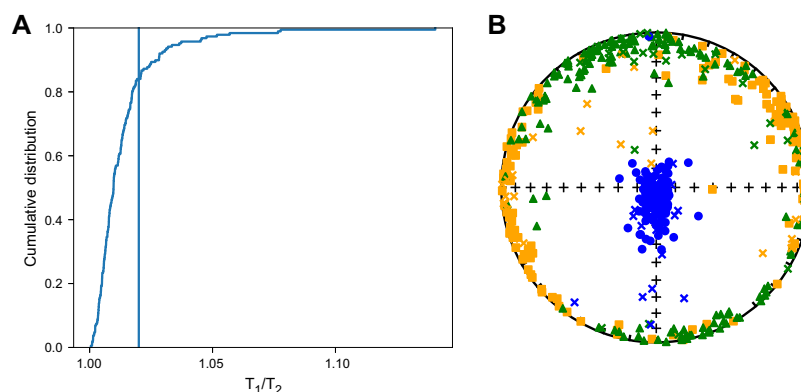

Figure F17. AMS data, Site U1603. A. Ratios of the maximum and intermediate eigenvalues (τ_1/τ_2) as a cumulative distribution. The vertical line at 1.02 is taken as the boundary between undisturbed (where the two are approximately equal) and disturbed fabrics. B. Equal area projections of the eigenvectors of the AMS ellipsoids. All directions are plotted in the lower hemisphere. Undisturbed specimens: orange squares = V_1 directions, green triangles = V_2 directions, blue circles = V_3 directions. For disturbed specimens, eigenvectors are plotted as Xs (orange = V_1; green = V_2; blue = V_3).

Inclinations from the filtered archive section half 20 mT step data are shown as kernel density plots in Figure **F26** and support the assumption that periods of both normal and reversed polarity were recovered at Site U1603. Most inclination magnitudes fall under expected (geocentric axial dipole [GAD]) values for the latitude of Site U1603 during normal (positive inclinations) and reversed (negative inclinations) polarities.

5.3. Magnetostratigraphy

Preliminary magnetostratigraphic interpretations are based on inclinations calculated from archive section half and discrete specimen measurements from the 20 mT AF demagnetization
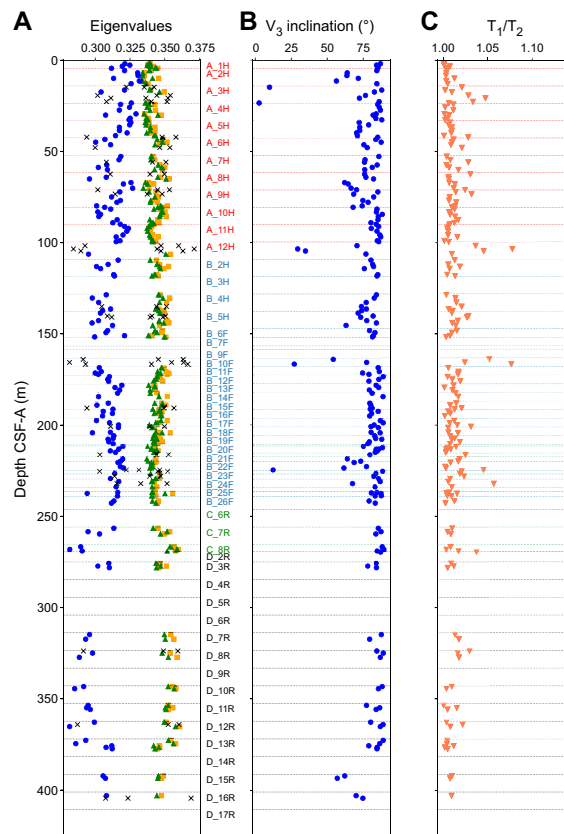
Figure F18. AMS parameters with depth, Site U1603. A. Eigenvalues. Orange squares = maximum eigenvalues (τ_1), green triangles = intermediate eigenvalues (τ_2), blue circles = minimum eigenvalues (τ_3). Disturbed specimens are plotted as Xs. B. Inclination of the eigenvector associated with the minimum eigenvalue (V_3), which is expected to be near vertical (90°) in undisturbed sediments. C. Ratio of τ_1/τ_2, which should be near unity in undisturbed sediments. Horizontal dashed lines = top depths of labeled cores.
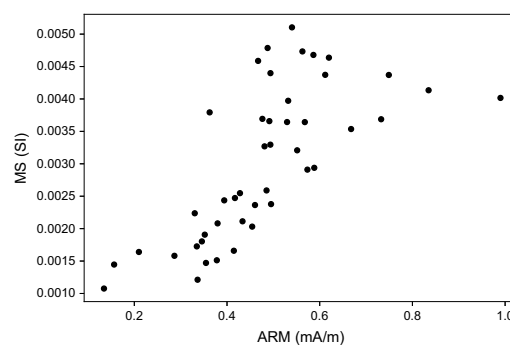
Figure F19. ARM versus bulk MS, Site U1603. The quasilinear relationship suggests that the concentration of magnetic minerals is the primary control of both measurements, supporting the use of normalized remanence for RPI estimates.
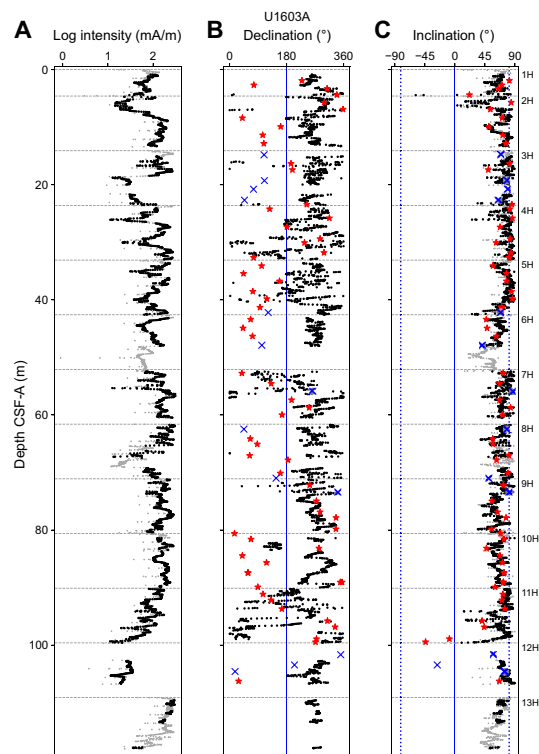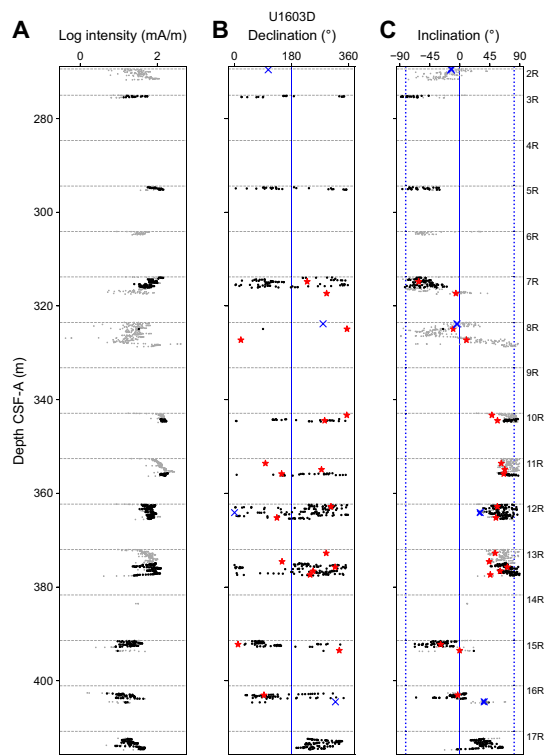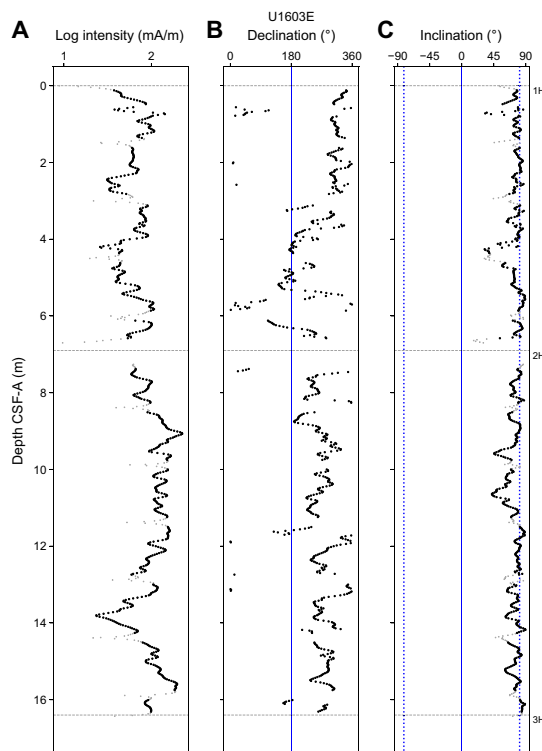
Figure F20. Archive section half (A) intensity of remanence, (B) declination, and (C) inclination after demagnetization to 20 mT, Hole U1603A. Section halves: gray dots = original (unedited) 20 mT step data, black dots = 20 mT step data after filtering to remove coring disturbance. Discrete specimens: red stars = undisturbed, blue Xs = disturbed based on AMS data. Declination values are rotated to a mean value of 180°. Inclinations: dashed blue lines = expected GAD values for normal and reversed polarities. Horizontal dashed lines = top depths of labeled cores.
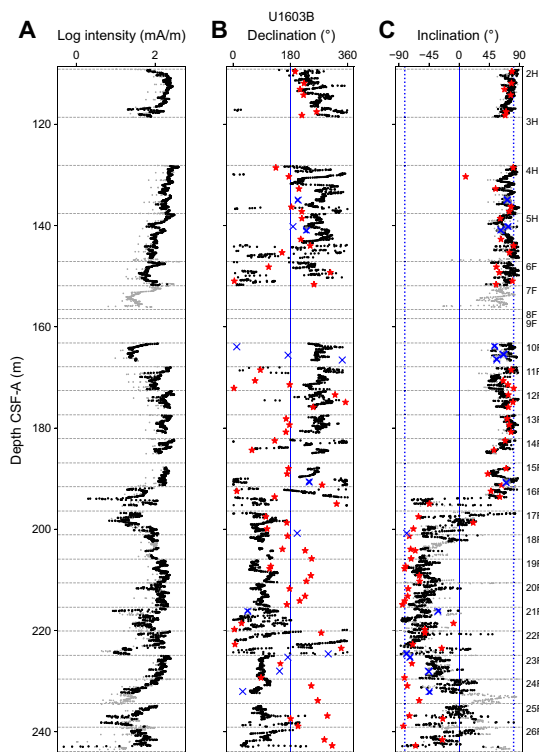
Figure F21. Archive section half (A) intensity of remanence, (B) declination, and (C) inclination after demagnetization to 20 mT, Hole U1603B. Section halves: gray dots = original (unedited) 20 mT step data, black dots = 20 mT step data after filtering to remove coring disturbance. Discrete specimens: red stars = undisturbed, blue Xs = disturbed based on AMS data. Declination values are rotated to a mean value of 180°. Inclinations: dashed blue lines = expected GAD values for normal and reversed polarities. Horizontal dashed lines = top depths of labeled cores.
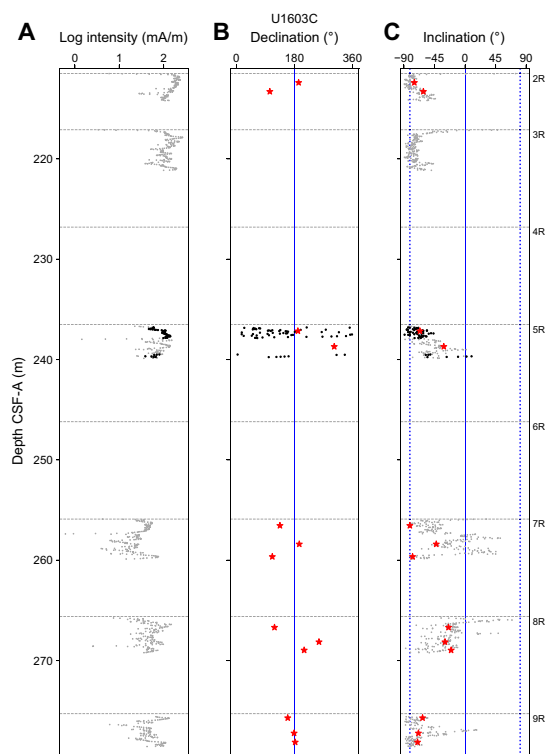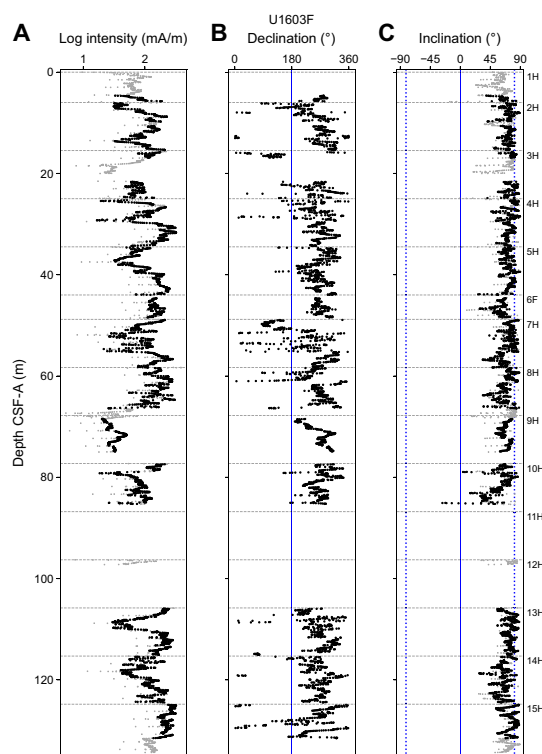
Figure F22. Archive section half (A) intensity of remanence, (B) declination, and (C) inclination after demagnetization to 20 mT, Hole U1603C. Section halves: gray dots = original (unedited) 20 mT step data, black dots = 20 mT step data after filtering to remove coring disturbance. Discrete specimens: red stars = undisturbed. Declination values are rotated to a mean value of 180°. Inclinations: dashed blue lines = expected GAD values for normal and reversed polarities. Horizontal dashed lines = top depths of labeled cores.


Figure F23. Archive section half (A) intensity of remanence, (B) declination, and (C) inclination after demagnetization to 20 mT, Hole U1603D. Section halves: gray dots = original (unedited) 20 mT step data, black dots = 20 mT step data after filtering to remove coring disturbance. Discrete specimens: red stars = undisturbed, blue Xs = disturbed based on AMS data. Declination values are rotated to a mean value of 180°. Inclinations: dashed blue lines = expected GAD values for normal and reversed polarities. Horizontal dashed lines = top depths of labeled cores.

Figure F24. Archive section half (A) intensity of remanence, (B) declination, and (C) inclination after demagnetization to 20 mT, Hole U1603E. Section halves: gray dots = original (unedited) 20 mT step data, black dots = 20 mT step data after filtering to remove coring disturbance. Declination values are rotated to a mean value of 180°. Inclinations: dashed blue lines = expected GAD values for normal and reversed polarities. Horizontal dashed lines = top depths of labeled cores.

Figure F25. Archive section half (A) intensity of remanence, (B) declination, and (C) inclination after demagnetization to 20 mT, Hole U1603F. Section halves: gray dots = original (unedited) 20 mT step data, black dots = 20 mT step data after filtering to remove coring disturbance. Declination values are rotated to a mean value of 180°. Inclinations: dashed blue lines = expected GAD values for normal and reversed polarities. Horizontal dashed lines = top depths of labeled cores.

step (with disturbed fabrics indicated with an X in Figure **F27**). We observe an interval of normal polarity (Polarity Zone N1 in Figure **F27**) from the surface to 193.8 m CSF-A in Hole U1603B. Fully reversed inclinations (less than −45°) are achieved by 194.08 m CSF-A, and we pick the boundary at 194 m CSF-A (Table **T11**).
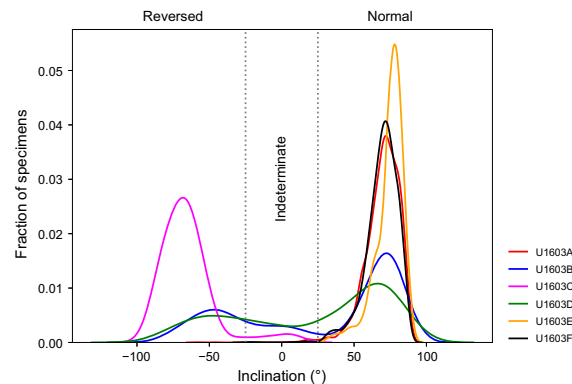
Figure F26. Kernel density plots of inclination data, Site U1603. Measurements were made on archive section halves after AF demagnetization to 20 mT. Two clearly distinguishable modes for the steeply down and steeply up directions support the interpretation of polarity.
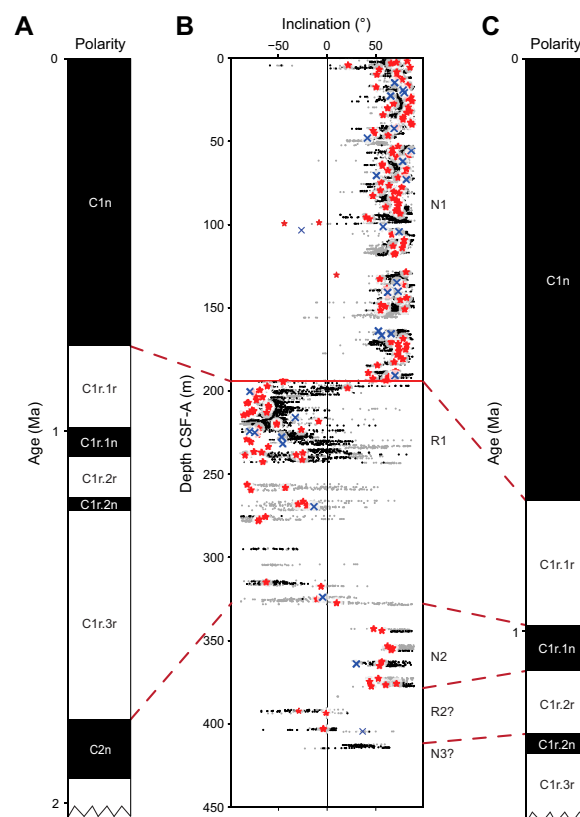
Figure F27. Magnetostratigraphic correlation with the GPTS of Ogg (2020), Site U1603. A. Low sedimentation rate scenario in which the transitional inclinations from about 220 to 260 m CSF-A (unlabeled) are interpreted as the Jaramillo Subchron (C1r.1n; 0.990–1.070 Ma) and the lower normal interval (Polarity Zone N2) as the Olduvai Subchron (C2n; ended 1.775 Ma). B. Inclinations (archive section half data: gray dots = unfiltered, black dots = filtered; discrete specimens: red stars = undisturbed, blue Xs = disturbed). N1–N3 = normal polarity zones. R1–R2 = reversed polarity zones. Polarity Zone N1 is interpreted as the Brunhes Chron (C1n). Two different interpretations of the remaining polarity zones are shown in A and C. C. High sedimentation rate scenario in which normal Polarity Zone N2 (between about 327–393 m CSF-A) is interpreted as the Jaramillo Subchron (C1r.1n; 0.990–1.070 Ma) and Polarity Zone N3 as the Cobb Mountain Subchron (C1r.2n; ended 1.180 Ma).

Table T11. Suggested Chron boundary depths, Site U1603. **Download table in CSV format.**

Hole	Polarity zone	Top age (Ma)	Top depth CSF-A (m)	Chron
U1603A	N1	0.000	0.00	C1n
U1603B	R1	0.773	194.00	C1r.1r
U1603D	N2	0.990	327.00	C1r.1n
U1603D	R2	1.070	393.00	C1r.2r
U1603D	N3	1.180	411.00	C1r.2n

In the lower part of Hole U1603B, starting at about 200 m CSF-A, we observe somewhat shallow inclinations in the pass-through archive section half measurements, but they are in intervals of interlaminated mud and sand, as well as dispersed clasts. Discrete specimens from these cores (red stars in Figure **F27**), chosen to avoid sandy intervals and clasts, show steeper negative inclinations consistent with a reversed polarity. It is also possible that this period may be associated with an excursion or coring disturbance, as indicated by the X symbols.

We define the transition in inclinations back to normal polarity in Section 400-U1603C-8R-3 at 327 m CSF-A (Polarity Zone N2 in Figure **F27**). Recovery was poor in Hole U1603D, but the normal polarity interval appears to continue through at least Core 13R. We define the lower boundary of Polarity Zone N2 at 393 m CSF-A in Hole U1603D, with a potential interval of reversed polarity (Polarity Zone R2) below. A third normal interval (Polarity Zone N3) may appear briefly at 411 m CSF-A in Hole U1603D (Figure **F27**).

We identified two possible scenarios for correlating the magnetostratigraphic patterns measured below the Brunhes Chron to the chrons defined in the geomagnetic polarity timescale (GPTS) of Ogg (2020). The first scenario (Figure **F27A**) correlates the interval of intermediate directions within Polarity Zone R1 with the Jaramillo Subchron (C1r.1n) and Polarity Zone N2 with the Olduvai Subchron (C2n). The second (preferred; see **Age model**) scenario (Figure **F27C**) correlates Polarity Zone N2 with the Jaramillo Subchron (C1r.1n) and Polarity Zone N3 tentatively with the Cobb Mountain Subchron (C1r.2n) (Table **T11**).

6. Physical properties

Physical property data were acquired on all cores from Holes U1603A−U1603D using the Whole-Round Multisensor Logger (WRMSL) for wet bulk density from gamma ray attenuation (GRA), MS, and *P*-wave velocity (using the *P*-wave logger [PWL]) at a 2 cm resolution. We also measured NGR in all sections longer than 50 cm. Thermal conductivity was measured in one whole-round section per core wherever possible. It was measured on the working section halves if the sediment was too hard or the whole-round measurement readings were unreliable. For Holes U1603E and U1603F, only NGR and low-resolution (5 cm) MS were logged for stratigraphic correlation purposes. The cores from these sites were sampled for sedaDNA; thus, the GRA source was kept inactive during WRMSL logging to avoid possible effects on the DNA preservation. Equalization to room temperature was not reached because of the fast track logging for stratigraphic correlation purposes. Thus, PWL measurements were not made.

After the whole rounds were split into halves, we acquired X-ray imaging of the archive halves of every core. The Section Half Multisensor Logger (SHMSL) was used to measure point MS (MSP) and color reflectance using the L*a*b* color system, and the red-green-blue color space (RGB) of the sediments was captured with the Section Half Imaging Logger (SHIL). In addition, we determined *P*-wave velocities at discrete points on the working section halves for almost all cores at Site U1603. In general, we measured *P*-wave velocity in three sections per APC core and two sections per HLAPC and rotary core barrel (RCB) core. *P*-wave caliper (PWC) measurements of *P*-wave velocity were done in all sections from Holes U1603E and U1603F to compensate for the lack of PWL measurements. Measurements were taken at variable intervals to accommodate lithologic variations. Two moisture and density (MAD) samples per core were taken and processed for Holes

U1603A–U1603D to obtain discrete wet bulk density, dry bulk density, grain density, and porosity. No MAD samples were taken for Holes U1603E and U1603F.

Prominent variations in physical property values occur at similar depths in NGR, density, and MS signals and are associated with major lithologic changes in the cores. More uniform lithologies are reflected by more monotonous physical property signals. The sensors worked correctly, and the data are of good quality. Accordingly, the physical properties obtained from Site U1603 provide valid and reproducible information on sediment composition and its variability for all cores.

6.1. Physical property measurements and measurement intervals

High-resolution physical property measurements were made on all core sections and most core catchers from Holes U1603A–U1603D to provide basic information on sediment composition and variability. The WRMSL measured bulk density by GRA, MS, and compressional *P*-wave velocity on the PWL at 2 cm intervals. PWL measurements were not obtained on cores from Holes U1603E and U1603F because logging lacked the time for equilibration to room temperature (fast tracked for stratigraphic correlation) required to obtain reliable readings of compressional wave velocity. In general, PWL readings are robust on cores recovered with the APC system, but material recovered with the RCB system has a slightly smaller core diameter and does not fill the liner entirely. The lack of proper contact between the caliper and the sediment leads to large standard deviations in the measurements. Thus, PWL values are only of use in correlation with PWC velocities. GRA measurements were not made on cores from Holes U1603E and U1603F because they were sampled for sedaDNA. For these cores, only MS was measured on the WRMSL at 5 cm resolution for correlation proposes. For holes with sedaDNA sampling, measurements of MS were made on the WRMSL in Special Task Multisensor Logger (STMSL) (fast track) mode and are noted as such in the Laboratory Information Management System (LIMS) database; however, for simplicity in this report, they are referred to as WRMSL measurements. NGR was measured with a counting period of 300 s at 10 cm intervals (see **Physical properties** in the Expedition 400 methods chapter [Knutz et al., 2025]) on all cores from Site U1603. Thermal conductivity was measured using the TK04 (Teka Bolin) system in the whole-round sections wherever possible. However, it was obtained with a puck probe from the working section halves where sediment was too hard to penetrate with the needle probe or if the readings were not accurate. Needle and puck probes provide comparable data.

After the cores were split, the section halves were X-rayed and thermal conductivity was measured, unless this could be performed on the whole-round section. PWC velocity was acquired in three working sections per core for Holes U1603A–U1603D and all the working sections from Holes U1603E and U1603F. Lithology and core disturbance prohibited the collection of PWC values on 2 cores out of 13 from Hole U1603A, 2 cores out of 26 from Hole U1603B, 3 cores out of 9 from Hole U1603C, 6 cores out of 17 from Hole U1603D, and 3 cores out of 7 from Hole U1603E. For Holes U1603C and U1603E, the cores missing PWC measurements are those with no recovery. MSP and color reflectance were measured at 2 cm increments using the SHMSL, and digital color imaging was measured with the SHIL on all archive section halves. Additionally, discrete samples from all cores from Holes U1603A–U1603D were taken for MAD measurements as two samples per core, ideally representing different lithologies. They were processed on board to determine water content, wet bulk density, dry bulk density, porosity, and grain density.

All physical property analyses were carried out except the PWC measurements mentioned above. Low-quality PWL measurements were noted on RCB cores in Holes U1603C and U1603D. Core disturbances, such as upbowing of layers, did not diminish the quality of the physical property data in a way that prevents meaningful core-seismic integration.

6.1.1. Whole-Round Multisensor Logger measurements

Results from WRMSL measurements for Holes U1603A–U1603D are compiled in Figure **F28**. We measured high-resolution data (2 cm intervals) for all the core sections and the majority of the core catchers. All cores from Holes U1603A–U1603D rested for around 5 h to equilibrate to room temperature (~19°C) before logging in the WRMSL. We measured NGR and low-resolution MS (5 cm intervals) for all cores from Holes U1603E and U1603F upon arrival to the laboratory for strati-

graphic correlation purposes (Figure **F29**). The logs described in this chapter have undergone preliminary processing including clipping, despiking, and smoothing. A positive correlation is found between density and NGR counts, as well as between density and MS downhole, likely in response to lithology changes at Site U1603 (Figures **F28**, **F29**, **F30**). The correlation between these physical properties distinguishes four physical properties units at Site U1603; the main signatures of those units are summarized in Table **T12**.

6.1.1.1. Gamma ray attenuation bulk density

Wet bulk densities range 1.3–2.1 g/cm^3 with a mean value of 1.9 g/cm^3. Wrapping cyclicity is observed downhole for GRA bulk density, along with a downhole trend to increasing values above Core 400-U1603B-10F (~165 m CSF-A), whereas below this depth, GRA baseline values show a slight decrease with depth. The lowest values are found in Cores 2H (~120 m CSF-A), 9F (~160 m CSF-A), and 400-U1603D-6R (305 m CSF-A), and the highest values are located between 130 and 180 m CSF-A (Figure **F28**). GRA bulk density values generally agree with calculated densities from the MAD discrete samples, except in the interval between 35 and 155 m CSF-A, where MAD values are consistently lower than GRA density values. The largest differences are up to 0.2 g/cm^3.

6.1.1.2. Magnetic susceptibility

MS is sensitive to the concentration and type of magnetic minerals deposited in the sediments. Although it usually appears as sharp peaks of high-amplitude variability, MS also tracks lithologic
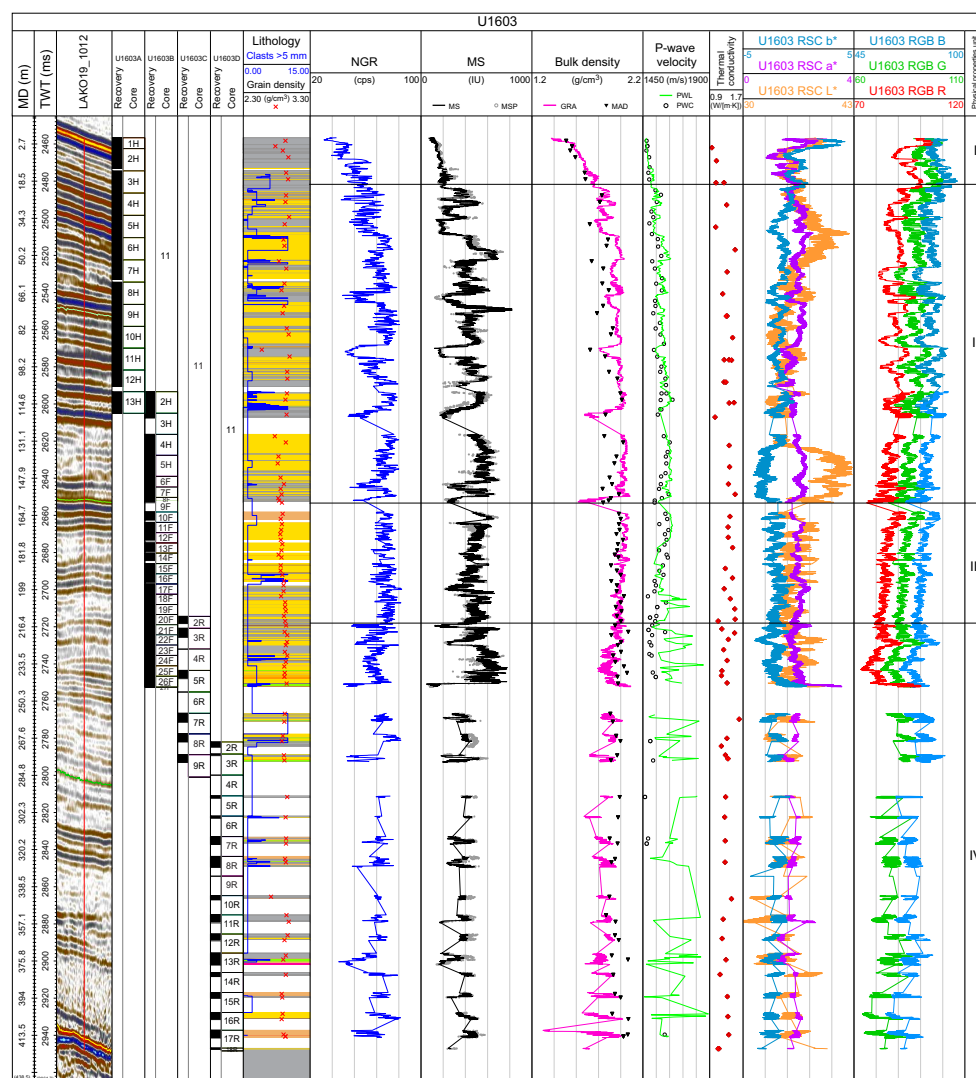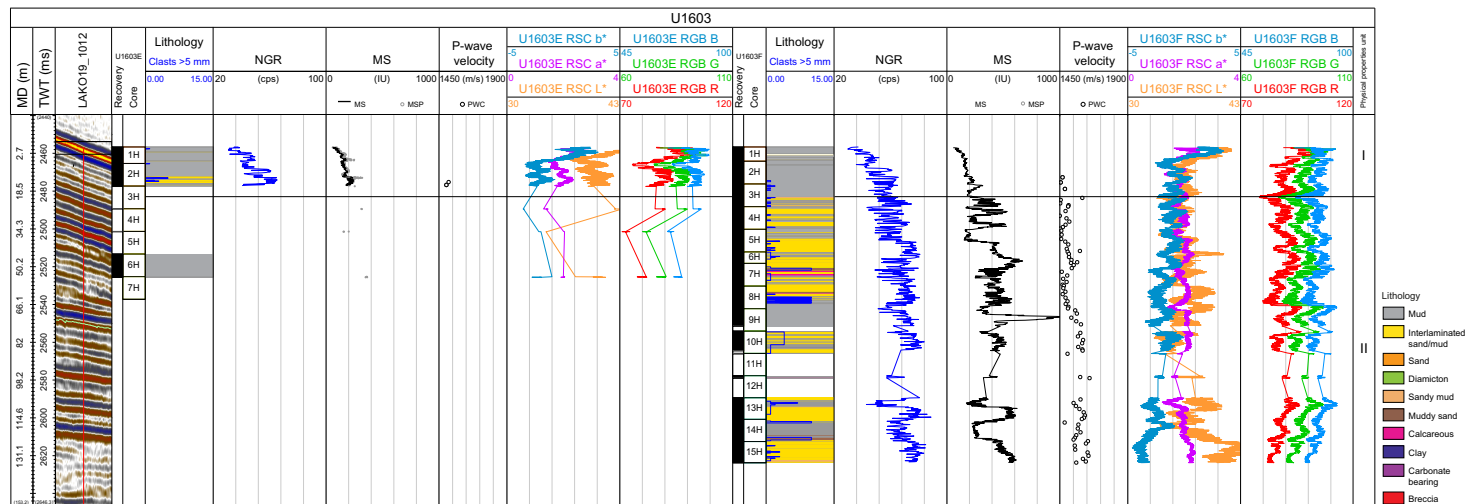

Figure F28. Physical properties, Holes U1603A–U1603D. MD = measured depth (m CSF, Method B [CSF-B]). TWT = two-way traveltime. cps = counts per second. RSC = reflectance spectroscopy and colorimetry.

changes. Values at Site U1603 range 49×10^{-5} to 821×10^{-5} SI with a mean of 391×10^{-5} SI (Figures **F28**, **F29**). The baseline of the signal presents high-amplitude variability (up to 230×10^{-5} SI), particularly between 20 and 165 m CSF-A. There is a general decrease in the baseline of MS downhole.

The highest MS values are found in Core 400-U1603A-9H ($>800 \times 10^{-5}$ SI), and the lowest values are observed in Cores 1H–3H and 400-U1603B-26F ($\sim80 \times 10^{-5}$ SI). Generally, we observe a strong correlation in the variability with depth of all physical properties determined with the WRMSL (Figure **F29**). However, MS varies considerably within intervals of high NGR and GRA bulk density (Figure **F28**).

6.1.1.3. *P*-wave velocity using the *P*-wave logger

P-wave velocities measured with the PWL show unreliable values on sections with cracks or poor contact between the sediment and the liner. Thus, measurements on cores recovered with the APC or HLAPC systems are more reliable than those drilled with the XCB or RCB systems. However, the measurements are generally good and range 1470–1900 m/s. PWL values gradually increase downhole, exceeding 1800 m/s below 230 m CSF-A (Figure **F28**). The lowest velocity values are observed for Cores 400-U1603A-1H and 2H (above 5 m CSF-A) and the highest for Core 400-U1603B-24F downward (below 230 m CSF-A).

Figure F29. Physical properties, Holes U1603E and U1603F. MD = measured depth (m CSF-B). TWT = two-way traveltime. cps = counts per second. RSC = reflectance spectroscopy and colorimetry.
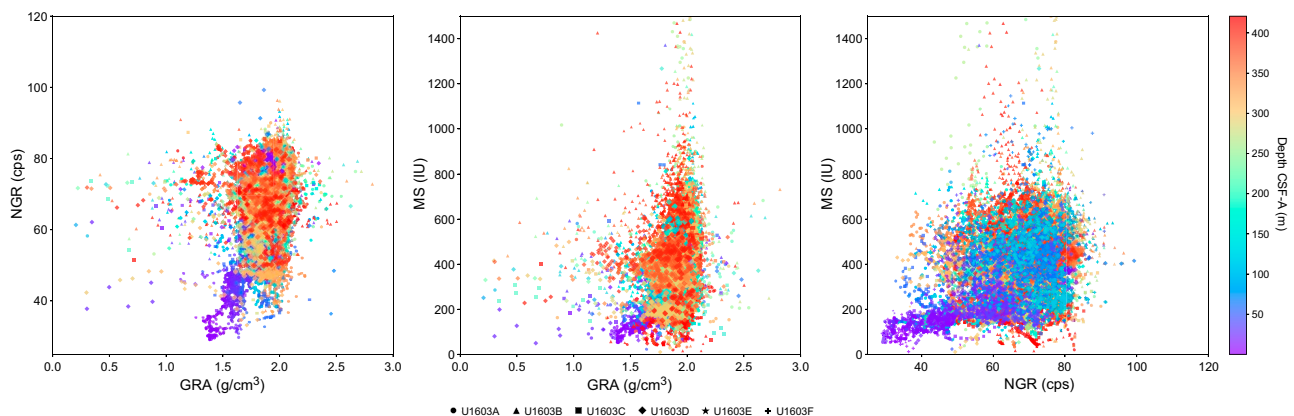
Figure F30. Crossplots and linear relationships of NGR, GRA bulk density, and MS, Site U1603. cps = counts per second.

6.1.2. Natural gamma radiation

NGR values display high-amplitude variability with cyclic changes at Site U1603 (Figures **F28**, **F29**). NGR values oscillate between 30 and 86 counts/s with a mean of 68 counts/s. The baseline of the signal responds to high NGR values between Cores 400-U1603A-6H and 400-U1603B-21F (40–220 m CSF-A). In this interval, the lowest counts in NGR are for Cores 400-U1603A-8H, 11H, 400-U1603B-3H, and 9F. The NGR baseline is lower in cores from Holes U1603C and U1603D (220–422 m CSF-A).

6.1.3. Thermal conductivity

Thermal conductivity varies between 0.9 and 1.7 W/(m·K) at Site U1603 (Figure **F28**). There is a clear positive trend with depth through Core 400-U1603B-21F (~220 m CSF-A; mean = 1.4–1.6 W/[m·K]). Below this depth, thermal conductivity values decrease to an average of 1.3 W/(m·K), which remains constant to the base of the hole, where the deepest measured value is 1.1 W/(m·K). The lowest values were measured in Cores 400-U1603A-5H and 400-U1603B-3H (38–120 m CSF-A), and the highest values are observed in Cores 400-U1603A-6H (48 m CSF-A), 400-U1603B-19F (208 m CSF-A), 20F (210 m CSF-A), and 400-U1603D-18R (421 m CSF-A). The observed thermal conductivity does not present clear dependence on sediment facies.

6.1.4. Point magnetic susceptibility

MSP measurements show a good match to values obtained from the WRMSL (Figures **F28**, **F29**). However, higher variability is observed with this instrument because of the smaller integration volume of the sensor (~1 cm; 1σ) compared to the loop (~18 cm; 1σ) used for the WRMSL (Weber et al., 1997).

Table T12. Physical properties units, Site U1603. **Download table in CSV format.**

Unit	Top hole, core	Top depth CSF-A (m)	Bottom hole, core	Bottom depth CSF-A (m)	Physical properties	Lithology	Seismic facies
I	400-U1603A-1H, U1603E-1H, U1603F-1H	0	400-U1603A-3H, U1603E-3H, U1603F-3H	20	NGR, MS, GRA, *P*-wave, and thermal conductivity generally increase downhole in this unit.	The increase in physical properties values might be related to a downhole decrease in water content and a transition from a lithology dominated by mud at the top of the unit to interlaminated mud with thin sandy levels toward the bottom of the unit.	Low-amplitude and low lateral continuity reflections are identified in this interval. At this site, concordant terminations are observed with top and bottom boundaries.
II	U1603A-3H, U1603E-3H, U1603F-3H	20	U1603B-9F	160	NGR, MS, and GRA show high-amplitude variability in this unit. Intervals of low values for these physical properties are identified. *P*-wave and thermal conductivity values generally increase downhole.	The variability of the physical properties in this unit reflects broad variations in the lithology. Intervals of low NGR, MS, and GRA values correlate with mud-dominant lithologic facies, and intervals with average to high values for the mentioned properties correlate with intervals of interbedded mud with abundant sand layers.	High-amplitude reflections of high lateral continuity are identified in the upper and lower parts of the unit. An interval of low-amplitude and medium lateral continuity reflections forms the central part of the unit. At this site, concordant terminations are observed with top and bottom boundaries.
III	U1603B-10F	160	U1603B-20F, U1603C-2R	215	NGR and GRA have a relatively constant baseline in this unit, whereas MS shows medium variability. The NGR baseline is relatively constant with depth, whereas MS and GRA slightly decrease downhole. Discrepancies between PWC and PWL become more relevant toward the lower part of the unit. PWC generally decreases downhole, and PWL increases downhole, showing peaks at the bottom of the unit. Thermal conductivity is relatively homogeneous within this unit.	The relative low variability of the physical properties is related to an interval where sand is the predominant lithology. Minimum MS values correlate to interbedded thin layers of mud.	Low- to medium-amplitude reflections form this unit. They present low lateral continuity at the top and bottom of the unit and high lateral continuity in the middle part of the unit. At this site, concordant terminations are observed with top and bottom boundaries.
IV	U1603B-20F, U1603C-2R	215	U1603D-18R	422	High-amplitude variability is observed in NGR, MS, GRA, and PWL in this unit. The baseline of these properties is relatively constant downhole; however, GRA and NGR values decrease downhole. PWC and PWL values largely differ in this unit. Thermal conductivity values decrease downhole.	The variability shown by the physical properties is related to a downhole transition from diamictons and interlaminated sand and mud layers to predominantly mud and sandy mud layers interbedded with diamicton.	The seismic facies in this unit show interbedded packages of high-amplitude and lateral continuous reflections with low-amplitude and lateral continuity reflections that become chaotic toward the bottom of the unit.

6.1.5. Color reflectance

L*a*b* color reflectance measurements describe coordinates in a spherical system with 16.8 million possible variations (Weber, 1998; Blum, 1997). The L* axis measures the black–white color component, known as lightness or gray value. It is a reliable tracer for the content of biogenic carbonate in marine sediment (Weber, 1998). The L* baseline is relatively constant at Site U1603; however, three intervals of increasing L* values are observed between Cores 400-U1603A-5H and 8H (33–55 m CSF-A), between Cores 400-U1603B-4H and 9F (135–160 m CSF-A), and in Core 400-U1603D-14R (~380 m CSF-A) (Figure **F29**).

The a* axis is the green–red component and is usually a tracer of changing redox conditions in the sediments or distinct provenance. At Site U1603, a* values oscillate between 1.0 and 2.2 and show a slight increasing trend downhole. A peak in a* values is observed at the base of Hole U1603B (>3.1). The b* axis is the yellow–blue component, with more positive values (yellower colors) corresponding to higher opal (usually diatoms) contents. At Site U1603, b* values are low (−3 to 3) and show a slight decreasing trend downward. The lowest b* values match the intervals of highest L* (Figure **F29**).

6.1.6. Gantry

Results of section-half gantry measurements for Holes U1603A−U1603D are compiled in Figure **F31**. Correlation between GRA and MAD density and PWC and PWL values confirms the high quality of the data (Figure **F28**).

6.1.6.1. *P*-wave velocity using the *P*-wave caliper

Discrete *P*-wave measurements were carried out using the PWC (see **Physical properties** in the Expedition 400 methods chapter [Knutz et al., 2025]). Measurement resolution within each core varied depending on lithology, recovery, and quality, with at least three measurements per core. The PWC measurements provide a correlation for PWL values measured on the whole-round cores with the WRMSL (Figure **F28**). PWC measurements were made in every core from Site U1603; however, unreliable or no results were obtained on several cores.

PWC values ranging ~1400 to ~1630 m/s (Figures **F28**, **F31**) obtained for Holes U1603A and U1603B are consistent with the trends observed in the PWL values from the WRMSL to ~200 m CSF-A (Figure **F28**). Very low PWC values for Holes U1603C and U1603D might be a result of core expansion upon arrival in the laboratory.

6.1.6.2. Shear strength

A number of discrete shear strength measurements were conducted using the automated vane shear (AVS) tool (see **Physical properties** in the Expedition 400 methods chapter [Knutz et al., 2025]). Five shear strength measurements were obtained on the deepest cores from Hole U1603B (24F through 26F) (Figure **F31**). Shear strength values for Hole U1603B range 25–58 kN/m^2.

6.1.6.3. Moisture and density

Sediment samples were taken from the working halves of split cores for measuring MAD on all cores from Holes U1603A−U1603D. No MAD samples were taken on cores from Holes U1603E and U1603F. Bulk density values were calculated from moisture and volume measurements (see **Physical properties** in the Expedition 400 methods chapter [Knutz et al., 2025]). Sample resolution within each core varied depending on lithology, recovery, and quality, with at least two samples per core. MAD samples were taken adjacent to the PWC measurement so that a correlation between *P*-wave velocity and bulk density can be made. A total of 107 samples were taken for MAD estimates: 24 from Hole U1603A, 48 from Hole U1603B, 12 from Hole U1603C, and 23 from Hole U1603D.

MAD density values correlate in general with GRA bulk density measured on the WRMSL (Figure **F28**). However, MAD density values are slightly lower than GRA bulk density for Holes U1603A and U1603B but slightly higher compared to GRA values for Holes U1603C and U1603D. Bulk density values for Site U1603 range 1.2–2.3 g/cm^3 with a mean of 1.9 g/cm^3 and exhibit an overall downhole increase. Trends observed at Site U1603 (Figures **F28**, **F31**) for grain density measurements closely follow those observed for bulk density. This likely reflects the grain density of the

major lithologic components at this site: quartz (2.65 g/cm^3), biotite (~3 g/cm^3), dolomite (2.84 g/cm^3), common clays, and feldspars (~2.56 g/cm^3).

Porosity represents the percent of pore space of wet sediment volume and generally decreases downhole as the sediments compact (Figure **F31**). Discrete porosity values range from ~71% near the top of Site U1603 to 38% below 405 m CSF-A. Average porosity at Site U1603 is 48%.

6.2. Core-log-seismic correlation

The seismic facies of the units defined by physical properties are described in Table **T12**. General changes in seismic facies in the seismic profile correspond to changes in the physical properties. Correlation of the seismic signal in two-way traveltime with depth in meters has been achieved through the construction of distinct velocity models. Four velocity models were generated for Site U1603 considering *P*-wave velocities measured in the laboratory (i.e., PWC and PWL), *P*-wave velocity from the Dipole Sonic Imager (DSI) (see **Downhole measurements** in the Expedition 400 methods chapter [Knutz et al., 2025]), and time-depth relations from the VSI experiment. The
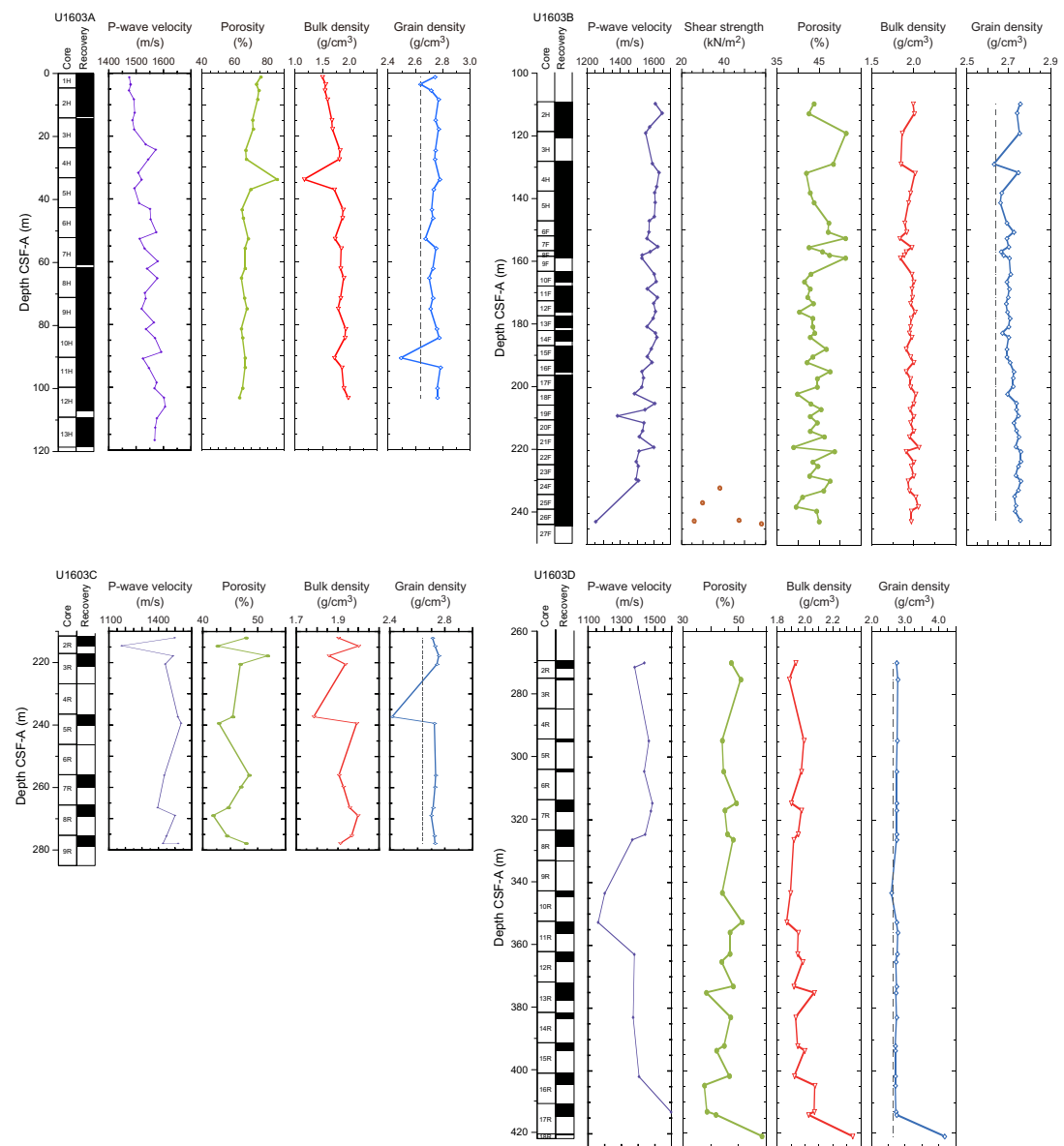
Figure F31. Results from gantry and MAD analyses, Holes U1603A–U1604D. PWC includes automatic and manually picked first arrival times. Grain density: dashed line = quartz reference value of 2.65 g/cm^3.

time-depth correlation based on the laboratory *P*-wave measurements (PWC and PWL) results in an overextended seismic profile because of the low velocity values, which are probably related to core expansion upon resting in the laboratory. The VSI check shots usually provide the most robust time-depth constraints. However, at Site U1603, the stations were concentrated on the lower part of the hole, with the uppermost part lacking data constraints. In addition, poor anchoring of the geophones resulted in noisy data that needs further detailed processing. Because of time constraints during the expedition, the processing was not implemented on board. Thus, the core-log-seismic correlation for Site U1603 was based on the velocity model from the DSI velocities obtained during downhole logging in Hole U1603D. The final fits between the seismic facies, preliminary observations on the FMS log, and the lithologic variability confirm a feasible time-depth relationship. The resulting time-depth relationship has been applied in Figures **F28** and **F29**.

7. Geochemistry

Samples for headspace gas, interstitial water (IW) chemistry, and bulk sediment geochemistry were analyzed at Site U1603. Headspace hydrocarbon gas measurements showed low concentrations in the uppermost 150 m and higher concentrations of methane, with a low yet consistent presence of ethane, in sediment units below 150 m CSF-A. The main findings from IW analysis include decreases in lithium and potassium with depth, possibly indicating clay formation. A monotonic decrease in sulfate with depth to a minimum around 150 m CSF-A provides evidence for a sulfate–methane transition zone. IW iron, manganese, and phosphate show high concentrations near the sediment surface and sharp decreases to low concentrations with increasing depth. Increases in IW calcium and alkalinity in the upper depths may indicate dissolution of calcium carbonate ($CaCO_3$) minerals. Elemental analysis of solid sediment samples revealed overall low concentrations of carbon and nitrogen across most intervals, albeit individual layers were rich in $CaCO_3$ with contents up to 60%.

7.1. Volatile hydrocarbons

As part of routine environmental protection and safety monitoring, headspace hydrocarbons were analyzed for Holes U1603A–U1603D (Figure **F32**). Samples for headspace gas analysis were taken at a resolution of one sample per core (9.6 m advance). For cores below 200 m CSF-A (Holes U1603C and U1603D), every other half-length core (4.8 m advance) was sampled whenever recovery exceeded 50%. A total of 129 samples were analyzed for headspace gases. Methane (CH_4) concentrations were generally low (1.8–19 ppm) in the uppermost 170 m but promptly increased to
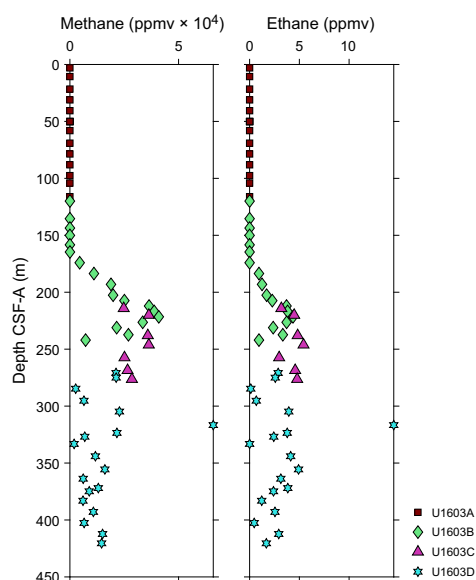
Figure F32. Hydrocarbon gas concentrations, Holes U1603A–U1603D. Samples were taken from 5 cm³ of sediment.

concentrations of 1,900–66,000 ppm at depth (Holes U1603B–U1603D). Ethane (C_2H_6) concentrations were below detection limit above 180 m CSF-A and were 0.12–14 ppm across headspace samples below 180 m CSF-A (Holes U1603B–U1603D).

7.2. Interstitial water chemistry

A total of 68 IW samples were squeezed from 5 or 10 cm whole-round samples. Typically, samples yielded 30 cm³ of water for subsequent analysis. Samples from poorly lithified horizons and intervals with high contents of dropstones often resulted in lower yields because much of the material had to be discarded to avoid possible contamination of drill mud. Two additional samples were collected and analyzed, one from the mudline (sediment surface) of Hole U1603A and one from overlying water at Hole U1603D. Additional high-resolution (approximately one per meter) Rhizon water samples were taken from Hole U1603E in the uppermost 15 m.

7.2.1. pH and alkalinity

The measured pH values range 7.56–8.06 (Figure **F33**). The mudline sample from Hole U1603A has a pH of 7.67, and pH generally increases over the uppermost 40 m to 7.8. The pH notably increases to ~7.9 in the interval 160–220 m CSF-A. Values below this interval range 7.79–7.99 with no discernible trends. Alkalinity values increase from 2.3 mM at the sediment/water interface to a maximum of 6.6 mM at 15.65 m CSF-A (Figure **F33**). Values decrease near-linearly downcore to a minimum of 1.4 mM at the bottom of Hole U1603D. The principal exception to this downhole trend is an abrupt increase in alkalinity from 2.6 mM at 150.05 m CSF-A to 3.8 mM at 164.64 m CSF-A.

7.2.2. Salinity, sodium, chloride, lithium, potassium, and bromide

IW salinity decreases downcore from values matching the mudline water salinity of 35 to a minimum of 31 at 200 m CSF-A (Figure **F34**). Salinity below 220 m CSF-A is consistently 32. No consistent trend is observed in the sodium and chloride values (Figure **F34**). Unlike what might be expected from the alkalinity data, sodium and chloride do not show a >10% decrease in concentration. Lithium and potassium decrease downcore from peak values of 22 µM and 12 mM. Lithium decreases over the uppermost 20 m, whereas potassium decreases over the uppermost ~200 m,
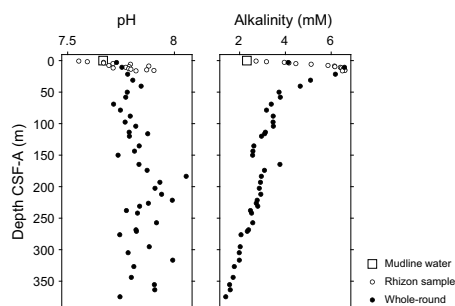
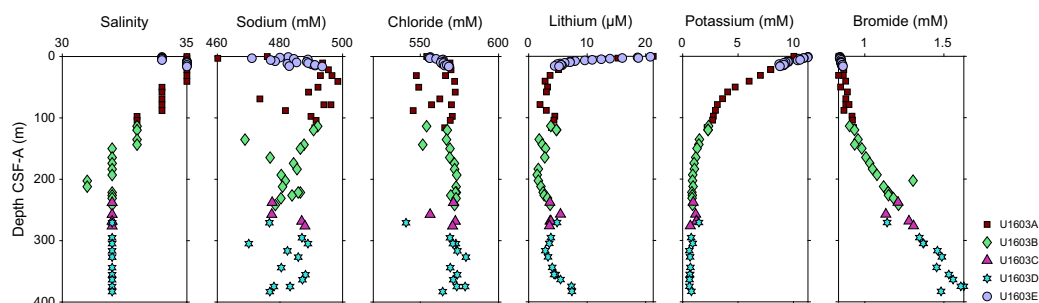**Figure F33.** IW pH and alkalinity, Site U1603.

Figure F34. IW salinity, sodium, chloride, lithium, potassium, and bromide, Holes U1603A–U1603E.

possibly indicating silicate alteration and clay formation throughout the core. Bromide increases roughly monotonically downcore from a mudline value of 0.8 mM to a peak value of 1.7 mM. Several samples between 200 and 300 m CSF-A deviated from the general trend, and the deepest samples are more scattered.

7.2.3. Ammonium, manganese, iron, sulfate, phosphate, and boron

Ammonium increases from trace levels near the detection limit of 10 µM in the mudline water to 500 µM in the uppermost 15 m of Site U1603, reaching a maximum of 624 µM at 100 m CSF-A and decreasing slightly downcore to approximately 400 µM (Figure **F35**).

Dissolved manganese increases from trace quantities at the sediment/water interface to a maximum of 78.6 µM at 3.75 m CSF-A (Figure **F35**). Concentrations decrease from 3.75 m to approximately 100 m CSF-A, whereas concentrations downcore remain roughly constant between 5 and 15 µM.

Iron increases in concentration in the IW from trace concentrations at the sediment/water interface to a maximum of 58.9 µM at 6.65 m CSF-A (Figure **F35**). Below 20 m CSF-A, the concentration of dissolved iron remains consistently between 0 and 12 µm.

Sulfate concentrations decrease over the uppermost 160 m from seawater concentrations of 28 mM to ~1 mM (Figure **F35**). Water extracted below this depth has consistently low concentrations of sulfate, typically <2 mM, with no sample exceeding 6 mM. Phosphate concentrations increase from a seawater concentration of 8.5 µM to a maximum of 51.7 µM at 7.65 m CSF-A (Figure **F35**). These values decrease back to roughly seawater values within the uppermost 50 m and remain consistent downcore.

Boron increases from a seawater concentration of 408.2 µM at the mudline to a maximum value of 572.5 µM at 14.65 m CSF-A (Figure **F35**). Below this peak value, values decrease to 200 m CSF-A, below which concentrations remain largely unchanged.

7.2.4. Calcium, magnesium, strontium, silicon, and barium

Calcium concentrations (IW) increase in the uppermost core from a seawater value of 10.2 mM at the mudline to 13.48 mM at 13.65 m CSF-A (Figure **F36**). This ~3 mM increase in calcium concentration correlates with the 4 mM increase in alkalinity (Figure **F33**), likely reflecting the dissolution of a calcium carbonate mineral. Below, calcium concentrations reach a local plateau to 135 m CSF-A before concentrations drop from 14.7 to 11.3 mM at 183.55 m CSF-A. This inflection coincides with the interface between sulfate- and methane-bearing fluid. Below this depth, calcium concentrations increase to a maximum value of 25.8 mM at 374.73 m CSF-A.

Magnesium concentrations decrease consistently from a seawater concentration of 53.1 mM at the mudline to a minimum value of 17.5 mM at 374.73 m CSF-A (Figure **F36**).

Strontium increases sharply in the upper sediment from a minimum concentration of 84.6 µM at 2.75 m CSF-A to a concentration of 100.9 µM at 69.05 m CSF-A (Figure **F36**). Strontium concen-
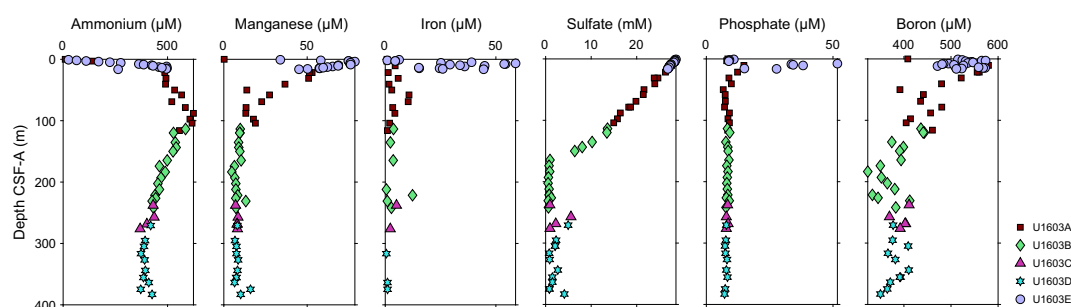
Figure F35. IW ammonium, manganese, iron, sulfate, phosphate, and boron, Holes U1603A–U1603E.

trations remain largely consistent downcore to 257.60 m CSF-A; below this depth, concentrations increase from 106.6 µM to a maximum value of 146.8 µM at 374.73 m CSF-A.

Dissolved silicon concentrations increase from a minimum value of 93.7 µM at the mudline and average 173 µM ± 45 µM (1σ) downcore with no discernible trends (Figure **F36**).

Dissolved barium concentrations increase from a minimum of 0.5 µM at the mudline to 1.1 at 150.05 m CSF-A (Figure **F36**). Below this depth, concentrations are consistently higher and more variable, reaching ~3 µM around 250 m CSF-A. Barium concentrations continue to generally increase downcore and reach a maximum of 4.8 µM at the bottom sample at 383 m CSF-A. Notably, the increase in barium concentrations coincides with the depletion of dissolved sulfate at ~150 m CSF-A.

7.3. Bulk sediment geochemistry

7.3.1. Carbon, nitrogen, and carbonate

The shipboard solid phase analysis at Site U1603 from all major lithostratigraphic units identified consisted of measurements of $CaCO_3$, total carbon (TC), and total nitrogen (TN) using shipboard plastic cylinder sampling (sample type CARB). CARB samples were taken from Holes U1603A–U1603D at a resolution of 2 samples per core (9.6 m advance); a total of 69 samples were taken. Duplicate analyses were performed on six samples to verify the accuracy of the analysis. Total organic carbon (TOC) was calculated from measurements of $CaCO_3$ and TC. Downcore profiles of $CaCO_3$, TOC, and TN contents (weight percent) at Site U1603 are shown in Figure **F37**.
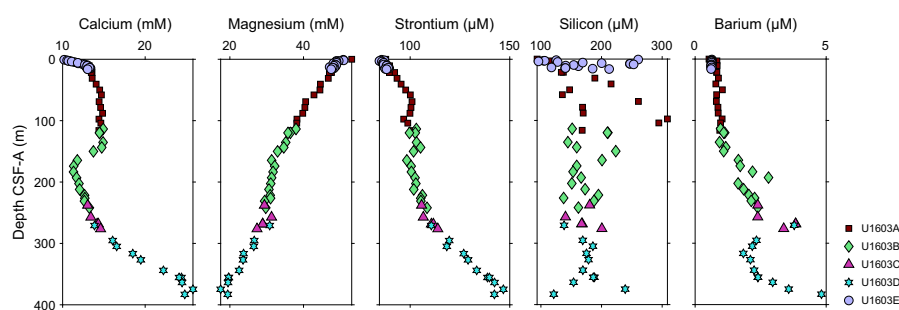
Figure F36. IW calcium, magnesium, strontium, silicon, and barium, Holes U1603A–U1603E.
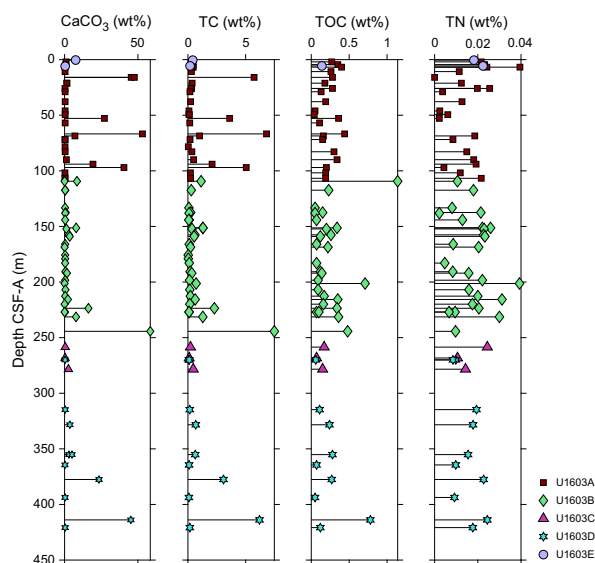
**Figure F37.** $CaCO_3$, TC, TOC, and TN, Holes U1603A–U1603E.

Although the CaCO$_3$ content is below 1% throughout most intervals, CaCO$_3$ concentrations are as high as 58% in selected calcareous mud intervals. The TOC content ranges 0.1%–0.8% throughout Holes U1603A–U1603D, and most samples have values less than 0.4%. The TN content is <0.04% throughout all samples analyzed.

8. Stratigraphic correlation

To minimize coring gap alignment, sequences from Holes U1603A–U1603D were examined using whole-round MS measured at a 2 cm resolution with the WRMSL and NGR data at 10 cm intervals. In addition, 5 cm resolution MS and NGR data were measured on all sections from Holes U1603E and U1603F and examined in near–real time to ensure adequate coring depths to fill the gaps in Hole U1603A. Because triple APC offset coring was abandoned in favor of reaching the total depth at Site U1603, the splice could only provide partial stratigraphic coverage. The difficulty was further magnified by low recovery rates below 105 m CSF-A. Thus, Holes U1603A–U1603D were correlated to each other, but they were mostly aligned by the top of the hole (seafloor). Holes U1603E and U1603F were correlated to Hole U1603A, completing a splice of the uppermost 98 m.

The top of Hole U1603A (which preserved a mudline) served as the anchor (zero depth point) for generation of the core composite depth below seafloor, Method A (CCSF-A), depth scale at this site (see **Stratigraphic correlation** in the Expedition 400 methods chapter [Knutz et al., 2025] for an explanation of depth scales). We attempted to determine the relative depth offset of each core from this reference by establishing affine ties between cores from all six holes based on optimized correlation of WRMSL-derived MS and NGR data (see Figure **F22** in the Expedition 400 methods chapter [Knutz et al., 2025]). These depth offsets are illustrated in Figure **F38**, and the affine ties are reported in Table **T13**. Cores 400-U1603A-2H through 8H are tied, as well as Cores 400-U1603E-1H and 2H and Cores 400-U1603F-1H through 8H. Below these cores, a tie has been achieved between Cores 400-U1603A-8H and 400-U1603F-9H after correlation with paleomagnetic data, and continuous ties between Cores 400-U1603A-9H, 400-U1603F-9H, 400-U1603A-10H, and 400-U1603F-10H provide a continuous splice to 98.9 m CCSF, Method D (CCSF-D). Further ties between Cores 400-U1603A-12H, 400-U1603F-13H, 400-U1603B-2H, 400-U1603F-
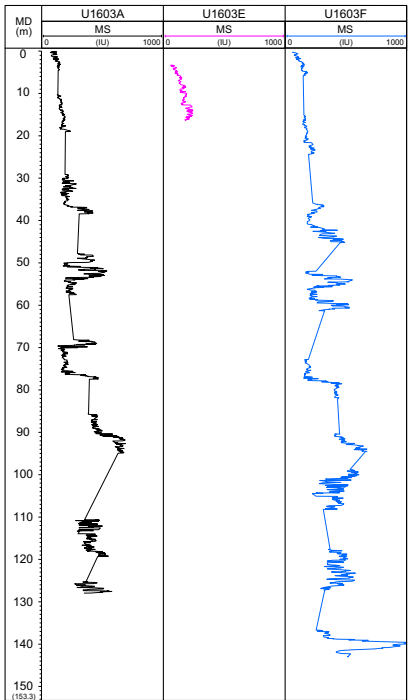
Figure F38. WRMSL-derived MS data, Holes U1603A, U1603E, and U1603F. MD = measured depth (m CCSF-A).

13H, and 400-U1603F-14H and Cores 400-U1603F-15H and 400-U1603B-4H are possible. The RCB recovery and drilling deformation found in the cores limit the correlation with Holes U1603C and U1603D. Core disturbances, shattered core liners, and other issues impacting core quality mean that the stratigraphic coherence of the sedimentary sequence recovered is variable. Ties have been made between Cores 400-U1603B-21F and 400-U1603C-2R and Cores 400-U1603B-26F and 400-U1603C-5R, with input from core descriptions, paleomagnetism, and high-resolution linescan camera and X-ray images as the only way to gain an offset estimate. Because the relevant core gaps are very close to being lined up between the two holes, the affine ties between these cores are uncertain (see the Quality comment column in Table **T13**).

In summary, it is not possible to build a complete CCSF-D depth scale for Site U1603. However, the high recovery and core alignment between Holes U1603A, U1603E, and U1603F allow for the construction of a pseudo-splice to 98.9 m CCSF-D (Table **T14**).

8.1. Construction of the pseudo-splice

After the composite depth scale was created, selected sequences from Holes U1603A, U1603E, and U1603F were spliced together to create the most complete and representative section possible (Figure **F39**). Detailed sedimentological logs and archive-half X-ray images were also taken into account during the process of splice construction to avoid inclusion of any significantly disturbed intervals and/or sections with unique features (relative to the other holes). However, it was necessary to include disturbed intervals at the top and bottom of some cores to achieve an overlapping section. Thus, we refer to the end product as a pseudo-splice (Table **T14**).

The primary pseudo-splice for Site U1603 spans 0–98.9 m CCSF-D. It is based predominantly on correlation of sediment MS and NGR data. The affine growth factor is 1.12 in Core 400-U1603F-10H and 1.11 in Core 400-U1603A-10H (i.e., the last tied cores in the pseudo-splice). Cores from Holes U1603F and U1603A extend to 83.6 and 90.0 m CSF-A, respectively. High uncertainty on the ties exists between Cores 400-U1603A-8H and 400-U1603F-9H at 77.8 m CCSF-D. Moreover, all the cores included in the pseudo-splice are APC cores, and although it is possible to correlate them to each other, the coring gaps are very close to aligned. Downhole logging data may potentially be used to improve the depth accuracy of these cores (see **Downhole logging**).

Below 98.9 m CCSF-A, multiple coring gaps of unknown length in Holes U1603A–U1603D prevent the extension of the pseudo-splice to the bottom of the site. At depths beyond the pseudo-splice, the described correlation between Holes U1603A–U1603D is not sufficient to warrant construction of a floating splice, and the gaps between cores are unknown.

8.2. Comparison of core and downhole logging data

Downhole logging was conducted in Hole U1603D (see **Downhole logging**) to establish connections to seismic data and provide additional data for cored (but possibly not recovered) intervals.

Table T13. Affine table, Site U1603. **Download table in CSV format.**

Table T14. Pseudo-splice table containing the core ties between Holes U1603A, U1603E, and U1603F. **Download table in CSV format.**
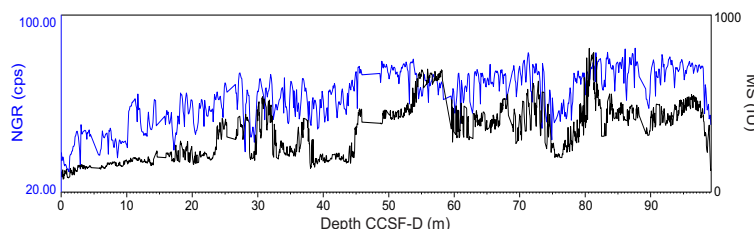
Figure F39. Pseudo-spliced record of MS and NGR, Site U1603. cps = counts per second.

Table T15. Affine table in correlation to downhole logging in Hole U1603D, Site U1603. **Download table in CSV format.**

The quality of the hole is generally good. Thus, the log provides a continuous record that may allow better interpretation of the lithologies encountered.

We imported the MS and total spectra gamma ray (HSGR) downhole logs into Correlator (v. 4) to improve our understanding of the positions of the cores, particularly below 98.9 m CCSF-A. We were able to upload downhole logs into Correlator by making a single core table with the log data. We attempted to tie each core from Holes U1603A and U1603F into the logging data, followed by cores from Holes U1603B–U1603D. This procedure has some significant uncertainties due to the presence of large-scale features in the downhole logging data that do not resemble the record measured on cores in the laboratory. However, the overall cyclicity is well matched between the logs and the cores, providing information that can be used to confidently improve the depth constraints onto the cores (Table **T15**).

9. Age model

The initial age model for Site U1603 is based on magnetostratigraphic interpretations for Holes U1603A–U1603D. The sediment from the seafloor to 194 m CSF-A in Hole U1603B is characterized by normal polarity (Polarity Zone N1 in Figure **F27**) and is interpreted as the Brunhes Chron (C1n, 0–0.773 Ma; Ogg, 2020). At 194 m CSF-A, there is a transition to reversed polarity (Polarity Zone R1), likely representing the Brunhes/Matuyama boundary (0.773 Ma). The normal polarity interval below 327 m CSF-A in Hole U1603D (Polarity Zone N2) is not well constrained due to gaps in recovery and drilling disturbance. However, we suggest correlation with the Jaramillo Subchron (C1r.1n, 0.990–1.070 Ma; Ogg, 2020). We suggest an uncertain lower boundary for Polarity Zone N2 at 393 m CSF-A, below which polarity is mainly reversed, with further divisions ambiguous.

To constrain the age of sediments beyond the interpretation of the polarity stratigraphy, we constructed an RPI time series. The magnetic remanence of the archive section halves after demagnetization in a peak AF of 20 mT (NRM_{20mT}), filtered as described in **Paleomagnetism**, was normalized by the point-source MS collected on the archive section halves. To create a more continuous time series, a filtered RPI data set was constructed using the composite depth scale for the site (meters CCSF-A), combining sections of Holes U1603A, U1603B, and U1603F to fill gaps in the recovery (Figure **F40**; Table **T16**).

With the chronostratigraphic tie point provided by the Brunhes/Matuyama boundary, we identify additional tie points using decreases in paleointensity (DIPs) and comparison with a model of the paleomagnetic axial dipole moment. The paleomagnetic axial dipole moment for the last 2 My (PADM2M; Ziegler et al., 2011) is a model constructed based on a stack of more than 80 globally distributed records calibrated to a consistent age model by Tauxe and Yamazaki (2007). Note that the age of the Brunhes/Matuyama boundary in the age model used by Tauxe and Yamazaki (2007) was 0.78 Ma, and individual records were calibrated using the stacked benthic $\delta^{18}O$ timescale (LR04) of Lisiecki and Raymo (2005). Comparison with PADM2M also provides the opportunity to predict where the marine isotopic stages of the LR04 $\delta^{18}O$ stack (Lisiecki and Raymo, 2005) may appear at Site U1603 (Figure **F41C**). We identified 10 tie points, including the reversal boundaries (Table **T17**), in our RPI record that are also recognizable in the PADM2M model. In addition to the DIP associated with the Brunhes/Matuyama boundary (C1r.1r (top)) and the tie points at the top and bottom of the Jaramillo Subchron (C1r.1n (top) and C1r.2r (top), respectively), we identified six DIPs between the seafloor and the Brunhes/Matuyama boundary and one between the Brunhes/Matuyama and the top of the Jaramillo Subchron (Figure **F41**).

Our paleomagnetic constraints allow us to create an age-depth model (Figure **F42**). We estimate average sediment accumulation rates (SARs) are ~28 cm/ky through the uppermost 250 m CCSF-A and ~75 cm/ky below 250 m CCSF-A to at least the beginning of the Jaramillo Subchron. This change in SAR at about 250 m CCSF-A coincides with the boundary between Lithostratigraphic
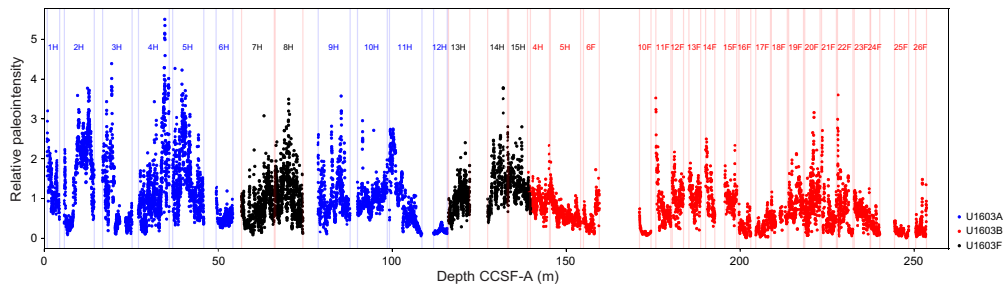
Figure F40. Construction of a composite series of RPI, Site U1603. Series uses data from Holes U1603A, U1603B, and U1603F and the core sections listed in Table T16. Depths are based on Table T13.

Table T16. Cores from Holes U1603A, U1603B, and U1603F used to construct the complete RPI dataset. **Download table in CSV format.**

Hole, core	Top depth CSF-A (m)	Top depth CCSF-A (m)	Hole, core	Top depth CSF-A (m)	Top depth CCSF-A (m)	Hole, core	Top depth CSF-A (m)	Top depth CCSF-A (m)
400-			U1603B-2H	109.1	117.119	U1603B-14F	182.1	189.846
U1603A-1H	0.0	0.000	U1603F-14H	115.3	124.312	U1603B-15F	186.9	194.646
U1603A-2H	4.6	5.673	U1603B-3H	118.6	126.839	U1603B-16F	191.6	199.346
U1603A-3H	14.1	15.805	U1603F-15H	124.8	133.013	U1603B-17F	196.4	204.146
U1603A-4H	23.6	26.568	U1603B-4H	128.1	135.846	U1603B-18F	201.1	208.846
U1603A-5H	33.1	36.392	U1603B-5H	137.6	145.346	U1603B-19F	205.9	213.646
U1603A-6H	42.6	48.816	U1603B-6F	147.1	154.846	U1603B-20F	210.6	218.346
U1603F-7H	48.8	56.591	U1603B-7F	151.9	159.646	U1603B-21F	215.4	223.146
U1603F-8H	58.3	66.233	U1603B-8F	156.6	164.346	U1603B-22F	220.1	227.846
U1603A-9H	71.1	78.622	U1603B-9F	158.4	166.146	U1603B-23F	224.9	232.646
U1603A-10H	80.6	89.229	U1603B-10F	163.2	170.946	U1603B-24F	229.6	237.346
U1603A-11H	90.1	99.092	U1603B-11F	167.9	175.646	U1603B-25F	234.4	243.830
U1603A-12H	99.6	108.765	U1603B-12F	172.6	180.346	U1603B-26F	239.1	249.863
U1603F-13H	105.8	113.044	U1603B-13F	177.4	185.146			
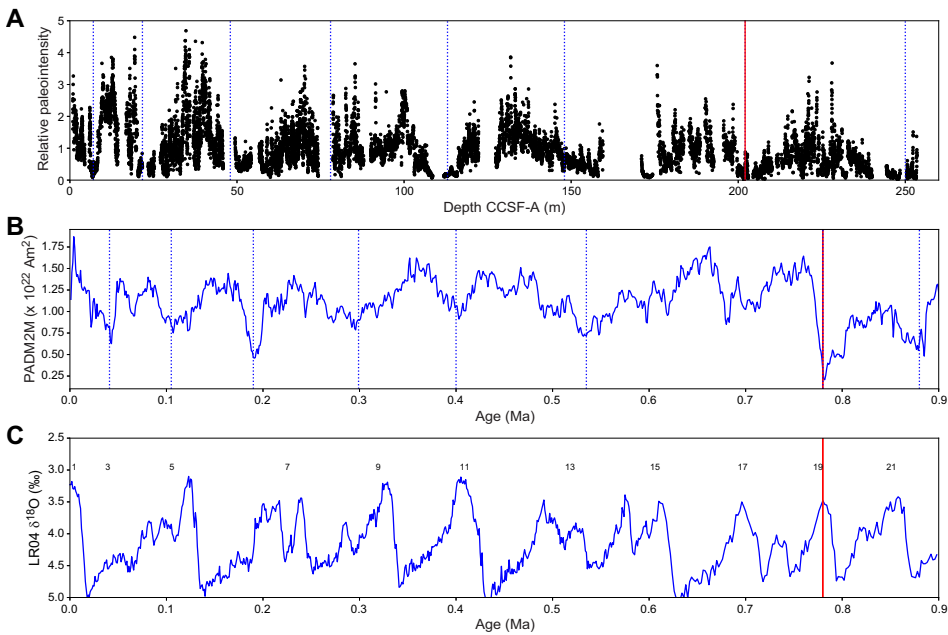
Figure F41. DIPs, Site U1603. A. RPI record from the data shown in Figure F40. B. PADM2M series of Ziegler et al. (2011). C. LR04 δ¹⁸O curve of Lisiecki and Raymo (2005). Marine isotopic stages are identified by numbers above the curve in C. Blue dotted lines = DIPs identified in the RPI record in A (Table T17) and their correlations to the PADM2M time series in B. Solid red lines = Brunhes/Matuyama boundary. Isotopic stages in C can be traced back to core depths through correlation of LR04 to PADM2M and thence to the Site U1603 RPI record using the depths listed in Table T17 on the CCSF-A and CSF-A depth scales. Ages are calibrated to the age model from Tauxe and Yamazaki (2007) and not the GPTS of Ogg (2020).

Table T17. Chron boundary depths and locations of DIPs, Site U1603. **Download table in CSV format.**

Age (Ma)	Depth CSF-A (m)	Depth CCSF-A (m)	Chron boundary
400-U1603A-			
0.041	5.90	7.00	
0.105	20.00	21.70	
0.19	43.00	48.00	
0.299	69.00	78.00	
0.4	103.80	113.00	
400-U1603B-			
0.535	140.20	148.00	
0.78	194.00	201.77	C1r.1r (top)
0.88	239.30	250.00	
400-U1603D-			
0.99	327.00	327.00	C1r.1n (top)
1.07	393.00	393.00	C1r.2n (top)
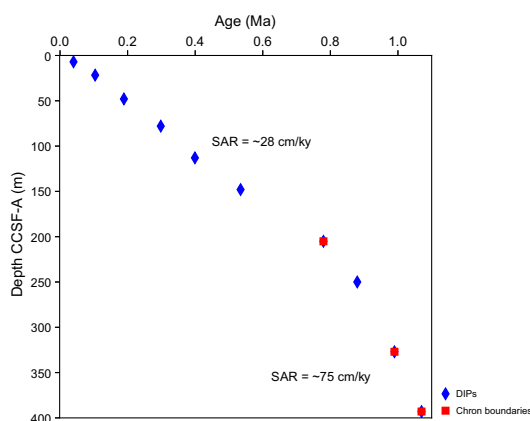
Figure F42. Age-depth plot, Site U1603. Constraints are listed in Table T17. SARs are estimated for the intervals above and below 250 m CCSF-A, about the depth of the top of Lithostratigraphic Unit III. Ages are calibrated to the age model from Tauxe and Yamazaki (2007) and not the GPTS of Ogg (2020).

Subunit IIB (interlaminated to interbedded mud and sand, mud with sand and dispersed clasts) and Unit III (sandy mud to diamicton and thinly laminated mud) (see **Lithostratigraphy**).

10. Downhole logging

Downhole logging was carried out in Hole U1603D upon completion of coring operations. A quad combo tool string recorded MS, natural gamma ray, electrical laterolog resistivity, acoustic velocity, and density data. Four runs (two down passes plus two up passes) were carried out with the sensors recording on the way down and up. Two of the runs (initial down and final up) covered the full length of the hole to 2 m above the bottom. Two calibration runs (one up and one down) were logged in the deepest 100 m of the hole. The caliper showed a relatively homogeneous and stable hole with some washouts at 1900–1950 mbrf, and the instruments yielded reliable measurements.

Upon completion of the downhole logging with the quad combo tool string, vertical seismic profiling was attempted with the VSI. The goal was to obtain an accurate time-depth relationship to tie the logging and coring results to the seismic data. The seismic source was lowered into the water and fired with increasing intensity according to the guidelines for a soft start. The VSI was lowered to the bottom of Hole U1603D. A total of 15 stations were planned for the geophones to record seismic images of the hole; however, a decrease in visibility due to fog resulted in aborting the VSI experiment after 10 stations were attempted. The coupling between the geophone and the hole failed on three stations. On three stations, the seismic wave was well captured with minor

adjustments. For four more stations, manual picking of the wave arrival was possible after processing the signal.

Stability of the hole and sea and ice conditions allowed for a third downhole logging tool. The FMS was run with the DSI to obtain formation resistivity and velocity data. The DSI was used for calibration/comparison with the velocities obtained on the quad combo tool string. The FMS resulted in a compelling resistivity image of Hole U1603D.

Logging measurements were crucial for covering recovery gaps during RCB coring. Core logging and downhole logging results differ on absolute values, but the relative trends of the logs are comparable. Hence, logging data could be used for correlation purposes and for covering the formation recovery gaps with confidence. Additionally, the APCT-3 tool was deployed four times in Hole U1603A and two times in Hole U1603F, performing measurements during APC coring.

10.1. Logging operations

The last core from Hole U1603D arrived on deck at 2230 h (all times provided in local ship time, UTC – 3 h, unless otherwise noted) on 30 August 2023. Hole preparation for the logging program started at 0030 h on 31 August and included a high-viscosity mud sweep followed by releasing the RCB drill bit to the bottom of the hole and displacing the open hole with 10.5 lb/gal heavy mud (barite) to help hole stability. The end of the pipe was raised to 50 meters below seafloor (mbsf) and maintained at this depth throughout the entire logging operation, leaving ~371 m of open hole. The later two logging runs were implemented up to 1903 mbrf. The wireline heave compensator was used to reduce the effect of vertical ship motion on the wireline depth. Rigup for downhole logging started at 0345 h on 31 August under good weather and ice conditions. An issue with a logging winch solenoid delayed the logging operations a few more hours. Fortunately, after a low voltage battery was replaced, logging operations started at 1040 h on 31 August.

The quad combo tool string was assembled for the first run and consisted of the following tools from bottom to top (see **Downhole measurements** in the Expedition 400 methods chapter [Knutz et al., 2025]): Magnetic Susceptibility Sonde (MSS), DSI, High-Resolution Laterolog Array (HRLA), Hostile Environment Litho-Density Sonde (HLDS; with source), Hostile Environment Natural Gamma Ray Sonde (HNGS), and Enhanced Digital Telemetry Cartridge (EDTC). The quad combo tool string was lowered into Hole U1603D at 1040 h on 31 August. All tools were run on the downlog except the density tool, which was run together with the caliper (borehole diameter) measurement tool on the uplog. The downlog started at 1800 mbrf, the seafloor gamma peak was identified at 1811 mbrf, and the log penetrated to 2231 mbrf. No problems were encountered getting down through the pipe or the open hole. Total penetration was 419 m (i.e., 3 m above the total depth of the hole). Thus, the bottom of the hole contained very little to no fall-in or debris. After reaching total depth, the caliper arms were opened and the density tool was enabled. The hole was logged up for a 144 m calibration pass. The tool was lowered back to 2230 mbrf, and the main uplog was collected. Downhole logging with the quad combo tool string was completed, and the tool string was out of the hole by 1515 h on 31 August.

The second logging run consisted of the Vertical Seismic Imager (VSI) with the EDTC (see **Downhole measurements** in the Expedition 400 methods chapter [Knutz et al., 2025]). Observation for protected species began at 1600 h on 31 August. The seismic source consisted of two 250 inch^3 Sercel G guns in parallel array lowered 3 m into the water at 1430 h. The VSI was lowered to 2225 mbrf in Hole U1603D at 1634 h. A total of 15 stations (average spacing = 25 m) were planned to obtain the best correlation with the seismic data (Table **T18**). A decrease in visibility due to fog resulted in the end of the VSI experiment after 10 stations were attempted. Three stations have a good capture of the seismic wave and thus were successful (>1 good shot). Further signal processing and major adjustment was required for four stations. Stations 1 (~2225 m wireline log depth below rig floor [WRF]), 4 (~2150 m WRF), and 7 (~2157 m WRF) failed due to anchoring against the borehole wall. Poor signal, especially on the *z*-axis, is attributed to a soft borehole wall that prevented complete decoupling of the geophone from the shuttle body when the caliper arm was anchored. Foggy conditions reduced the visibility required for observing protected species. Thus, the VSI experiment was aborted at 2120 h. The tool string returned to the surface at 2240 h.

The third logging run deployed the FMS DSI tool string (see **Downhole measurements** in the Expedition 400 methods chapter [Knutz et al., 2025]), which included the HNGS and EDTC. Sonic reprocessing was done using a coherency and dispersion analysis plot for calibration and comparison with the results obtained from the quad combo tool string. The FMS run resulted in a compiled resistivity image of Hole U1603D. The FMS-sonic tool string was lowered into Hole U1603D at 2335 h on 31 August. The tool string reached the base of the hole at 2231 mbrf. Two completed uplogs were recorded to 1902 mbrf. The tool string was returned to the rig floor at 0345 h. All logging equipment was rigged down by 0430 h on 1 September.

10.1.1. Log data quality

The main control on log data quality is the diameter of the borehole measured by the caliper on the HLDS logging tool (Figure **F43**). The borehole diameter was around 11.4 inches with a standard deviation of 1.4 (similar during Runs 1 and 3). The hole was wider than the maximum extent of the caliper arm (17 inches) only in local points at 1911, 1941, 1978, 2070, and 2072 mbrf, leading to robust quality of the logs that require good contact with the borehole wall, such as the density log (Figure **F43**). Log data were transmitted to the Lamont-Doherty Earth Observatory (LDEO) for depth matching and data processing. All readings are within the expected ranges.
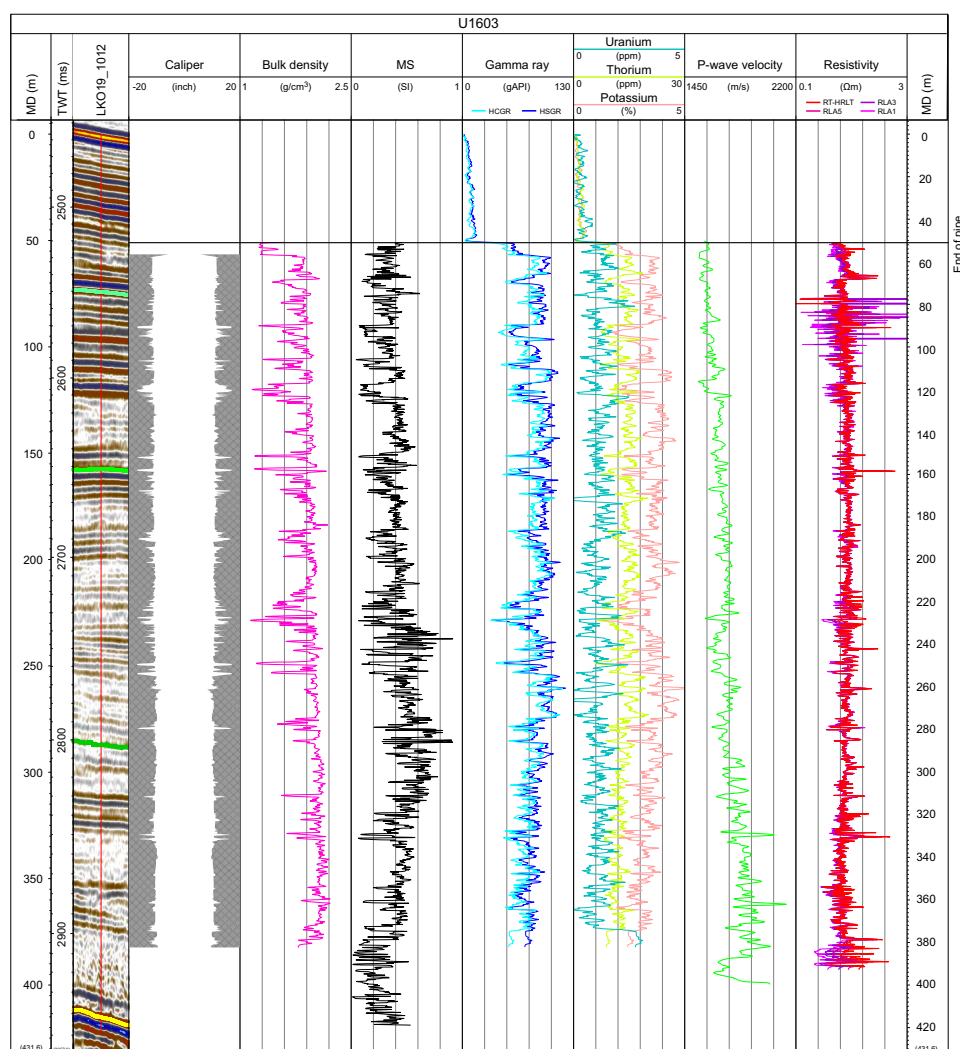
Figure F43. Main downhole logs, Hole U1603D. MD = measured depth. TWT = two-way traveltime. HCGR = computed gamma ray, RT-HRLT = true resistivity (HRLA tool), RLA1 = shallow, RLA3 = medium, RLA5 = deep. Time-depth relation is from the VSI experiment.

The drilling pipe was located at 50 mbsf during all main readings; thus, the uppermost 50 m of the formation are not described in the following text. Density ranges 1.4–2.1 g/cm³ for the majority of the hole, with a baseline slightly increasing downward. Deep resistivity ranges 0.5–2.3 Ωm. Average gamma ray values are greater than 50 American Petroleum Institute gamma ray units (gAPI) and progressively increase downhole to 260 mbsf. Maximum gamma ray values reach 113 gAPI below that depth. MS oscillates between 0.046 and 0.133 SI with mean values of 0.057 SI. *P*-wave velocity ranges 1542–2135 m/s with a general trend of downward increase.

The downlog and uplog data of each measurement do not always perfectly match. In the case of gamma radiation, differences occur in absolute values because the uplog is corrected for borehole diameter as measured by the caliper and the presence of barite-weighted mud whereas the downlog is not corrected because the caliper is closed when the tool is lowered downhole. The uplog and downlog *P*-wave velocity values differ in places because the software is not always able to pick the signal arrival. All DSI runs were run at standard (high) frequency. Processing of the sonic log was implemented on board using the coherency and dispersion analysis plots on Schlumberger's Techlog software at a low frequency. Further sonic processing is needed to determine the *P*- and *S*-wave velocities from the original sonic waveforms.

The downhole natural gamma ray and density logs have features in common with the equivalent shipboard laboratory data from Site U1603 (Figure **F44**), with small offsets between log and core data due to the assignment of core depths when core recovery was not 100% and other effects.

The physical properties (PP) units distinguished using the values from the laboratory core measurements (Figure **F28**) can be extended to the downhole logs with the exception of PP Unit I, which lies within the interval covered by the drilling pipe (Figure **F43**). However, the boundary between PP Units III and IV, characterized by a transition from high-amplitude variability to a relatively constant baseline on density, natural gamma ray, and MS, is observed at 290 mbsf on the downhole logs versus 215 m CSF-A on the core logs. Major differences in depths could be related to the low core recovery deeper than 250 m CSF-A.

Sonic velocity values are consistently higher in downhole measurements compared to the values measured on cores (PWC) because downhole measurements are made under in situ conditions of pressure and temperature.

A detailed comparison of the logging data with the spliced record at Site U1603 is given in **Stratigraphic correlation**. The applied depth relationship is the one obtained from the processed sonic data (see **Core-log-seismic correlation**). The physical properties measured downhole are interpreted in a similar way to those measured on the cores in the laboratory (see **Physical properties**).

Table T18. Check shot stations planned and implemented during the VSI experiment, Site U1603. **Download table in CSV format.**

Station number	Planned measured depth (mbrf)	Measured depth (mbrf)	Status
1	2225	2224.97	No anchoring
2	2200	2223.06	Major adjustment
3	2175	2200.01	Major adjustment
4	2150	2196.60	No anchoring
5	2125	2190.59	Minor adjustment
6	2100	2176.50	Minor adjustment
7	2075	2156.72	No anchoring
8	2050	2155.17	Minor adjustment
9	2025	2111.09	Major adjustment
10	2002	2099.21	Major adjustment
11	1975		Canceled
12	1950		Canceled
13	1925		Canceled
14	1898		Canceled
15	1975		Canceled

10.2. Downhole temperature and heat flow

Six APCT-3 formation temperature measurements were made in Hole U1603A (Cores 4H, 7H, 10H, and 13H) and Hole U1603F (Cores 4H and 10H). Core 400-U1603A-10H moved during the measurements, and equilibration time on Core 13H was shorter than initially planned. However, all six measurements yield reliable results. The obtained temperatures range from 1.6°C at 34.5 m drilling depth below seafloor (DSF) in Hole U1603F to 5.4°C at 118.6 m DSF in Hole U1603A (Table **T19**), giving an approximately linear temperature increase with depth and a geothermal gradient of 41°C/km. The seafloor temperature was determined to be 0.6°C based on APCT-3 data taken while the tool was held at the mudline for 5 min during each run.

Thermal conductivity under in situ conditions was estimated from laboratory-determined thermal conductivity from Hole U1603A using the method of Hyndman et al. (1974) (see **Physical properties** in the Expedition 400 methods chapter [Knutz et al., 2025]). The calculated in situ val-
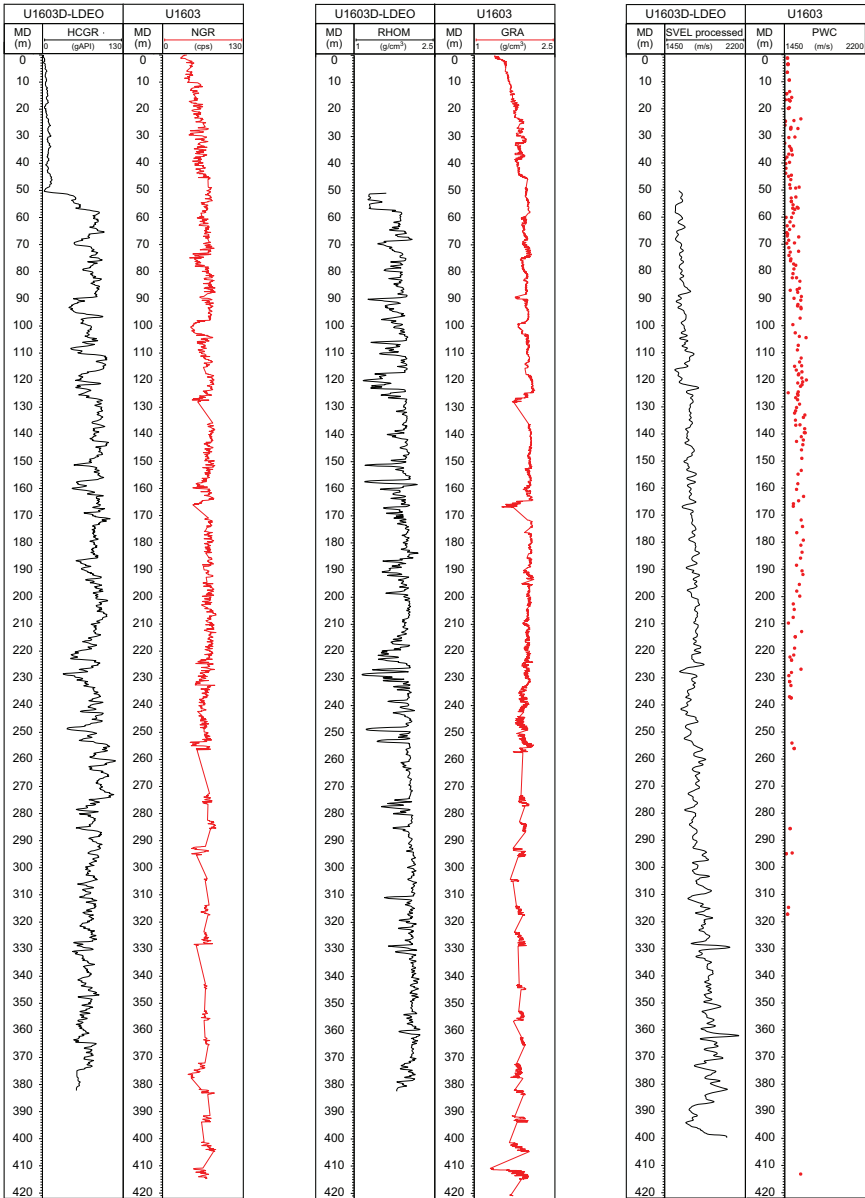
Figure F44. Comparison between downhole (black) and core log (red) gamma radiation, density, and velocity data, Hole U1603D. Velocity includes main sonic and PWC velocity. MD = measured depth, HCGR = computed gamma ray. RHOM = bulk density, SVEL = sonic velocity up.

Table T19. Formation temperatures derived from APCT-3 measurements, Site U1603. **Download table in CSV format.**

Hole, core	APCT-3 depth (m)	Temperature (°C)	Quality	Comments
400-				
Seafloor	0.0	0.57	Tentative value	
U1603A-4H	33.1	2.06	Good	
U1603A-7H	61.6	2.76	Good	
U1603A-10H	90.1	3.79	Not good	Moved
U1603A-13H	118.6	5.39	Good	No temperature equilibration time
U1603F-4H	34.5	1.54	Good	
U1603F-10H	86.8	3.83	Good	

ues are within 2% of the measured shipboard laboratory values. Thermal resistance was then calculated by integrating the inverse of the in situ thermal conductivity over depth. Considering all thermal conductivity measurements for Site U1603, a heat flow of 51 mW/m^2 was estimated from the linear fit between temperature and thermal resistance (Pribnow et al., 2000).

References

Aksu, A.E., 1985. Planktonic foraminiferal and oxygen isotopic stratigraphy of CESAR cores 102 and 103: preliminary results. Geological Survey of Canada Paper, 1985:84–22.

Balsley, J.R., and Buddington, A.F., 1960. Magnetic susceptibility anisotropy and fabric of some Adirondack granites and orthogneisses. American Journal of Science, 258-A:6–20.

Blum, P., 1997. Physical properties handbook: a guide to the shipboard measurement of physical properties of deep-sea cores. Ocean Drilling Program Technical Note, 26. **https://doi.org/10.2973/odp.tn.26.1997**

Brummer, G.-J.A., and Kučera, M., 2022. Taxonomic review of living planktonic foraminifera. Micropaleontology, 41(1):29–74. **https://doi.org/10.5194/jm-41-29-2022**

Cage, A.G., Pieńkowski, A.J., Jennings, A., Knudsen, K.L., and Seidenkrantz, M.S., 2021. Comparative analysis of six common foraminiferal species of the genera Cassidulina, Paracassidulina, and Islandiella from the Arctic–North Atlantic domain. Journal of Micropalaeontology, 40(1):37–60. **https://doi.org/10.5194/jm-40-37-2021**

Christ, A.J., Rittenour, T.M., Bierman, P.R., Keisling, B.A., Knutz, P.C., Thomsen, T.B., Keulen, N., Fosdick, J.C., Hemming, S.R., Tison, J.-L., Blard, P.-H., Steffensen, J.P., Caffee, M.W., Corbett, L.B., Dahl-Jensen, D., Dethier, D.P., Hidy, A.J., Perdrial, N., Peteet, D.M., Steig, E.J., and Thomas, E.K., 2023. Deglaciation of northwestern Greenland during Marine Isotope Stage 11. Science, 381(6655):330–335. **https://doi.org/10.1126/science.ade4248**

Clark, P.U., and Pollard, D., 1998. Origin of the Middle Pleistocene transition by ice sheet erosion of regolith. Paleoceanography, 13(1):1–9. **https://doi.org/10.1029/97PA02660**

Cox, D.R., Huuse, M., Newton, A.M.W., Sarkar, A.D., and Knutz, P.C., 2021. Shallow gas and gas hydrate occurrences on the northwest Greenland shelf margin. Marine Geology, 432:106382. **https://doi.org/10.1016/j.margeo.2020.106382**

de Vernal, A., Rochon, A., and Radi, T., 2013. Dinoflagellates. In Elias, S.A. and Mock, C.J., Encyclopedia of Quaternary Science (Second Edition). Amsterdam (Elsevier), 800–815. **https://doi.org/10.1016/B978-0-444-53643-3.00283-1**

El Bani Altuna, N., Pieńkowski, A.J., Eynaud, F., and Thiessen, R., 2018. The morphotypes of Neogloboquadrina pachyderma: isotopic signature and distribution patterns in the Canadian Arctic Archipelago and adjacent regions. Marine Micropaleontology, 142:13–24. **https://doi.org/10.1016/j.marmicro.2018.05.004**

Eynaud, F., Cronin, T.M., Smith, S.A., Zaragosi, S., Mavel, J., Mary, Y., Mas, V., and Pujol, C., 2009. Morphological variability of the planktonic foraminifer Neogloboquadrina pachyderma from ACEX cores: implications for late Pleistocene circulation in the Arctic Ocean. Micropaleontology, 55(2/3):101–116. **http://www.jstor.org/stable/40607109**

Feyling-Hansen, R.W., 1976. The stratigraphy of the Quaternary Clyde Foreland Formation, Baffin Island, illustrated by the distribution of benthic foraminifera. Boreas, 5(2):77–94. **https://doi.org/10.1111/j.1502-3885.1976.tb00333.x**

Hald, M., and Korsun, S., 1997. Distribution of modern benthic foraminifera from fjords of Svalbard, European Arctic. Journal of Foraminiferal Research, 27(2):101–122. **https://doi.org/10.2113/gsjfr.27.2.101**

Hiscott, R.N., Aksu, A.E., and Nielsen, O.B., 1989. Provenance and dispersal patterns, Pliocene-Pleistocene section at Site 645, Baffin Bay. In Srivastava, S.P., Arthur, M., Clement, B., et al., Proceedings of the Ocean Drilling Program, Scientific Results. 105: College Station, TX (Ocean Drilling Program), 31–52. **https://doi.org/10.2973/odp.proc.sr.105.117.1989**

Hyndman, R.D., Erickson, A.J., and Von Herzen, R.P., 1974. Geothermal measurements on DSDP Leg 26. In Davies, T.A., Luyendyk, B.P., et al., Initial Reports of the Deep Sea Drilling Project. 26: Washington, DC (US Government Printing Office), 451–463. **https://doi.org/10.2973/dsdp.proc.26.113.1974**

Jakobsson, M., Mayer, L., Coakley, B., Dowdeswell, J.A., Forbes, S., Fridman, B., Hodnesdal, H., Noormets, R., Pedersen, R., Rebesco, M., Schenke, H.W., Zarayskaya, Y., Accettella, D., Armstrong, A., Anderson, R.M., Bienhoff, P., Camerlenghi, A., Church, I., Edwards, M., Gardner, J.V., Hall, J.K., Hell, B., Hestvik, O., Kristofferson, Y., Marcussen, C., Mohammad, R., Mosher, D., Nghiem, S.V., Pedrosa, M.T., Travaglini, P.G., and Weatherall, P., 2012. The International Bathymetric Chart of the Arctic Ocean (IBCAO) Version 3.0. Geophysical Research Letters, 39(12):L12609. **https://doi.org/10.1029/2012GL052219**

Jennings, A., Reilly, B., Andrews, J., Hogan, K., Walczak, M., Jakobsson, M., Stoner, J., Mix, A., Nicholls, K.W., O'Regan, M., Prins, M.A., and Troelstra, S.R., 2022. Modern and Early Holocene ice shelf sediment facies from Petermann Fjord and northern Nares Strait, northwest Greenland. Quaternary Science Reviews, 283:107460. **https://doi.org/10.1016/j.quascirev.2022.107460**

Jennings, A.E., and Helgadottir, G., 1994. Foraminiferal assemblages from the fjords and shelf of eastern Greenland. Journal of Foraminiferal Research, 24(2):123–144. **https://doi.org/10.2113/gsjfr.24.2.123**

Jennings, A.E., Seidenkrantz, M.-S., and Knudsen, K.L., 2020. Glomulina oculus, new calcareous foraminiferal species from the high Arctic: a potential indicator of a nearby marine-terminating glacier. Journal of Foraminiferal Research, 50(2):219–234. **https://doi.org/10.2113/gsjfr.52.2.219**

Kaminski, M.A., Gradstein, F.M., Scott, D.B., and MacKinnon, K.D., 1989. Neogene benthic foraminifer biostratigraphy and deep-water history of Sites 645, 646, and 647, Baffin Bay and Labrador Sea. In Srivastava, S.P., Arthur, M., Clement, B., et al., Proceedings of the Ocean Drilling Program, Scientific Results. 105: College Station, TX (Ocean Drilling Program), 731–756. **https://doi.org/10.2973/odp.proc.sr.105.123.1989**

Kelleher, R., Jennings, A., Andrews, J., Brooks, N.K.S., Marchitto, T., Feng, S., Woelders, L., Normandeau, A., Jenner, K., Bennett, R., and Brookins, S., 2022. Late glacial retreat of the Lancaster Sound Ice Stream and early Holocene onset of Arctic/Atlantic throughflow in the Arctic Island channels. Arctic, Antarctic, and Alpine Research, 54(1):395–427. **https://doi.org/10.1080/15230430.2022.2110689**

Knutz, P.C., Jennings, A.E., Childress, L.B., Bryant, R., Cargill, S.K., Coxall, H.K., Frank, T.D., Grant, G.R., Gray, R.E., Ives, L., Kumar, V., Le Houedec, S., Martens, J., Naim, F., Nelissen, M., Özen, V., Passchier, S., Pérez, L.F., Ren, J., Romans, B.W., Seki, O., Staudigel, P., Tauxe, L., Tibbett, E.J., Yokoyama, Y., Zhang, Y., and Zimmermann, H., 2025. Expedition 400 methods. In Knutz, P.C., Jennings, A.E., Childress, L.B., and the Expedition 400 Scientists, NW Greenland Glaciated Margin. Proceedings of the International Ocean Discovery Program, 400: College Station, TX (International Ocean Discovery Program). **https://doi.org/10.14379/iodp.proc.400.102.2025**

Knutz, P.C., Newton, A.M.W., Hopper, J.R., Huuse, M., Gregersen, U., Sheldon, E., and Dybkjær, K., 2019. Eleven phases of Greenland Ice Sheet shelf-edge advance over the past 2.7 million years. Nature Geoscience, 12(5):361–368. **https://doi.org/10.1038/s41561-019-0340-8**

Knutz, P.C., Perez, L., Hopper, J.R., Andreasen, K.J., Newton, A., Cox, D., Huuse, M., Dorschel, B., Campbell, C., and BIOS Team, submitted. Pleistocene sediment drifts on the north-west Greenland margin formed by contour current and downslope interactions. Marine Geology.

Lisiecki, L.E., and Raymo, M.E., 2005. A Pliocene-Pleistocene stack of 57 globally distributed benthic $\delta^{18}O$ records. Paleoceanography, 20(1):PA1003. **https://doi.org/10.1029/2004PA001071**

Lofverstrom, M., Thompson, D.M., Otto-Bliesner, B.L., and Brady, E.C., 2022. The importance of Canadian Arctic Archipelago gateways for glacial expansion in Scandinavia. Nature Geoscience, 15(6):482–488. **https://doi.org/10.1038/s41561-022-00956-9**

Mudie, P.J., 1992. Circum-Arctic Quaternary and Neogene marine palynofloras: paleoecology and statistical analysis. In Head, M.J., and Wrenn, J.H. (Eds.), Neogene and Quaternary dinoflagellate cysts and acritarchs. 10: Houston, TX (American Association of Stratigraphic Palynologists Foundation), 347–390.

Münchow, A., Falkner, K.K., and Melling, H., 2015. Baffin Island and West Greenland current systems in northern Baffin Bay. Progress in Oceanography, 132:305–317. **https://doi.org/10.1016/j.pocean.2014.04.001**

Newton, A.M.W., Huuse, M., Cox, D.R., and Knutz, P.C., 2021. Seismic geomorphology and evolution of the Melville Bugt trough mouth fan, northwest Greenland. Quaternary Science Reviews, 255:106798. **https://doi.org/10.1016/j.quascirev.2021.106798**

Newton, A.M.W., Knutz, P.C., Huuse, M., Gannon, P., Brocklehurst, S.H., Clausen, O.R., and Gong, Y., 2017. Ice stream reorganization and glacial retreat on the northwest Greenland shelf. Geophysical Research Letters, 44(15):7826–7835. **https://doi.org/10.1002/2017GL073690**

Ogg, J.G., 2020. Geomagnetic Polarity Time Scale. In Gradstein, F.M., Ogg, J.G., Schmitz, M., and Ogg, G. (Eds.), Geologic Time Scale 2020. Amsterdam (Elsevier), 159–192. **https://doi.org/10.1016/B978-0-12-824360-2.00005-X**

Okolodkov, Y.B., 1998. A checklist of dinoflagellates recorded from the Russian Arctic seas. Sarsia, 83(4):267–292. **https://doi.org/10.1080/00364827.1998.10413687**

Pribnow, D.F.C., Kinoshita, M., and Stein, C.A., 2000. Thermal data collection and heat flow recalculations for ODP Legs 101–180: Hannover, Germany (Institute for Joint Geoscientific Research, GGA). **http://www-odp.tamu.edu/publications/heatflow/**

Radi, T., Bonnet, S., Cormier, M.-A., de Vernal, A., Durantou, L., Faubert, É., Head, M.J., Henry, M., Pospelova, V., Rochon, A., and Van Nieuwenhove, N., 2013. Operational taxonomy and (paleo-)autecology of round, brown, spiny dinoflagellate cysts from the Quaternary of high northern latitudes. Marine Micropaleontology, 98:41–57. **https://doi.org/10.1016/j.marmicro.2012.11.001**

Schaefer, J.M., Finkel, R.C., Balco, G., Alley, R.B., Caffee, M.W., Briner, J.P., Young, N.E., Gow, A.J., and Schwartz, R., 2016. Greenland was nearly ice-free for extended periods during the Pleistocene. Nature, 540(7632):252–255. **https://doi.org/10.1038/nature20146**

Schwehr, K., and Tauxe, L., 2003. Characterization of soft-sediment deformation: detection of cryptoslumps using magnetic methods. Geology, 31(3):203–206. **https://doi.org/10.1130/0091-7613(2003)031<0203:COSSDD>2.0.CO;2**

Seidenkrantz, M.-S., 2013. Benthic foraminifera as palaeo sea-ice indicators in the subarctic realm – examples from the Labrador Sea–Baffin Bay region. Quaternary Science Reviews, 79:135–144. **https://doi.org/10.1016/j.quascirev.2013.03.014**

Simon, Q., Hillaire-Marcel, C., St-Onge, G., and Andrews, J.T., 2014. North-eastern Laurentide, western Greenland and southern Innuitian ice stream dynamics during the last glacial cycle. Journal of Quaternary Science, 29(1):14–26. **https://doi.org/10.1002/jqs.2648**

Smelror, M., 1999. Pliocene-Pleistocene and redeposited dinoflagellate cysts from the western Svalbard margin (Site 986); biostratigraphy, paleoenvironments, and sediment provenance. In Raymo, M.E., Jansen, E., Blum, P., and Herbert, T.D. (Eds.), Proceedings of the Ocean Drilling Program, Scientific Results. 162: College Station, TX (Ocean Drilling Program). **https://doi.org/10.2973/odp.proc.sr.162.011.1999**

Stehman, C.F., 1972. Planktonic foraminifera in Baffin Bay, Davis Strait and the Labrador Sea. Atlantic Geoscience, 8(1):13–19. **https://doi.org/10.4138/1398**

Tang, C.C.L., Ross, C.K., Yao, T., Petrie, B., DeTracey, B.M., and Dunlap, E., 2004. The circulation, water masses and sea-ice of Baffin Bay. Progress in Oceanography, 63(4):183–228. **https://doi.org/10.1016/j.pocean.2004.09.005**

Tauxe, L., 2010. Essentials of Paleomagnetism: Oakland, CA (University of California Press).

Tau xe, L., and Yamazaki, T., 2007. 5.13 - Paleointensities. In Schubert, G., Treatise on Geophysics. Amsterdam (Elsevier), 509–563. **https://doi.org/10.1016/B978-044452748-6.00098-5**

Weber, M.E., 1998. Estimation of biogenic carbonate and opal by continuous non-destructive measurements in deep-sea sediments: application to the eastern equatorial Pacific. Deep Sea Research, Part I: Oceanographic Research Papers, 45(11):1955–1975. **https://doi.org/10.1016/S0967-0637(98)00028-4**

Weber, M.E., Niessen, F., Kuhn, G., and Wiedicke, M., 1997. Calibration and application of marine sedimentary physical properties using a multi-sensor core logger. Marine Geology, 136(3–4):151–172. **https://doi.org/10.1016/S0025-3227(96)00071-0**

Ziegler, L.B., Constable, C.G., Johnson, C.L., and Tauxe, L., 2011. PADM2M: a penalized maximum likelihood model of the 0–2 Ma palaeomagnetic axial dipole moment. Geophysical Journal International, 184(3):1069–1089. **https://doi.org/10.1111/j.1365-246X.2010.04905.x**

Zijderveld, J.D.A., 1967. AC demagnetization of rocks: analysis of results. In Runcorn, S.K.C., Creer, K.M., and Collinson, D.W. (Eds.), Methods in Palaeomagnetism. Developments in Solid Earth Geophysics. J.R. Balsley (Series Ed.), 3: 254–286. **https://doi.org/10.1016/B978-1-4832-2894-5.50049-5**